Electronic Structure of Vanadium Phosphorus Oxides

vorgelegt von
Diplom - Ingenieur
Marc - Georg Willinger
Berlin

Fakultät II – Mathematik und Naturwissenschaften
der Technischen Universität Berlin
zur Erlangung des akademischen Grades

Doktor der Naturwissenschaften
Dr.rer.nat.

genehmigte Dissertation

Promotionsausschuss:

Vorsitzender:	Prof. Dr. rer. nat. R. Schomäcker
Berichter:	Prof. Dr. rer. nat. R. Schlögl
Berichter:	Prof. Dr. rer. nat. M. Lerch

Tag der wissenschaftlichen Aussprache: 28. Juni 2005

Berlin 2005

D 83

Kurzzusammenfassung

Marc-Georg Willinger - Elektronische Struktur von Vanadium Phosphor Oxiden.

Vanadium Phosphor Oxide (VPO) zeichnen sich durch ihre strukturelle Komplexität und die Existenz einer Vielzahl von unterschiedlichen Polymorphen aus, welche leicht ineinander überführt werden können. Mit dieser Eigenschaft verbunden ist ihre Anwendung in der Katalyse, wo sie als Katalysatoren in der Synthese von Maleinsäure Anhydrid aus n-Butan Verwendung finden. Aufgrund der Komplexität der Reaktion werden dem aktiven Katalysator im Wechselspiel mit den aus der Gasphase adsorbierten Molekülen Eigenschaften abverlangt, welche sich nicht durch die alleinige Existenz einer kristallinen Phase erklären lassen. Obwohl der industriell eingesetzte Katalysator zum überwiegenden Teil aus Vanadium Pyrophosphat (VO)2P2O7 besteht, steht sowohl der Umsatz als auch die Selektivität des Katalysators mit der Präsenz verschiedener fünfwertiger VPO Phasen in Beziehung. Die Zusammensetzung der Oberfläche des aktiven Katalysators und das Zusammenspiel der verschiedenen auftretenden Phasen definieren die Zentrale Frage zur Aufklärung der katalytischen Aktivität. Eine Möglichkeit, die dem System innewohnende Komplexität zu verringern, besteht darin, einzelne katalytisch relevante Phasen für sich isoliert zu untersuchen. Die vorliegende Arbeit fasst eine kombinierte experimentelle und theoretische Untersuchung von Vanadium Phosphor Oxid Phasen zusammen. Bandstruktur Rechnungen basierend auf der Dichtefunktional Theorie (DFT) liefern einen detaillierten Einblick in die elektronische Struktur und erlauben es, anhand der untersuchten Phasen die Beziehung zwischen der geometrischen und der elektronischen Struktur zu untersuchen. Elektronen Energieverlust Spektren (EELS) liefern Information über die lokale elektronische Struktur. In Kombination mit den Simulationen lassen sich Peaks in den Spektren auf die zugrunde liegenden Anregungsprozesse zurückverfolgen. Die untersuchten Systeme stellen dabei Referenzsysteme dar, anhand deren Spektren von Proben unbekannter Phasenzusammensetzung interpretiert werden können. Dies ist eine wesentliche Voraussetzung für die Interpretation von zukünftigen in-situ Röntgen Absorptionsspektren.

Abstract

Marc-Georg Willinger - Electronic structure of vanadium phosphorus oxides.

Vanadium phosphorus oxides (VPO) are a very complex and fascinating system characterized by an easy formation and inter conversion of several crystalline phases. VPO´s are commercially used as catalysts for the synthesis of maleic anhydride (MA) in the partial oxidation of n-butane. This complex reaction involves several steps which acquire a concerted mechanism coupling acid and oxidizing properties. VPO catalysts consist of the main V^{4+} phase $(VO)_2P_2O_7$ and a mixture of pentavalent $VOPO_4$ phases. These phases are crucial for the conversion and selectivity rate of the final catalyst. It is believed that only a specific combination of V^{4+} and V^{5+} phases leads to the high catalytic performance. One way to get a more profound understanding of the real catalyst and the role of the different phases is to reduce the complexity of the system by investigating the specific occurring phases in depth on their own. This thesis reports the investigation of the electronic structure of VPO phases by means of a combined theoretical and experimental approach. The investigated phases represent reference systems that contain electronic and structural features that are characteristic for the phases that are involved in catalysis. Ab-initio band structure calculations based on density functional theory (DFT) were performed in order to evaluate the bulk electronic structure. Core level spectroscopic methods were applied to experimentally probe the electronic structure at the ionized species. The band structure calculations provide a detailed insight into bonding properties such as hybridization and covalent versus ionic bonding and the localization of the electrons. Characteristic features of differently coordinated oxygens in the recorded electron energy loss (EELS) spectra can be identified by comparing them to the simulated spectra and to the underlying site and angular momentum projected density of states. Spectral features are hence well understood and can be used for the interpretation of spectra recorded from samples of unknown phase composition.

Contents

List of Figures

List of Tables

Chapter 1

Introduction

A catalyst was defined by J. J. Berzelius in 1836 as a compound, which increases the rate of a chemical reaction, but which is not consumed by the reaction. A huge variety of catalytic processes are found in nature. From enzymes, which catalyze all aspects of cell metabolism, to mineral surfaces, catalysts increase the rate of a given reaction, often by reducing the activation energy that the reactants must overcome before they go on to form products. Catalysis is of crucial importance for the chemical industry and catalysts have been developed for a wide spectrum of reactions, with perhaps the most popular example being the converter in cars used to reduce toxic emissions. Catalysts can be described as either homogeneous or heterogeneous. Homogeneous catalysts are molecularly dispersed with the reactants in the same phase. This provides easy access to the catalytic site but can make the separation of catalyst and products difficult. Heterogeneous catalysts - usually solids - are in a different phase from the reactants, which reduces separation problems but provides more limited access to the catalytic site. The principal interest in catalysis research is to control the rate of chemical reactions. This requires a detailed understanding of the mechanism of all reaction steps involved. For decades, studies of heterogeneous catalysts were largely empirical, involving little understanding at the molecular level. Theories of how they function, emphasized the need for complementarity between reactant structure and the geometrical arrangement of the catalysts surface atoms.

This thesis is focused on the investigation of the geometric and electronic structure of several vanadium phosphorus oxides (VPO´s). A combination of theoretical and experimental tools has been applied to study different compounds and some of their most prominent phases. The systems studied are of significant relevance toward a more solid

understanding of the catalytic activity of VPO catalysts. To one point because some of the investigated phases are thought to be directly involved in the catalytic process [1–5] and, second, because the investigated phases serve as reference or "standard" phases for the investigation of more complex systems in a further step. Band structure calculations based on density functional theory elucidate detailed information about the electronic structure and effects of geometry variations on the bonding properties. Samples were characterized by means of electron microscopy, electron diffraction, X-ray diffraction and core-shell excitation spectroscopy (electron energy loss spectroscopy and X-ray absorption spectroscopy). Local analysis of the electronic structure by means of electron spectroscopy performed in the electron microscope takes into account the inherent heterogeneity at the surface of the catalytically active material.

Overview of the thesis

In Chapter 2 the role of vanadium phosphorous oxides in heterogeneous catalysis is pointed out.
Chapter 3 describes the experimental and theoretical techniques on which the thesis is based.
In Chapter 4 two polymorph of V_2O_5 are compared to each other in view of differences in their geometric and electronic structure. These two polymorph serve as simple reference systems in the discussion of more complicated vanadium phosphorous oxides investigated in the later Chapters. In Chapter 5, the electronic and geometric structures of several polymorph of vanadium(V) phosphorous oxide phases are investigated. The effect of oxidation state on the electronic structure is elucidated by the investigation of vanadium(IV) and vanadium(III) phosphorous oxide phases in Chapter 6 and 7, respectively. Finally, Chapter 9 concludes and summarizes the results.

Chapter 2

Vanadium in catalysis

Vanadium was discovered in 1801 in Mexico by the Spanish mineralogist A.M. del Rio, who considered it to be present in a particular brownish lead mineral [6]. He named the new element Erythronium. However, the French chemist H.V. Collet-Descotils incorrectly declared that this new element was only impure chromium. Later on, in 1830, the Swedish chemist N.G. Sefström rediscovered the element and named it in honor of Vanadis, the old Norse name for the Nordic goddess Freyja- a fertility goddess - because of its beautiful multicolored compounds. Vanadium is one of the most abundant and widely distributed non-iron metals in the earth's crust and is found in about 152 different minerals, in certain iron ores and also in the form of organic complexes in some crude oils. The major sources of vanadium are titaniferrous magnetite ores from mines in Australia, China, Russia and South Africa. The current level of the annual production of vanadium in the world is 38,000 tonnes [7]. About 80% of the vanadium produced is used as steel additive, as it makes steel shock- and vibration-resistant. Vanadium is also an essential element in aerospace industry, as it guarantees low density, high strength and resistance to high operating temperatures and stress. Titanium-aluminum-vanadium alloys are used in, e.g. aero-engine gas turbines and in the undercarriages of planes. Other uses of vanadium are in ceramics and electronics. Vanadium salts are well known for the brilliant orange and blue colors in ceramics or in dyes for textiles and leather. The most dominant non-metallurgical use of vanadium is in catalysis, which represents about 5% of the annual production of vanadium.

2.1 Vanadium Oxides

Vanadium oxides play an important role in a number of catalytic processes such as hydrocarbon oxidation, where the oxide catalyst participates in the reaction by abstracting hydrogens and/or transferring surface oxygen to the organic molecule [7]. Vanadium atoms exist in different formal oxidation states which vary from two to five. The ability of vanadium atoms to possess multiple stable oxidation states results in the easy conversion between oxides of different stoichiometry by oxidation or reduction and is believed to be an important factor for the oxide to function as catalyst in selective oxidation. Some of the vanadium oxides undergo reversible metal-insulator transitions as a function of temperature, pressure or doping. Along with these transitions come magnetic transitions and structural changes. Prominent examples are V_2O_4 and V_2O_3, where the change in resistivity extends over several orders of magnitude [8]. In both compounds, the first-order phase transition is accompanied by structural changes affecting the geometry of the characteristic VO_6 octahedra [9]. In addition, V_2O_3 exhibits long-range antiferromagnetic order below the transition temperature [10]. The origin of the metal-insulator transition is still a matter of controversy. As a consequence, a complete and accepted picture of the physics of the vanadium oxides has not yet evolved.

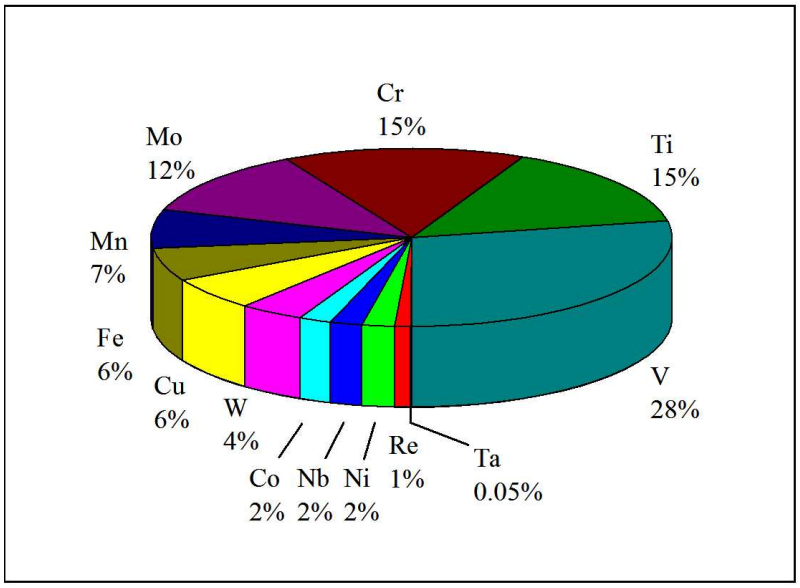

Fig. 2.1: Overview of the importance of vanadium in supported metal oxide catalysts. Numbers taken from Weckhuysen *et al.* [7].

2.2 Vanadium Phosphorus Oxide Catalysts

Vanadium phosphorus oxides (VPO) are a very complex and fascinating system characterized by an easy formation and inter conversion of a variety of crystalline phases. They are commercially used as catalysts for the synthesis of maleic anhydride (MA) in the partial oxidation of n-butane.

2.2.1 Crystal structures of VPO phases

The known main phases and precursors of the VPO system involved in catalysis are set up of distorted VO_6 octahedra sharing vertices with independent PO_4 tetrahedra. The oxygen polyhedron of vanadium is so irregular that it is often considered as a VO_5 square pyramid with a very short apical vanadyl bond ($d_{V=O}$ = 1.59Å in the α_{II} form) and a much more remote sixth oxygen atom ($d_{V\cdots O}$ = 2.85Å). The structural framework of anhydrous VPO phases involved in catalysis can be classified roughly in three groups:
(i) single octahedra that are linked together so as to produce chains of alternated short and long vanadium-oxygen bonds (V=O$\cdots$V=O$\cdots$) in one (α_I-, α_{II}- and β-$VOPO_4$) or in two perpendicular directions as in the proposed structure of ω-$VOPO_4$ [11] and
(ii) pairs of edge-sharing octahedra that are linked together via common apexes, leading again to chains of alternated short and long V-O bonds as in $(VO)_2P_2O_7$ and
(iii) rows of edge-sharing octahedra as in and VPO_4, respectively (an overview with examples is given in Fig. 2.2).
The four equatorial oxygens are generally shared with single PO_4 tetrahedra or P_2O_7 double tetrahedra as in ortho PO_4 and pyro P_2O_7 phosphates, respectively, or even with chains of metaphosphate PO_3, according to the valence of vanadium and the atomic ratio P/V.

2.2.2 The reaction from n-butane to maleic anhydride

MA is an important intermediate for chemical industry, particularly for the production of unsaturated polyester resins, agricultural chemicals, lubricating oil additives and pharmaceuticals [12]. The main product is unsaturated polyester resin, which is mainly used in construction, boat-building, automotive and electrical industries in form of so-called fiber-glass reinforced plastics. MA was first synthesized in the 1830´s [13, 14] and the commercial manufacturing began one hundred years later in 1933 by National Aniline

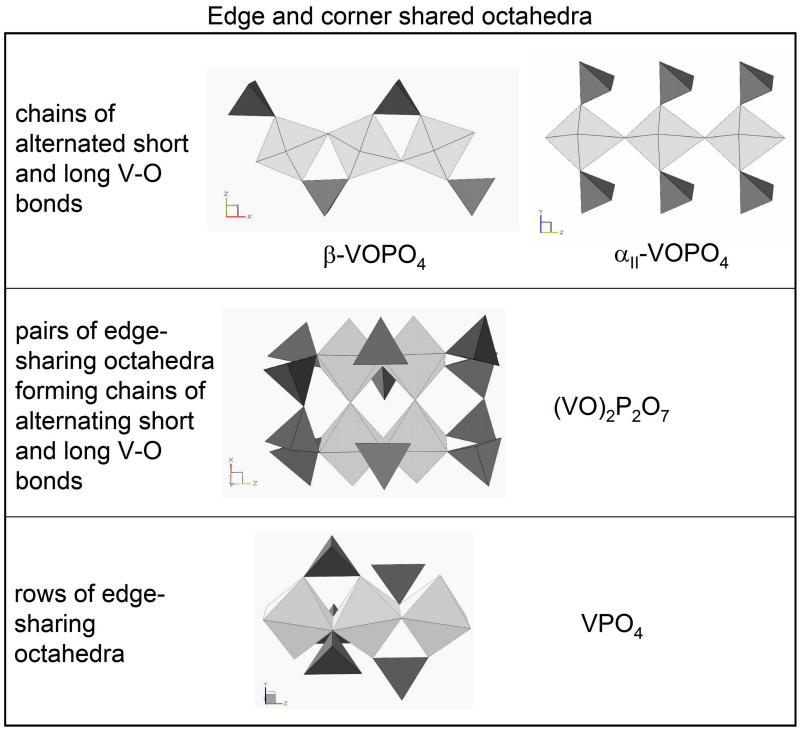

Fig. 2.2: Structural framework of anhydrous VPO phases involved in catalysis and representative examples. Dark tetrahedra correspond to PO_4 units, light gray octahedra correspond to VO_6 units

and Chemical Co., Inc., using a process based on benzene oxidation catalyzed by a vanadium oxide catalyst [15]. The production from n-butane has nowadays largely replaced productivity from benzene due to a lower cost of the raw materials and for environmental reasons. Maleic anhydride (1) and its derivatives maleic acid (2) and fumaric acid (3) are produced with an annual world-wide capacity of over $1 \cdot 10^6$ tons [16].

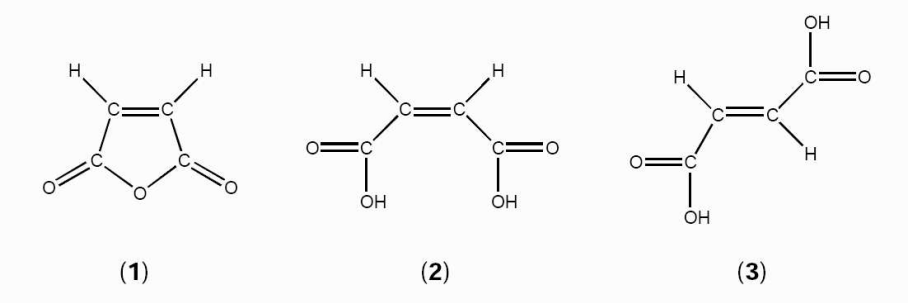

Fig. 2.3: Maleic anhydride (1) and its derivatives maleic acid (2) and fumaric acid (3).

The conversion of n-butane to maleic anhydride by VPO catalysts is recognized as one of the most complex selective oxidation reactions used in industry today. This complex reaction involves the abstraction and transport of 8 hydrogens that form four water molecules, and insertion of three oxygens (two carbonyl type, one furan type) resulting in cyclization of the initial butane. In total, 14 electrons are exchanged in the process.

$$2C_4H_{10} + 7O_2 \longrightarrow 2C_4H_2O_3 + 8H_2O \tag{2.1}$$

Research on this catalytic system has been largely developed in the last decade and many publications and reviews have been devoted on the search for the catalytically active species on the catalyst surface and the reaction mechanism [2, 5, 12, 17–22].

Different industrial technologies are presently existing which involve fixed-bed, fluid-bed as well as circulating fluid-bed riser reactors [2] and are all based on the unique vanadyl pyrophosphate $(VO)_2P_2O_7$ catalyst.

2.3 Basic concepts of heterogeneous catalysis

The basic steps of a chemical reaction in heterogeneous catalysis are (1) the adsorption of the reacting species on the surface, (2) their reaction, and (3) the desorption of the product

(the Langmuir-Hinschelwood process). Adsorption on the catalyst causes a change in the state of the reactants, possibly including disassociation, which allows the reaction to take place. Before the reaction actually occurs, there may also be substantial diffusion and possibly reassociation and desorption of unreacted species. The final desorption step is necessary for the product to be recovered and for the catalyst to be regenerated.

Kinetic modeling of partial oxidation reactions spans over 30 years. Two basic concepts comprise the cornerstones in the conception and development of selective oxidation catalysis of light hydrocarbons: the first is the postulate, that lattice oxygen of certain multivalent transition metal oxides serves as a more versatile and selective oxidizing agent (redox) than gaseous oxygen and the second is the idea of site isolation [23], the spatial separation of active sites from each other on the catalyst surface of a heterogeneous catalyst.

Lattice oxygen

Lattice oxygen is thought to be a special form of atomic oxygen which is bound strongly enough to the catalyst to be moderated in its oxidizing power but weakly enough to oxidize a pre-activated substrate molecule. Mars and van Krevelen [24] described a mechanism in which the organic reactant is oxidized by lattice oxide ions at the surface, which are subsequently replenished by dioxygen dissociation in combination with surface and solid state diffusion, resulting in re-oxidation of the surface site. Regeneration of the reduced metal oxide must be faster than its reduction for the system to function as a catalyst. Thus, the catalyst must be characterized by facile change of the oxidation state of its cations. Since transition metal oxides belong to systems that may change the electronic states of the metal in a wide range, they are the main compounds for active and selective catalysts.

Site isolation

Site isolation was surmised to be a prerequisite for obtaining desired, selective partial oxidation products from the corresponding hydrocarbons in heterogeneous oxidation catalysis. It states that reactive surface lattice oxygens must be structurally isolated from each other in defined groupings on a catalyst surface in order to achieve selectivity. The number of oxygens in a given isolated grouping determines the reaction channel through the stoichiometry requirements imposed on the reaction by the availability (or lack) of oxy-

gens at the reaction site.

Phase cooperation

Phase cooperation is another important concept [23]. It was born from investigations that revealed that the combination of two phases, when in intimate contact, performed more effectively than the sum of the two phases when operating separately or far removed from each other. Two phases cooperate with each other in a way that phase I performs the actual catalytic function while phase II takes a subordinate, re-oxidation function. Alternatively, it is also conceivable that an intergrowth or overgrowth of two phases comprise the actual improved catalyst. For phase cooperation to be effective, it is imperative that the two or more phases are in intimate contact with each other, in order to facilitate their cooperation on an atomic scale. This condition is readily met when the two phases contain at least one lattice plane each that are structurally closely matched, thereby facilitating the formation of coherent interfaces (epitaxy) between the two phases [23]. Since phase cooperation is the result of the formation of nanodomains of one phase coherently bound to the other, it may result also in site isolation. Examples for situations which provide the possibility for site isolation are defect structures, effect of promoters and of supports, inclusion in zeolites, etc...

2.4 Unsolved questions about the active site

The complex partial oxidation of alkanes involves several steps: chemisorption at the surface, abstraction of hydrogen, insertion of oxygen and desorption of the product from the surface. This requires a concerted mechanism which couples acid and oxidizing properties. In order to catalyze the oxidative transformation with good selectivity, the surface the catalyst must therefore have multi functional properties. Experimental evidence lead to the general consensus that the reaction follows a Mars van Krevelen mechanism [25–27]. Bulk VPO catalyst is usually produced by activation of the catalyst precursor in reaction condition for several hundreds hours. There is a general agreement in the fact that vanadium pyrophosphate (VPP) is the essential phase of the catalyst for the mild oxidation of *n*-butane to MA [2, 17, 28, 29]. It is the only phase with long range order which has been identified by XRD for the long-term ”equilibrated” VPO catalyst. Furthermore, the average oxidation state of vanadium measured on the best working catalysts after the catalytic test measures around 4.1 and is consistent with the main par-

ticipation of VPP (oxidation state: 4.0). A model for the oxidation of butane was even proposed on the (100) face of this phase [2, 30, 31]. However, in agreement with the 4.1 oxidation state, the participation, to some extent, of $VOPO_4$ (V^{5+}) - phases in some steps of the reaction pathway has to be considered [2, 17, 28, 29]. The difficulty in identifying the active sites stems from the fact that VPO catalysts are composed of both well crystallized and amorphous phases whose participation to the mechanism of butane oxidation is not jet completely understood. The surface terminations and thus the surface composition depends on (i) the method of preparation (organic preparation which starts with a precursor of poorer crystallinity leads to a surface richer in phosphorus) and (ii) time on stream (as time on stream increases, the amount of phosphorus on the surface decreases due to partial recrystallization of the surface).

The role of VPO (V^{5+}) and (V^{3+}) phases

Contradictory results appear in the literature about the role of $VOPO_4$ phases on VPP: it has been considered that micro domains of δ- and γ-$VOPO_4$ on $(VO)_2P_2O_7$ are detrimental to catalytic performances [30] and that V^{5+} ions are "parasitic species" responsible for the consecutive overoxidation of MA to CO_2 [32]. On the other hand it is believed that only a specific combination of V^{4+} and V^{5+} phases leads to the high catalytic performance [4]. The presence of the crystalline V^{5+} phases in combination with the vanadyl pyrophosphate is thought to enhance the rate of oxidation of the adsorbed intermediates. In this case the catalyst works as a biphasic system containing microdomains of the oxidized $VOPO_4$ phase and the reduced VPP phase, according to the Mars and van Krevelen mechanism. Volta et al. [3] have explored the correlation between presence of $VOPO_4$ and catalytic behavior using a combination of various physico-chemical techniques and found that an increase in the selectivity to maleic anhydride, but a decrease in butane conversion can be related to the presence of α-$VOPO_4$ together with VPP. Using *in-situ* Raman spectroscopy and ^{31}P NMR techniques, it has also been claimed that disorganized γ- , δ- and α_{II}-$VOPO_4$ structures on the VPP matrix are responsible for the formation of maleic anhydride [33, 34]. Additionally, Zhang-Lin et al. [35, 36] have shown that γ - and δ-$VOPO_4$ have even selectivities for maleic anhydride production similar to VPP. Using time-resolved in situ x-ray absorption spectroscopy, Coulston *et al.* [27] showed that maleic anhydride production involves the reaction of V^{5+}. Concluding their results they suggest that V^{5+} species may play a role in the initial hydrogen abstraction from n-butane, which is the rate-determining step in n-butane selective oxidation. Bordes and

Courtine suggest that the active sites in n-butane oxidation to maleic anhydride are associated with coherent interfaces between $VOPO_4$ and $(VO)_2P_2O_7$ [26]. K. Ait-Lachgar et al. [37] oxidized a pure and well-crystallized $(VO)_2P_2O_7$ in oxygen flow at 500 °C for different times up to 24 hours. The samples were characterized by UV-VIS, XRD and NMR. While the oxidation state increased continuously, the selectivity had a maximum value at oxidation time of 1 hour. This led authors to the conclusion about the existence of an optimum density of V^{5+} species on top of $(VO)_2P_2O_7$ for MA production.

On the other hand, there also exist results from UV spectroscopy by Trifiro *et al.* [2, 38] indicating that a redox cycle between V^{3+} and V^{4+} is responsible for the selective oxidation. Also Gai *et al.* [39] presumed that V^{3+} species, which are located next to the oxygen defect sites, play important roles in selective oxidation of *n*-butane. However, based on the above requirements, vanadyl pyrophosphate would not be selective but only able to activate gaseous oxygen. It has been found indeed that pure $(VO)_2P_2O_7$ is active in butene oxidation but that many oxidized by-products are formed [40].

The problem of detection of the active species is further complicated by the huge variety of VPO phases and the easy transformation between different phases under oxidizing or reducing conditions or at varying temperatures.

2.5 Motivation and goal

One way to get a more profound understanding of the real catalyst and the role of the different phases involved in the reaction, is to reduce the complexity of the system by investigating the specific occurring phases in depth on their own. This work is focused on a combined, theoretical and experimental investigation of the electronic structure. A detailed knowledge of the electronic structure helps to understand spectral features recorded in core- and valence excitation spectroscopy. One example is the interpretation of systematic changes of spectral features observed during in situ low energy X-ray absorption spectroscopy performed under varying feed gas and temperature conditions [42]. Characteristic features of specific atom coordinations and chemical environment may be identified and traced throughout a variety of phases. This might be helpful in assisting the interpretation of spectral features recorded from unknown samples of unknown phase composition.

After introduction of the experimental and theoretical tools on which this thesis is based,

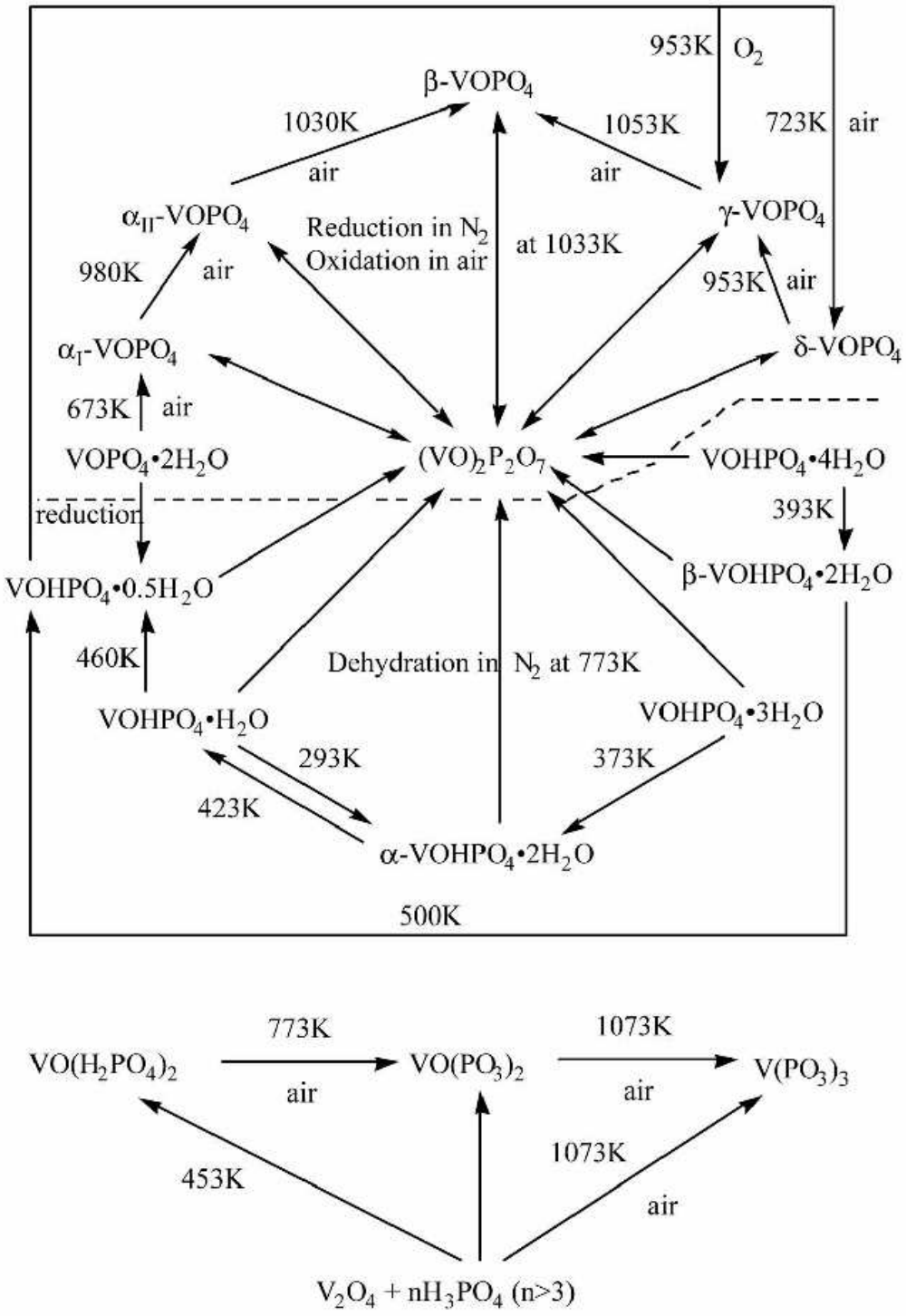

Fig. 2.4: Diagram of phase transformations among VPO catalysts and precursors. Taken from [41].

the electronic structure of some relevant VPO phases and of two polymorph of V_2O_5 will be presented (see Table 2.5). The phases have been chosen out of the huge number of VPO phases because: (i) they represent model systems, (ii) their unit cell parameters are known and (iii) the number of atoms in the unit cell is not too big for solving the electronic structure within the chosen theoretical approach.

V^{5+} phases	**α - and γ - V_2O_5:** layered structures, corner and edge linked VO_6 units, V V O — V, V — O — V and O — V bonds **β - $VOPO_4$, α_I - and α_{II} - $VOPO_4$:** corner linked VO_6 and PO_4 units, P — O — V and O — V bonds 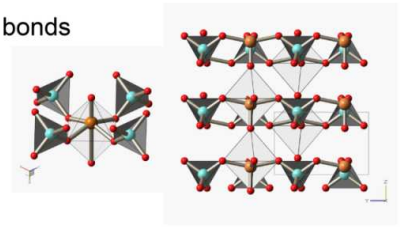
V^{4+} phases	**$VO(PO_3)_2$:** corner linked VO_6 and PO_4 units, P — O — P, P — O — V and O — V bonds **$VO(H_2PO_4)_2$:** corner linked VO_6 and PO_4 units, P — O — H, P — O — V and O — V bonds 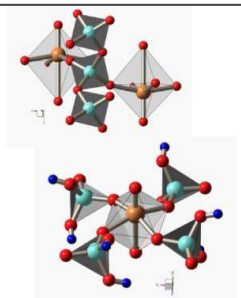
V^{3+} phases	**VPO_4:** chains of edge linked VO_6 units, V — O — P and V O — P bonds 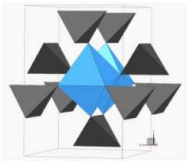

Fig. 2.5: Overview of the systems studied in this thesis. Some characteristic features of the phases are listed.

Chapter 3

Methods

In this chapter, the experimental and theoretical methods on which this thesis is based, are briefly introduced.

3.1 Experimental tools

3.1.1 TEM

Transmission electron microscopy (TEM) is analogous to optical transmission microscopy, but using an electron beam instead of visible light. The transmitted electron beam forms an image, which is a 2-dimensional projection of the 3-dimensional sample in the direction of the beam. In general, the attainable resolution is limited by the wavelength of the probing waves, which is 400-700 nm for visible light. The wavelength of the electron can be reduced to values suitable for imaging atomic features by accelerating electrons through high voltages (kV). A TEM provides highly coherent electrons of sufficient energy and the ability to investigate the sample in terms of its morphology, structure and orientation, combined with the advantage of high spatial resolution. The principle of a TEM is sketched in Fig. 3.1. Electrons emitted by the electron source are accelerated and pre-focused by the electron gun. After passing the illumination system and interaction with the sample, the electron beam passes the objective lens and enters the first and second intermediate lens and the final projector. Below the projector lens lies the fluorescent screen on which the image is rendered visible.

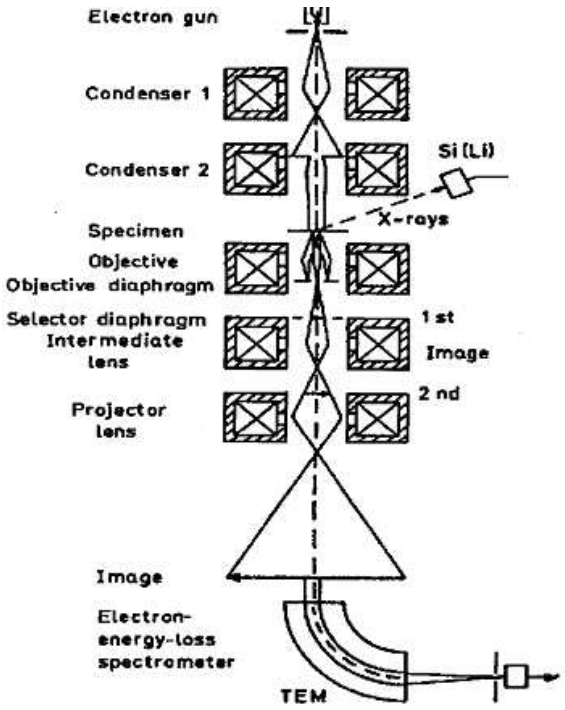

Fig. 3.1: Principal set-up of a Transmission Electron Microscope (TEM).

Electron Sources

There are two kinds of electron sources used in TEM's: tungsten or lanthanum hexaboride (LaB_6) cathodes as a source of thermally-emitted electrons and field-emission sources (FEG) where electrons are extracted from a cathode by applying an intense electric field to them. LaB_6 crystals have better characteristics than tungsten sources since they can be produced with a fine tip of about 1 μm in radius and they have a lower work function. This results in a small crossover size and considerably higher current density and an energy spread as little as 1 eV. In FEGs the current density is enormous, their extremely small source size means that the beam is highly spatially coherent and the resulting energy spread is minuscule. In all applications that require a bright, coherent source the FEG is best. On the other hand FEGs need UHV conditions which is expensive and requires a higher level of operator competence. The electron source is incorporated into a gun assembly which in effect acts as a lens to focus and accelerate the electrons according to the anode potential (usually 100kV to 200kV) and to direct them into the illumination system of the TEM.

Illumination system

The illumination system takes the electrons from the gun and transfers them to the specimen. It usually consists of the condenser aperture and two condenser lenses which project a demagnified image of the filament on the specimen. The lens current and hence, the focal length determine the beam convergence angle α and the brightness of the image. The point of least confusion is called crossover. If the image of the filament lies directly on the specimen, all emitted electrons contribute to the image and the brightness is highest. At the same time, the convergence angle is largest. If the condenser lens is over-focused, the image of the filament moves upwards and the specimen is illuminated from a rather great distance. This corresponds to a point-like and therefore parallel illumination with very small α and brightness. The condenser aperture is positioned between the condenser lenses. It limits the beam striking the specimen to protect it from excessive heating and also reduces the generation of X-rays.

Objective Lens

The objective lens is placed below the specimen. Electrons which have traversed the specimen are focused in the focal plane of the objective lens to form a Fraunhofer-diffraction

pattern. The first image of the specimen is formed in the first image-plane at a magnification of about 30 times. The objective aperture, also called contrast aperture, is placed in the back focal plane of the objective lens. It allows to select various Fourier-components of the image and defines a maximal scattering angle in order to increase the contrast. In the so-called bright-field mode, the contrast aperture selects the [000] spot and excludes all electrons that were Bragg-scattered to higher angles, whereas in the dark-field mode the image is formed only from scattered electrons. The possibility to select electrons according to a certain range of scattering angle allows to point out sample areas with different scattering characteristics like crystal defects in mono-crystals or micro-crystals of different orientation in polycrystalline samples.

Intermediate Lenses

The objective lens is followed by two or three intermediate lenses which, depending on their focal length, define the TEM operation mode. A sketch of ray-tracing through a TEM for the two basic operation modes is given in Fig 3.2. In image mode, the object plane of the intermediate lenses is the image plane of the objective lens. An objective aperture allows to select or decrease the range of scattering angles contributing to the formation of the final image.

In diffraction mode, the back focal plane of the objective lens which contains the diffraction pattern acts as the object plane for the intermediate lenses. In this mode, the diffraction pattern resulting from a specimen region controlled by the SAD-aperture are projected onto the viewing screen. Finally, the projector projects the image of the intermediate lenses (i.e. either an image of the specimen or its diffraction pattern) onto a fluorescent screen, into the camera system or the EELS-spectrometer which are both placed below the viewing screen.

3.1.2 EELS

Electron Energy Loss Spectroscopy (EELS) is an established technique for investigating the electronic structure in solids. The principle is quite simple: The energy distribution of initially mono energetic electrons is analyzed after they have interacted inelastically with a specimen. These inelastic collisions reveal a tremendous amount of information about the electronic structure of the specimen atoms and hence, details of the nature of these atoms, their bonding and nearest-neighbor distributions, and their dielectric response.

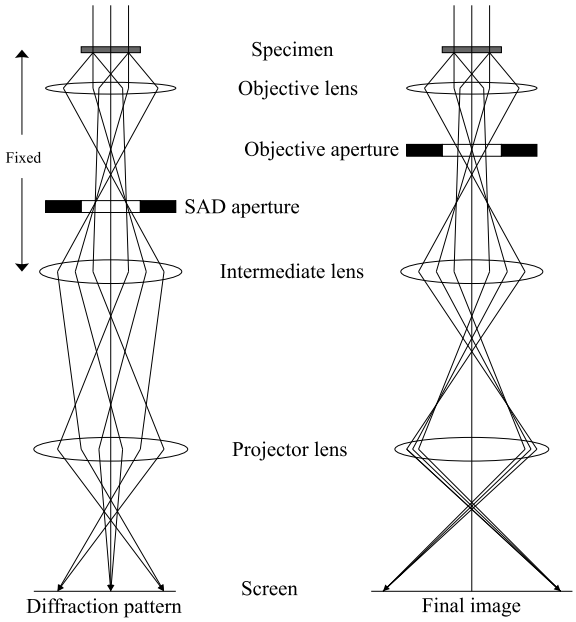

Fig. 3.2: Sketch of ray-tracing through a TEM for the two basic operation modes. Left: diffraction mode, right: imaging mode. The selected-area diffraction (SADF) aperture controls the area from which the diffraction is produced.

Provided that the incident energy is high enough and the specimen is sufficiently thin, practically all of the incident electrons are transmitted without reflection or absorption. Interaction takes place inside the specimen and information about the internal structure can be obtained by passing the transmitted beam into a spectrometer. Transmission EELS is usually carried out in a TEM, which allows high spatial resolution and also offers imaging and diffraction capabilities that can be used to identify the structure of the analyzed material. The obtained spectra are within limits (dipole approximation must be fulfilled) similar to the spectra recorded in the near edge region of X-ray absorption measurements (NEXAFS), which are usually performed at a synchrotron. The advantage of EELS with respect to NEXAFS is the high spatial resolution combined with the structural and morphological information simultaneously provided by the TEM and the availability, lower prize and smaller size of the TEM with respect to a synchrotron.

Interaction of fast Electrons with a Solid

When electrons enter a material, they interact with the constituent atoms via electrostatic forces. These coulomb interactions lead to changes of direction and momentum of the incident electrons, i.e. the electrons are scattered. Electron scattering can be divided into two categories: elastic and inelastic. Elastic scattering involves processes where the internal energy of both, the probe electron and the target, does not change or is negligible small. That is the case in interactions of incident electrons with the electrostatic field of an atomic nucleus, since a nucleus is some thousands of times more massive than an electron.

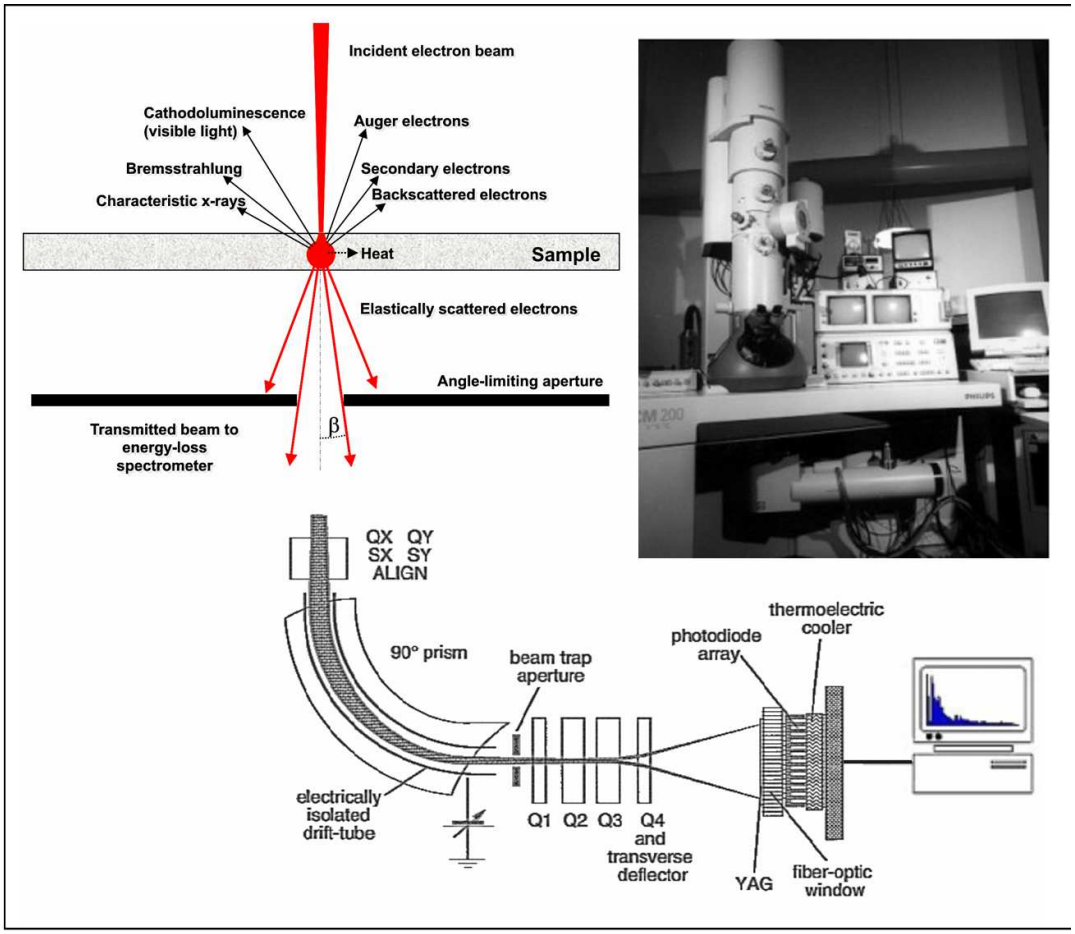

Fig. 3.3: The principle of electron energy loss spectroscopy

Inelastic scattering occurs as a result of Coulomb interaction between a fast incident elec-

tron and the atomic electrons surrounding each nucleus. Some inelastic processes can be understood in terms of the excitation of a single atomic electron into a free state in a Bohr orbital of higher quantum number or, in terms of energy-band theory, to a higher energy level. Other inelastic processes are interband transitions of valence or conduction electrons, excitation of phonons or plasmons, etc. In an inelastic process, the internal energy of the specimen is changed. The change is equal to the energy loss of the probe electron.

The EELS Detector

EELS spectra are recorded with the Gatan Imaging Filter GIF 100. The energy resolution is 0.9 to 1 eV (FWHM of the zero loss). The Gatan Imaging Filter (GIF) is mounted to the bottom of the camera chamber of the TEM. It allows images and diffraction patterns produced by the TEM to be transformed into energy-filtered (energy-selected) images and diffraction patterns. It can also form energy loss spectra with a range of energy dispersions. The images, diffraction patterns or spectra can be observed in real-time via a TV-rate CCD camera or can be acquired by a Slow-Scan CCD camera directly into a computer. Electrons are selected by a variable entrance aperture of 3.0 mm, 2.0 mm or 0.6 mm in diameter.

After passing the entrance aperture the electrons travel down a 'drift tube' through the spectrometer and are deflected through 90° on the basis of the velocity-dependent Lorentz-force. Electrons with greater energy loss are deflected further than those suffering zero loss. A spectrum is thus formed in the dispersion plane which consists of a distribution of electron counts versus energy loss. Besides bending the electron beam and creating energy dispersion, the magnetic prism also has a focusing action and at some distance behind the prism, an energy dispersed, focused image of the TEM's projector lens crossover is formed. This is the energy-loss spectrum.

A quadrupole-sextupole assembly is mounted at the end of the prism. It can be operated in two modes: In image mode, it takes the electrons which were selected by an energy-selecting slit located in the plane of the focused energy-loss spectrum and projects an energy-selected version of the TEM image onto the cameras. In spectroscopy mode, the quadrupole-sextupole assembly projects the focused energy loss spectrum onto the cameras.

The Electron Energy-Loss Spectrum

The beam of electrons that have transmitted the sample is directed into the EELS detector which separates the electrons according to their kinetic energy and produces an electron energy loss spectrum showing the scattered intensity (electron counts) as a function of the decrease in kinetic energy of the incident fast electron. A typical loss spectrum of vanadium pentoxide is shown in Fig. 3.4.

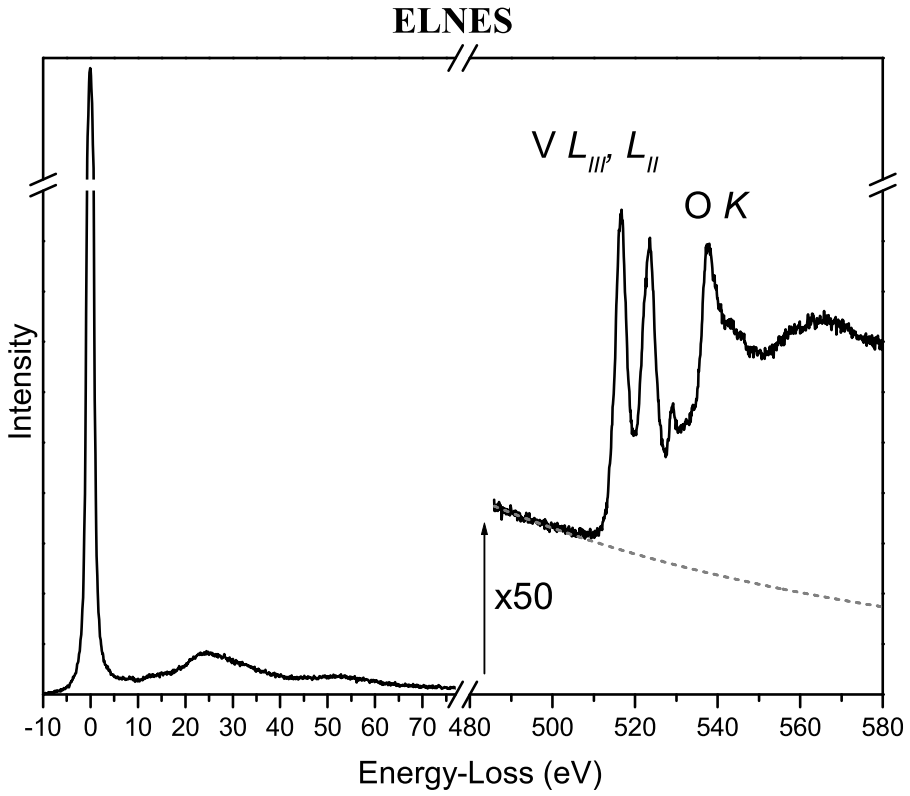

Fig. 3.4: Energy-loss spectrum of a VPO sample showing the low-loss region and ionization edges of oxygen (K edge) and vanadium (L_{III} and L_{II} edge). The intensity scale at the core-loss region is multiplied by a factor 50.

The first zero-loss or elastic peak represents electrons which are transmitted without suffering any measurable energy loss, including those which are scattered elastically in the forward direction and those which have excited phonon modes, for which the energy loss is less than the experimental energy resolution. The low-loss region up to an energy loss of about 50 eV contains electrons which have interacted with the weakly bound

outer-shell electrons of the atoms in the specimen, i.e. electrons that have set up plasmon oscillations or have generated inter- or intra-band transitions. Plasmons are longitudinal wave-like oscillations of weakly bound electrons. The plasmon peak is the second most dominant feature of the energy-loss spectrum after the zero-loss peak.

Electrons in the high-loss region have interacted with the more tightly bound inner-shell or core electrons to move it outside the attractive field of the nucleus. In this process, the atom is said to be ionized. The ionization losses are characteristic of the atom involved and so the signal is a direct source of elemental information, just like the characteristic X-rays. When viewed in greater detail, both the valence-electron (low-loss) peaks and the ionization edges possess a fine structure which reflects the crystallographic or energy-band structure of the specimen. Therefore, an element or compound that occurs in different forms shows quite distinct fine structures. If the energy loss spectrum is recorded from a sufficiently thin region of the specimen, each spectral feature corresponds to a different excitation process. In thicker samples, there is a reasonable probability that a transmitted electron will be inelastically scattered more than once, giving a total energy loss which is the sum of the individual losses. In the case of plasmon scattering, the result is a series of peaks at multiples of the plasmon energy.

The Spectral Background to Inner-Shell Edges

Each ionization edge in the energy loss spectrum is superimposed on a downward sloping background which arises from other energy-loss processes like plural scattering events which are usually associated with outer-shell interactions. The background appears as a rapidly changing continuum, decreasing from a maximum just after the plasmon peak at about 15 to 25 eV, down to a minimum at which it is indistinguishable from the instrumental noise. In addition to plural scattering, there are also single-scattering contributions to the background from the tails of preceding ionization edges. The background has to be subtracted when carrying out elemental analysis or interpreting core-loss fine structure. Since the background intensity is often comparable to, or larger than the core loss intensity, accurate subtraction of the background is essential. That is usually performed by selecting a window in the background before the edge onset in the spectrum and fitting a curve to the channels. This curve is then extrapolated by the EL/P software [43] over the desired energy window under the edge. For a good fit, the routine requires a range comprising at least 10 channels of the pre-edge background.

Plural Scattering

If the specimen thickness is much less than the mean free path for all inelastic scattering, the probability of a transmitted electron being scattered inelastically by valence electrons (as well as exciting an inner shell) is small. In thicker samples, this condition no longer applies and a broad double-scattering peak appears at an energy loss of approximately $E_K + E_P$, where E_P is the energy of the "plasmon" peak observed in the low-loss region and E_K is the energy of an ionization edge. In thicker specimens, higher-order satellite peaks merge with the double-scattering peak to produce a broad hump beyond the edge, completely transforming its shape and obliterating any fine structure. Within limits, such plural scattering can be removed from the spectrum by deconvolution [43, 44].

Absorption Edges

Excitations from inner shells of atoms give rise to absorption edges in Energy Loss Spectroscopy similar to the well-known X-ray absorption edges. In general these edges occur at energies E $\geq$ 50 eV for most elements, which is far beyond the interaction energy of valence electrons in the solid state. This allows to treat the target electrons as bound to single nuclei, not interacting with other atoms. On the other hand, valence or conduction electrons interact strongly with one another and influence the low loss region E $\leq$ 20 eV.

Energy-level diagram of a solid, including K- and L- shell core levels and a valence band of delocalized states (shaded); EF is the Fermi level and Evac the vacuum level. The primary processes of inner- and outer-shell excitation are shown on the left, secondary processes of photon and electron emission on the right.

The Beam Collection and Convergence Angle

Detailed intensity variations in the spectrum depend on the range of electron scattering angles which are gathered by the spectrometer. In order to investigate anisotropy in the local final DOS with EELS, the spectrometer collection angle is an important variable: In case of a small collection angle, EELS probes states which are polarized parallel to the incident beam. In case of a larger collection angle, additional excitations into orbitals pointing in a direction perpendicular to the incident beam contribute to the spectrum. In order to give a reasonable interpretation of the fine structure in EELS measurements, the dipole approximation must be fulfilled and, additionally, the spectrometer collection

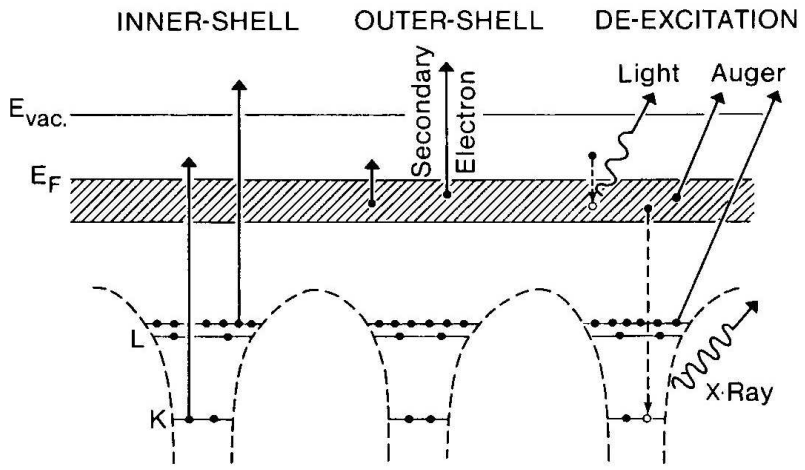

Fig. 3.5: Energy-level diagram of a solid, including K- and L- shell core levels and a valence band of delocalized states (shaded); E_F is the Fermi level and E_{vac} the vacuum level. The primary processes of inner- and outer-shell excitation are shown on the left, secondary processes of photon and electron emission on the right. Image was taken from [44].

angle must be known. The angular dependence of the spectra allows qualitative determination of the orientation of orbitals to which spectral features correspond.

3.1.3 Experimental details

All HRTEM and EELS measurements were performed with a Philips CM 200 field emission transmission electron microscope equipped with a Gatan energy flter. The microscope was operated at 200 kV. The energy resolution, estimated from the full-width at half maximum of the zero-loss peak, was 0.9 to 1 eV. Generally, spectra were recorded at an illumination angle in the range of 1.3 - 1.5 mrad and a collection angle of 9.8 mrad. For additional investigations of the morphology and atomic ratio of the samples, a Hitachi S-400 scanning electron microscope (SEM) equipped with an energy disperse X-ray detector was used. Phase analysis was performed using and a Stoe Power Diffractometer with a position sensitive detector in 2θ geometry.

3.2 Theoretical Tools

3.2.1 Molecular Orbitals

Molecular orbital (MO) theory deals with the formation of molecular orbitals from the overlap of atomic orbitals. The key points regarding the interaction of two atomic orbitals (χ_1 and χ_2) to form two molecular orbitals (Ψ_1 and Ψ_2) are:

1. The number of MO´s is equal to the number of atomic orbitals, and each MO can hold 2 electrons with opposite spins.
2. The overlap of two atomic orbitals is dependent upon:
   - symmetry of the orbitals
   - distance between orbitals
   - the energy difference between orbitals (E_1-E_2)
3. The stabilization of the bonding MO (Ψ_1) and destabilization of the antibonding MO (Ψ_2) increase as the overlap increases.
4. The destabilization of the antibonding MO is always greater than the stabilization of the bonding MO.
5. As the energy difference between χ_1 and χ_2 increases (with $E_1 < E_2$) the covalent stabilization decreases, the contribution of χ_1 (χ_2) to the bonding MO Ψ_1 (the antibonding MO Ψ_2) increases.

3.2.2 Linear Combination of Atomic Orbitals

A standard method for solving the periodic potential problems in solids within Molecular Orbital theory (MO-theory) is the LCAO (Linear Combination of Atomic Orbitals) or Bloch or Tight Binding Method. Within this approach, the wave functions are expressed as a linear combination of atomic orbitals, located on the various atoms of the crystal. The coefficients of the expansion are the values of the plane wave. Space quantized orbitals such as the p_x, p_y and p_z combinations of p orbitals and the d orbitals varying as xy, yz, zx, $x^2 - y^2$, and $3z^2 - r^2$ are used as well as more complicated hybridized orbitals. The coefficients in the Bloch sum are the values of the plane wave $exp(i\vec{k}\vec{R})$ at the positions $\vec{R}$ at which the atoms are located. Starting with an atomic orbital $\chi_n(\vec{r} - \vec{R}_i)$, located on

an atom at vector position $\vec{R}_i$, and with quantum numbers symbolized by the subscript n, the Bloch sum can be written as:

$$\Psi_k \; = \; \sum_i exp(i\vec{k}\vec{R}_i)\chi_n(\vec{r} - \vec{R}_i) \tag{3.1}$$

where the sum goes over all atoms in equivalent positions in all the unit cells of the crystal. Such Bloch sums are constructed for each atomic orbital. The wave function for a given $\vec{k}$ value can then be composed by a linear combination of all these Bloch sums. In general, except at special $\vec{k}$ values, there will be matrix components of energy between the Bloch sums forming a secular problem whose order equals that of the total number of atomic orbitals. These secular equations can be solved, and the resulting wave functions and energy levels form useful approximations to the solution of the periodic potential problem.

Crystal field theory

Crystal-filed theory (CFT) was developed by Hans Bethe in 1929 to account for the electronic structure and chemical properties of d metal ions in ionic crystals [45]. In CFT, a ligand-lone pair is idealized as a point negative charge repelling the d electrons in the orbitals of the central metal ion due to purely electrostatic interactions. The five d orbitals in an isolated gaseous metal are degenerate. If a spherically symmetric field of negative charges is placed around this metal ion, these orbitals remain degenerate, but all of them are raised in energy as a result of the repulsion between the negative charges on the ligands and the d orbitals. In case of a non-spherical symmetric crystal-field, the discrete point charges of the ligands interact differently with the d-metal ion orbitals, and thereby the degeneracy of the d orbitals is lifted, as shown for the case of an octahedral crystal field in Fig. 3.6. This model explains the splitting of the d orbitals in groups of different energies. The electrostatic energy is increased for d orbitals which are oriented toward the region of high electron density at a ligand; and likewise, the energy is lowered when the opposite is the case. The total crystal field splitting energy may be estimated by

$$D_{CFT} \approx \frac{r^4_{orbital}}{R^5_{metal-ligand}} \tag{3.2}$$

where $r_{orbital}$ is the radius of the d orbital and $R_{metal-ligand}$ is the metal-ligand internu-

clear distance. However, simple CFT ignores covalent interactions between the ligand and the central metal ion. Ligand-field theory accounts for this deficiency of CFT by including the overlap of d and ligand orbitals in form of molecular orbitals.

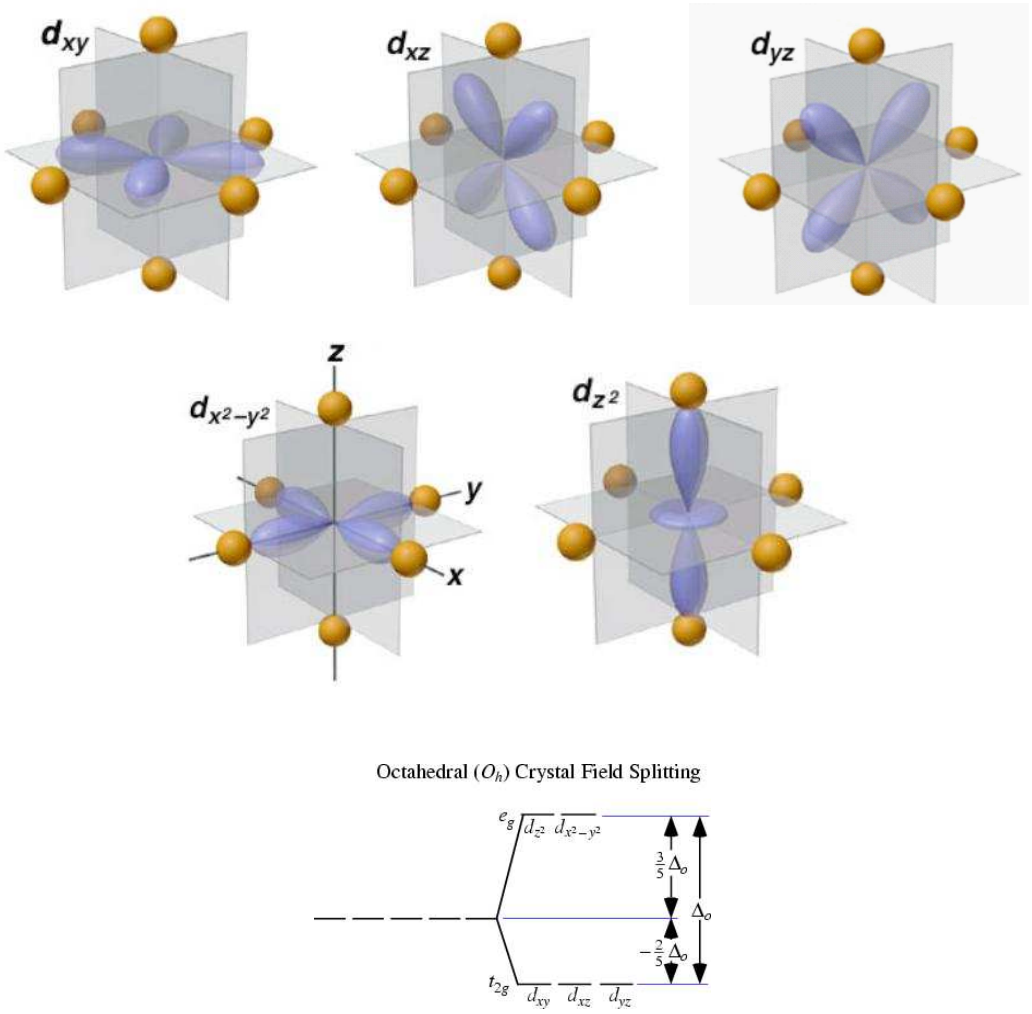

Fig. 3.6: The five d orbitals surrounded by ligands in an octahedral geometry and the resulting octahedral crystal field. Orbitals that have there lobes pointing toward the ligands are shifted upwards in energy with respect to those orbitals that have there lobes pointing in between the ligand atoms.

The Jahn-Teller Theorem

The Jahn-Teller Theorem was published in 1937 and states: "Any non-linear molecular system in a degenerate electronic state will be unstable and will undergo distortion to

form a system of lower symmetry and lower energy thereby removing the degeneracy". Out-of-center distortions of MO_6 octahedra in d^0 oxides, which are crucial to many of the interesting properties of the materials discussed in this thesis, have an electronic origin. In a typical d^0 oxide, valence band (which corresponds to the highest occupied molecular orbitals, HOMOs) is mainly anionic (oxygen $2s$ and $2p$), and the conduction band (which corresponds to the lowest unoccupied molecular orbitals, LUMOs) is mainly cationic, arising from the empty d states. For small and highly charged d^0 cations, the separation between the HOMO and the LUMO states becomes sufficiently small so as to permit a mixing between them that stabilizes the occupied states at the expense of the unoccupied states through a second-order Jahn-Teller effect [46]. The solid state counterpart of the Jahn-Teller distortion is referred to the Peierls distortion. In an octahedral crystal field, the t_{2g} orbitals occur at lower energy than the e_g orbitals (see Fig. 3.6). This is a reflection of the orientation of the orbitals since the t_{2g} are directed between bond axes while the e_g point along bond axes. The Jahn-Teller Theorem does NOT say how large a distortion should occur.

3.2.3 Density Functional Theory

Density-functional theory (DFT) is probably the most widely used computational electronic structure method today. The central quantities in DFT are the electron density $n(\vec{r})$ and the total energy E_{tot}.

In the following, the problem of evaluating quantum mechanically the ground state electronic density and total energy of a system of interacting electrons for a given nuclear configuration is briefly discussed.

3.2.4 The Kohn-Sham theorem

The key idea is to consider the electron density $n(\vec{r})$ as the basic variable. Hohenberg and Kohn [47] showed that ground state properties of a many-electron system can be expressed as functionals of the ground state electron density; i.e., they are determined by a knowledge of the density alone. The traditional formulation of the two theorems of Hohenberg and Kohn is as follows:

First theorem: *The ground-state energy of a many-body system is a unique functional of the particle density,* E_0.

Second theorem: *The functional E has its minimum relative to variations dn of the particle density at the equilibrium density n_0.*

An efficient and accurate scheme for solving the many-electron problem of a crystal is the Local Spin Density Approximation (LSDA) within density functional theory [47]. Therein the key quantities are the spin densities $\rho_\sigma(r)$ in terms of which the total energy is

$$E_{tot} \;=\; T_S + E_{ee} + E_{Ne} + E_{XC} + E_{NN} \tag{3.3}$$

with

T_S ...kinetic energy (of the non interacting particles),
E_{ee} ...electron-electron repulsion,
E_{Ne} ...nuclear-electron attraction,
E_{XC} ...exchange-correlation energies and
E_{NN} ...repulsive Coulomb energy of the fixed nuclei.

An approximation comprises the LSDA: the assumption that the exchange-correlation energy can be written in terms of a local exchange-correlation energy density μ_{XC} times the total electron density as

$$E_{XC} \;=\; \int \mu_{XC}(\rho\uparrow, \rho\downarrow) * [\rho\uparrow + \rho\downarrow] \tag{3.4}$$

Several forms for μ_{XC} exist in the literature [48, 49]. The minimum of E_{tot} can be found by a variational principle equivalent to the familiar Rayleigh-Ritz principle. Therefore orbitals χ^σ_{ik} are introduced, constrained to construct the spin densities as

$$\rho_\sigma(r) \;=\; \sum_{i,k} \rho^\sigma_{ik} \left|\chi^\sigma_{ik}(r)\right|^2 \tag{3.5}$$

where ρ^σ_{ik} are occupation numbers such that $0 \leq \rho^\sigma_{ik} \leq 1/\omega_k$, and ω_k is the symmetry required weight of point k within the first Brillouin zone.
With these assumptions, the variation of the total energy leads to the *Kohn-Sham* equations

$$\left[-\nabla^2 + V_{Ne} + V_{ee} + V^\sigma_{XC}\right] \chi^\sigma_{ik}(r) \;=\; \epsilon^\sigma_{ik}(r)\chi^\sigma_{ik}(r) \tag{3.6}$$

which must be solved self-consistently in an iterative process, since finding the *Kohn-Sham* orbitals requires the knowledge of the potentials which themselves depend on the (spin-) density and thus on the orbitals again.

The Full Potential LAPW Method

The LAPW method is a procedure for solving the *Kohn-Sham* equations for the ground state density, total energy, and (Kohn-Sham) eigenvalues (energy bands) of a many-electron system (a crystal) by introducing a basis set which is especially adapted to the problem: The unit cell is divided into non-overlapping Muffin-Tin spheres (I), centered at the atoms and the remaining ”interstitial” region (II). Electrons in a solid are divided into ”valence” electrons and ”core” electrons.

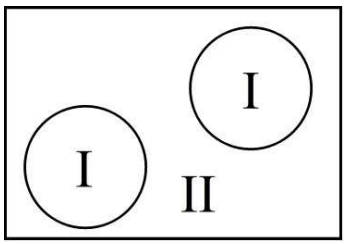

Division of the unit cell into non-overlapping Muffin-Tin spheres (I) and the remaining interstitial region (II)

Inside the atomic spheres (I) a linear combination of radial functions times spherical harmonics is used to characterize the core state:

$$\phi_{k_n} = \sum_{l,m} \left[A_{lm} u_l(r, E_l) + B_{lm} \dot{u}_l(r, E_l)\right] Y_{lm}(\hat{r}) \tag{3.7}$$

where $u_l(r, E_l)$ is the regular solution of the radial Schrödinger equation for the energy E_l and $\dot{u}_l(r, E_l)$ is the energy derivative of u_l. A linear combination of these two functions constitute the linearization of the radial function. The coefficients A_{lm} and B_{lm} are functions of k_n determined by requiring that this basis function matches the corresponding basis functions of the interstitial region. The solutions u_l and $\dot{u}_l$ are obtained by numerical integration of the radial Schrödinger equation on a radial mesh inside the sphere. In the interstitial region (II) the Bloch state is described by a superposition of plane waves

$$\phi_{k_n} = \frac{1}{\sqrt{\omega}} exp(i\vec{k}_n\vec{r}) \tag{3.8}$$

where $\vec{k}_n = \vec{k} + \vec{K}_n$ and $\vec{K}_n$ are the reciprocal lattice vectors and $\vec{k}$ is the wave vector inside the first Brillouin zone. Each plane wave is augmented by an atomic-like function in every atomic sphere. The solutions to the Kohn-Sham equations are expanded in this combined basis sets of LAPW's according to the linear variation method

$$\Psi_k = \sum_n c_n \phi_{k_n} \tag{3.9}$$

and the coefficients c_n are determined by the Rayleigh-Ritz variational principle. The convergence of this basis set is controlled by a cut-off parameter $R_{mt}K_{max}$ which lies between 6 and 9. R_{mt} is the smallest atomic sphere radius in the unit cell and K_{max} is the magnitude of the largest k vector in equation 3.9. In order to improve upon the linearization (i.e. to increase the flexibility of the basis) and to allow a consistent treatment of semi-core and valence states in one energy window (to ensure orthogonality) additional k_n independent basis functions can be added. They are called local orbitals and consist of a linear combination of two radial functions at two different energies (e.g. at the $3s$ and $4s$ energy) and one energy derivative (at one of these energies):

$$\phi_{lm}^{LO} = \left[A_{lm}u_l(r, E_{1,l}) + B_{lm}\dot{u}_l(r, E_{1,l}) + C_{lm}u_l(r, E_{2,l})\right] Y_{lm}(\hat{r}) \tag{3.10}$$

The coefficients A_{lm}, B_{lm} and C_{lm} are determined by the requirements that ϕ^{LO} should be normalized and have zero value and slope at the sphere boundary.

In its general form the LAPW method expands the potential in the following form:

$$V(r) = \begin{cases} \sum_{lm} V_{lm}(r)Y_{lm}(r) & \text{inside sphere} \\ \sum_k V_k exp(iKr) & \text{outside sphere} \end{cases} \tag{3.11}$$

The charge densities are expanded analogously. Since no shape approximations are made, the procedure is frequently called the *Full Potential* LAPW (FP-LAPW) method.

3.2.5 The SCF scheme

The basic idea of the self consistent field cycle (SCF) is simple (see Fig. 3.7). Some starting density ρ^{in} is guessed and the average field seen by each electron is calculated. From this, a hamiltonian H_{KS1} is constructed. The eigenvalue problem is solved, and results in a set of spin orbitals from which a new density ρ_1 can be derived. Most probably ρ_1 will differ

from ρ^{in}. Now ρ_1 is used to construct H_{KS2}, which will yield a ρ_2, etc. The procedure can be set up in such a way that this series will converge to a density ρ_f which generates a H_{KSf} which yields as solution again ρ_f : this final density is then consistent with the hamiltonian.

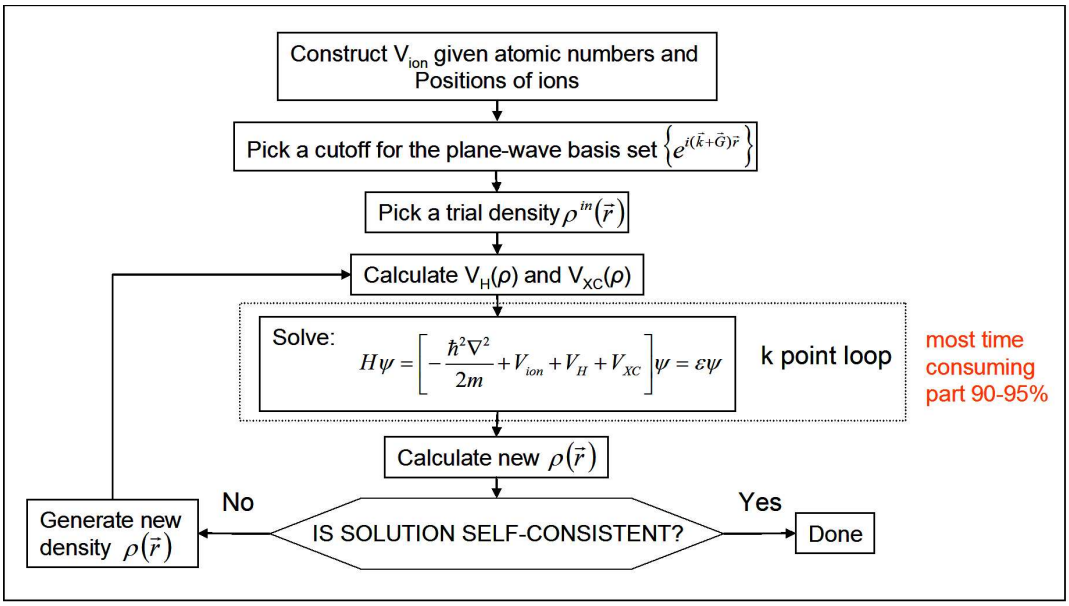

Fig. 3.7: The SCF procedure.

3.2.6 Simulation of ELNES

In the following, the probability for inelastic scattering of electrons on atoms is calculated as a function of energy and momentum transfer. The scattering probability is the differential cross section which is measurable directly in energy loss experiments. Since the probability depends on the nature of the scatterer, measuring $\partial^3\sigma/\partial\Omega\partial E$ yields information about the target atoms.

According to Fermi's golden rule, the transition probability of a system going from an initial state $|i\rangle$ to a final state $|f\rangle$ by the influence of some perturbation operator V is proportional to the square of the transition matrix element. The rule is derived in time dependent perturbation theory and gives the transition rate W (transitions per unit time).

$$dW_{fi} = \frac{2\pi}{\hbar} |\langle f|V|i\rangle|^2 \, dv_f \cdot \delta\left(E_i - E_f\right) \tag{3.12}$$

where

dW_{fi}	...number of transitions from unperturbed state $\|i\rangle$ to state $\|f\rangle$ within dv_f around $\|f\rangle$ per unit time (transition rate),
V	...perturbing potential,
dv_f	...differential phase space element around $\|f\rangle$ and
$\|i\rangle$, $\|f\rangle$	...are unperturbed initial and final state.

The differential particle current of free electrons scattered into$(d\Omega, dE)$ can now be calculated by summing (3.12) over all possible final states $|f\rangle$:

$$\begin{aligned} dj &= \frac{\partial W}{\partial\Omega\partial E} d\Omega dE = dj\left(dE, d\Omega\right) = \\ &= \sum_f \frac{2\pi}{\hbar} \left|\langle f|V|i\rangle\right|^2 \frac{k_f m}{\hbar^2} d\Omega dE \delta\left(E_i - E_f\right) \end{aligned} \tag{3.13}$$

since $dv_f = k_f^2 dk_f d\Omega$ and $E = \frac{\hbar^2 k^2}{2m}$ for free states $|f\rangle$.

With $dj = d\sigma(E,\Omega) \cdot j_i$, where $d\sigma = dE d\Omega \cdot \partial^2\sigma / \partial E \partial\Omega$ is the scattering cross section and j_i is the incident particle current, the cross section can be written as

$$\frac{\partial^2\sigma}{\partial E \partial\Omega} = \sum_f \frac{2\pi k_f m}{\hbar^3 j_i} \left|\langle f|V|i\rangle\right|^2 \delta\left(E_i - E_f\right) \tag{3.14}$$

The incident electrons are free particle eigenstates $|k\rangle$, normalised such that $\langle k'|k\rangle = \delta^3\left(\vec{k} - \vec{k'}\right)$:

$$\left\langle \vec{r}|\vec{k}\right\rangle = (2\pi)^{\frac{3}{2}} \exp\left(i\vec{k}\vec{r}\right) = \varphi\left(\vec{r}\right) \tag{3.15}$$

The quantum mechanical current density is

$$j_i = \frac{\hbar}{2mi}\left(\varphi^* \nabla\varphi - \varphi\nabla\varphi^*\right) = \frac{\hbar k_i}{\left(2\pi\right)^3 m} \tag{3.16}$$

and hence,

$$\frac{\partial^2\sigma}{\partial E \partial\Omega} = \left(\frac{2\pi}{\hbar}\right)^4 \sum_f \frac{k_f}{k_i} \left|\langle f|V|i\rangle\right|^2 \delta\left(E_i - E_f\right) \tag{3.17}$$

In elastic scattering, both, initial and final state are considered free states, and V is a static potential.

Inelastic scattering can be treated similarly when V represents the interaction potential between the probe and the target charges. Then $|i\rangle$ and $|f\rangle$ in (3.12) resemble many particle state vectors, including the target atoms.

The Dynamic Form Factor

The approximation that leads to the transition rate W_{fi} (3.12) is is only valid if the perturbation V is small compared to the energy of the scattered electrons, i.e. for fast collisions. In this case the unperturbed state vectors can be approximately factorized, since exchange effects are negligible:

$$|i\rangle = |k_i\rangle \otimes |\varphi_i\rangle\,, \qquad |f\rangle = |k_f\rangle \otimes |\varphi_f\rangle\,, \tag{3.18}$$

k_i, k_f are free states, φ_i and φ_f are the eigenfunctions of the electrons bound to the target nucleus before and after the collision.

The interacting potential representing the electrostatic forces between an incident electron and an atom can be written as

$$V = \frac{-Ne^2}{r} + \sum_{i=1}^{N} \frac{e^2}{|\vec{r} - \vec{r}_i|} \tag{3.19}$$

where the first term represents Coulomb attraction by the nucleus and the second term is a sum of the repulsive effects of each atomic electron at coordinate r_i. (This form for the potential is allowed as long as inner shell excitations are considered and the target can be thought of as an arrangement of non-interacting atoms).

Inserting the unity operator $\mathbf{1} = \int d^3r\, |\vec{r}\,\rangle \langle \vec{r}|$ into the transition matrix element $\langle f\,|V|\,i\rangle$ leads, with

$$\left\langle \vec{r}\,|\vec{k}\right\rangle = (2\pi)^{-\frac{3}{2}} \exp\left(i\vec{kr}\right) \tag{3.20}$$

to:

$$V_{fi} = \int d^3r_1 \dots d^3r_N \varphi_f^* (\vec{r}_1 \dots \vec{r}_N) \varphi_i (\vec{r}_1 \dots \vec{r}_N) \cdot \cdot d^3r V (\vec{r}; \vec{r}_1 \dots \vec{r}_N) \frac{\exp\left(i \left(\vec{k}_i - \vec{k}_f\right) \vec{r}\right)}{(2\pi)^3} \tag{3.21}$$

The d^3r integration can be performed by substituting $\vec{r'} = \vec{r} - \vec{r}_i$ in (3.19) and using the Fourier transform of the Coulomb potential:

$$\int d^3r \frac{e^2}{|\vec{r} - \vec{r}_i|} \exp\left(i\vec{Q}\vec{r}\right) = \frac{4\pi e^2}{Q^2} \exp\left(i\vec{Q}\vec{r}\right) \tag{3.22}$$

where $\vec{Q} = \vec{k}_i - \vec{k}_f$ is the wave vector transferred during the interaction.

Finally, the differential cross section can be written as:

$$\frac{\partial^2 \sigma}{\partial E \partial \Omega} = \left(\frac{2me^2}{\hbar^2 Q^2}\right)^2 \frac{k_f}{k_i} S \tag{3.23}$$

where

$$\begin{aligned} S &:= \sum_{\varphi_f} \left| \left\langle \varphi_f \left| \sum_{i=1}^{N} \exp\left(i\vec{Q}\vec{r}_i\right) \right| \varphi_i \right\rangle - N \underbrace{\langle \varphi_f | \varphi_i \rangle}_{0} \right|^2 \cdot \delta\left(E_{\varphi_i} - E_{\varphi_f} + E\right) = \\ &= \sum_{\varphi_f} \left[\int d^3r_1 \dots d^3r_N \varphi_f^* (r_1 \dots r_N) \sum_{i=1}^{N} \exp\left(i\vec{Q}\vec{r}_i\right) \varphi_i (r_1 \dots r_N) \right]^2 \cdot \\ &\quad \cdot \delta\left(E_{\varphi_i} - E_{\varphi_f} + E\right) \end{aligned} \tag{3.24}$$

is the dynamic scattering form factor DFF.

$E = E_{\varphi_i} - E_{\varphi_f}$ in (3.24) is the energy loss. The term which is due to the Coulomb force of the nucleus vanishes since $|\varphi_i\rangle$ and $|\varphi_f\rangle$ are orthogonal. For small wave number transfers the scattering cross section is enhanced due to the appearance of the factor Q^{-4} in (3.23). The DFF is essentially a sum over transition probabilities between initial and final eigenstates belonging to the atoms Hamiltonian.

Under the assumption that the atomic description remains valid for the initial one-electron state in the solid, the initial state $|\varphi_i\rangle = |nlm\rangle$, represented by its quantum numbers n, l and m, can be written as a product of radial function and spherical harmonics:

$$\left|\vec{R}\right\rangle = u_{nl}(R)Y_{lm}(\widetilde{R}). \tag{3.25}$$

By assuming that the initial core-level state is completely sharp in energy and contributions from different n and l are sufficiently separated in energy, the sum in 3.24 must only go over degeneracy m, as well as the two magnetic spin quantum numbers.

According to the Bloch theorem, the final state $|\varphi_f\rangle$ is characterized by $\vec{k}$ and ν, where $\vec{k}$ is the wave vector in the first Brillouin zone and ν is the band index of the atomic electron. In contrast to the initial state, the final-state wave function is completely delocalized over the whole crystal. However, due to the strong localization of the core electron, which is confined to a sphere of radius R_t (region I) and due to the fact that the overlap of initial and final states vanishes outside of the spheres, the Bloch-electron has to be described only within the sphere.

The Bloch state $\left|\vec{k}\nu\right\rangle$ within the spheres is described by a superposition of plane waves:

$$\Psi^t_{\vec{k}\nu}(\vec{R}) = \sum_{l'm'} D^t_{l',m'}(\vec{k}\nu)u_{l'}(E_{\vec{k}\nu},R)Y_{l'm'}(\widetilde{R}) \tag{3.26}$$

where the expansion coefficients $D^t_{l',m'}(\vec{k}\nu)$ are defined by the required continuity of the wave function at the sphere boundary. The APW approach thus explicitly uses projections of the Bloch states on atomic basis functions defined inside of the spheres where the core states are localized. Inserting 3.26 into the DFF 3.24 and making use of the Rayleigh expansion

$$exp(i\vec{Q}\vec{R}) = 4\pi\sum_{\lambda=0}^{\infty}\sum_{\mu=-\lambda}^{+\lambda} i^\lambda Y^\lambda_\mu(\widetilde{Q})^* Y^\lambda_\mu(\widetilde{R})j_\lambda(QR) \tag{3.27}$$

results in the DFF for the ionization of atom t [50].

A physical foundation of the DFF, S, rises from the fact that $\sum_j \exp(i\mathbf{Q}\mathbf{r}_j)$ is the Fourier transform of the electron density operator $n(\mathbf{r})$ of the target:

$$n_{\mathbf{q}} := \int d^3r \exp\left(-i\vec{Q}\vec{r}\right) n\ (\mathbf{r}) = \int d^3r \exp\left(-i\vec{Q}\vec{r}\right) \sum_j \delta\left(\vec{r} - \vec{r}_j\right) =$$
$$= \sum_j \exp\left(-i\vec{Q}\vec{r}_j\right) \tag{3.28}$$

It can be shown, that $S(q,\omega)$ is the space-time Fourier transform of the density autocorrelation and hence, that inelastic scattering of electrons measures the temporal and spatial variations of the charge density correlation.Therefore it contains information on the charge density variations. But the charge density can not be retrieved unambiguously from measurements since different density profiles may deliver the same correlation function. The lost information is hidden in the phase of $\left\langle \varphi_f \left| \sum_{i=1}^{N} \exp\left(-i\vec{Q}\vec{r}_i\right) \right| \varphi_i \right\rangle$.
In order to calculate the electronic states and energies that appear in (3.24) the DFT plane wave total energy code WIEN2k is used [51].

Dipole Approximation

As described above, the double differential cross section can be written within the first Born approximation as

$$\frac{\partial^2\sigma}{\partial E \partial\Omega} = \left(\frac{2me^2}{\hbar^2 Q^2}\right) \frac{k_f}{k_i} \sum_{i,f} \left| \left\langle \varphi_f \right| \exp\left(i\vec{Q}\vec{R}\right) \left| \varphi_i \right\rangle \right|^2 \delta^2\left(E + E_{\varphi_i} - E_{\varphi_f}\right) \tag{3.29}$$

The operator which connects initial and final state can be expanded as

$$\exp\left(i\vec{Q}\vec{R}\right) = 1 + i\vec{Q}\vec{R} - \left(\vec{Q}\vec{R}\right)^2 + \text{plus higher order terms} \tag{3.30}$$

which allows (3.29) to be split into terms of different order in $\vec{Q}\vec{R}$. The first one, arising from the unity term in (3.30), is zero because the initial and the final state single electron wavefunctions $|\varphi_i\rangle$ and $|\varphi_f\rangle$ are orthogonal. The second component containing $\vec{Q}\vec{R}$ is zero if the initial and final state have the same symmetry about the center of the excited atom $\left(\vec{R} = 0\right)$: In this case, their product is even; $\vec{Q}\vec{R}$ itself is an odd function and the two halves of the integral cancel. But if $|\varphi_i\rangle$ and $|\varphi_f\rangle$ have different symmetry, which is the case, for example, in an initial s- and final p-state, transitions are observed. This forms the basis of the dipole selection rule. The third matrix component represents dipole-

forbidden transitions. If $\vec{Q}\vec{R} \ll 1$ then the higher order terms in (3.29) can be neglected and the matrix element reduces the dipole form:

$$\left\langle \varphi_f \left| \vec{Q}\vec{R} \right| \varphi_i \right\rangle \tag{3.31}$$

In this form the matrix element is similar to the dipole matrix element for the absorption of polarized electromagnetic radiation. The condition for the dipole approximation is fulfilled in the case of small scattering angles. This implies that $\vec{Q} \ll r_C^{-1}$, where r_C is the radius of the core state defining the spatial region in which most of the transitions occur. The dipole form of the matrix element requires that selection rules apply and hence, the relation between angular momentum in the initial state ℓ and final state ℓ' is $\ell' = |\ell \pm 1|$.

In case of an initial s symmetry the final state must therefore be of p symmetry:

$$\left\langle \varphi_f \left| \vec{Q}\vec{R} \right| s \right\rangle = Q \left\langle \varphi_f \left| z \right| s \right\rangle = Q \left\langle p_z | p_z \right\rangle, \qquad \text{if} \quad \vec{Q} = \vec{z}Q \tag{3.32}$$

The TELNES package

The program TELNES makes use of wave functions derived from WIEN2k. It accounts both for orientation and anisotropy of the specimen and for integration over collection and convergence angles in the experiment. The program permits interpretation of ELNES spectra where the final state is a projection of the DOS onto a certain direction defined by the transferred momentum $\vec{Q}$, i.e. an interpretation in terms of (l, m)-like final DOS. Thus, the advantage of the WIEN2k code, namely providing final states characterized by (l, m) quantum numbers, is fully preserved.

3.2.7 Band structure calculations

All electronic structure calculations presented in the following chapters were performed with WIEN2k. Simple unit cells were used for the calculations combined with three-dimensional periodic boundary conditions, ensuring a proper inclusion of the space-group symmetry. In all simulations, the generalized gradient approximation (GGA) was used for the exchange-correlation potential [52]. For the generation of electron density plots, the program XCrysden was used [53] The near edge structure of ionization edges in EELS spectra were simulated using the TELNES program which is included in the WIEN2k package [50]. For the presented DOS, a Gaussian smearing with a line width of

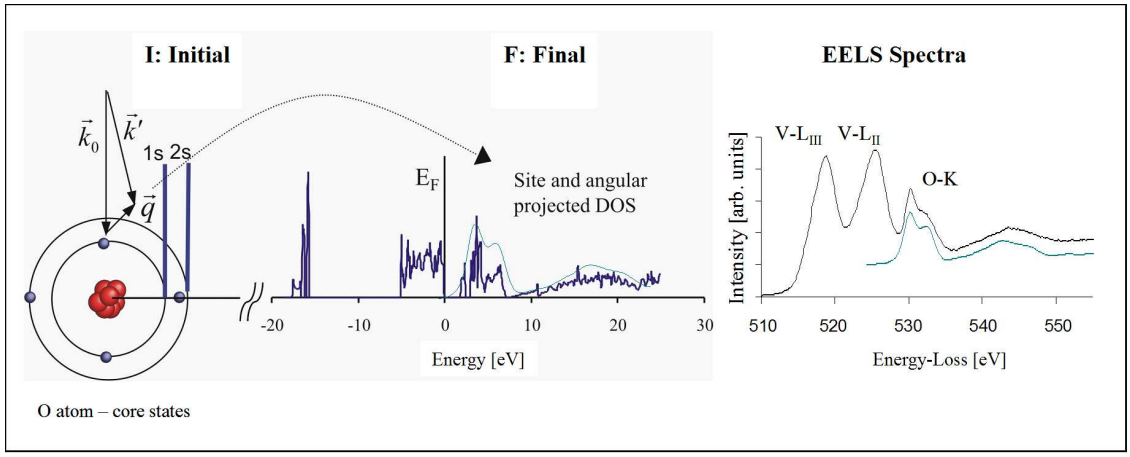

Fig. 3.8: Sketch of an e^- excitation from a core state into an empty state due to interaction with an electron from the incident beam.

0.04 eV was used in the calculations. The discussion of the DOS is focused on the valence and lower conduction bands, while the DOS of the core and semi core regions are not discussed.

Chapter 4

Geometric and electronic structure of α- and γ-V_2O_5

In this chapter the electronic structure of two polymorph of V_2O_5 will be discussed in view of differences in their geometric structure. The aim is to compare the basic structural VO_5 units in γ-V_2O_5 and α-V_2O_5 with respect to differences in their geometric and electronic structure. A detailed understanding of the relation between geometric and electronic structure is essential since this basic structural unit is also found in the VPO phases that are relevant in view of selective oxidation of n-butane [26]. These two compounds serve therefore as simple model systems for the discussion of more complicated vanadium phosphorus oxides in the succeeding chapters. The electronic structure of γ-V_2O_5 has not been studied in the past.

Some general features of d^0 metal oxides

In general, the crystal structures of d^0 metal oxides consist of distorted metal oxygen (MO_6) octahedra which are connected through corners and edges. Within the octahedra, the cation is displaced from the center of the octahedron (Jahn-Teller distortion). The occurrence of layered structures and distinct oxidehydrates for V_2O_5, MoO_3 and Re_2O_7 is a direct consequence of the distortion [54]. One special feature of this materials is that their d^0 cation, which is in its highest oxidation state, can be reduced partially or wholly in many instances. Thereby crystallographic shear processes operate such that the oxygen vacancies are eliminated without changing the octahedral coordination of the

metal atom.

The displacement is a result of the energy gained by shortening one of the M-O bonds with respect to the long and relatively more ionic (more basic) M-O bonds. The long M-O bonds become vulnerable to scission and the basic oxygens susceptible to electrophilic attack, for example, by protons. Formation of well defined hydrates is a direct manifestation of the reactivity of long M-O bonds of the distorted MO_6 octahedra. The consequences of the short M-O bonds in d^0 oxides are more impressive. Since the oxygen of the shortest M-O bond in a distorted octahedron is acidic relative to other oxygens, protons (or H_3O^+ ions) attached to this oxygen acquire a distinct Brønsted acidity.

4.1 The electronic structure α- and $\gamma-V_2O_5$

Divanadium pentoxide serves as an important model system for butane oxidation. It presents a well determined surface morphology and a high crystalline order containing the oxidation state V^{5+}. Consequently, the electronic and structural properties of α-V_2O_5 have been widely studied [55–58]. γ-V_2O_5 is a polymorph of the most common known α-V_2O_5 phase and was first reported in 1991 by Cocciantelli *et al.* who investigated charging and decharging cycles of LiV_2O_5 batteries [59]. While the electronic behavior of γ-LiV_2O_5 [60] has been modeled by means of DFT, the electronic structure of γ-V_2O_5 remained untouched. The synthesis of γ-V_2O_5 nanowires and nanorods by the reverse micelle technique is interesting in view of catalysis because it opens access to a geometrically well-defined nanosized model catalyst [61, 62]. The close relation between the geometric structure of α-V_2O_5 and γ-V_2O_5 as well as the possible conversion between the two structures is of high interest in view of catalysis. As the oxidation of hydrocarbons on vanadium oxide catalysts involves a Mars-van Krevelen redox cycle, differences in the redox properties and reducibility of α-V_2O_5 and γ-V_2O_5 are related to the performance of these phases as catalysts.

γ-V_2O_5 is also interesting in view of a very promising application of V_2O_5 nanofiber sheets as actuators as reported by Gang Gu *et al.* [63] and also for the synthesis of 1-dimensional anisotropic $VO-x$ nanotubes and nanorods for future nanotechnology [64, 65]. The catalytic relevance of the V^{5+} oxidation state combined with the structural peculiarities of the synthesized particles and the close relation to the α-V_2O_5 phase motivates the investigation of the electronic structure of γ-V_2O_5.

4.1.1 Geometric Structure

The γ-V_2O_5 forms a layer-type orthorhombic lattice with constants *a* = 9.946(0) Å, *b* = 3.585(0) Å and *c* = 10.042(0) Å [59]. The structure is set up by layers of edge and corner sharing VO_5 pyramids sticking out at both sides of the layer. As opposed to α-V_2O_5, where all V=O vanadyl bonds are oriented along *c* (*z* direction), the double chains of edge sharing pyramids are tilted relatively to each other in γ-V_2O_5 with an angle between the basal plane of the pyramids and the *x* axis of about +30 ° and -30 °, respectively (Fig. 1). Additionally, the VO_5 pyramids are oriented along *x* as down-up-down-up while in α-V_2O_5 the orientation is down-down-up-up. As a consequence, there exist two structurally different VO_5 pyramids. The first one at the V1 site can also be thought of as a bi-pyramidal (VO_6) by including the weak interlayer bond to the vanadyl oxygen of the adjacent layer. The second VO_5 pyramid at the V2 site is oriented in such a way that no oxygen atom lies in close vicinity of the basal plane. The existence of the two different vanadium sites has been confirmed by FTIR measurements of γ-V_2O_5 nanorods [62]. Each of the two pyramids contains three structurally different oxygens, but in total, due to the linking via one common oxygen, there exist five different oxygens and two different vanadiums in γ-V_2O_5. The primitive cell comprises four formula units. It is worthwhile to mention here that γ-V_2O_5 undergoes a transformation into the normal form of α-V_2O_5 near 340 °C [59].

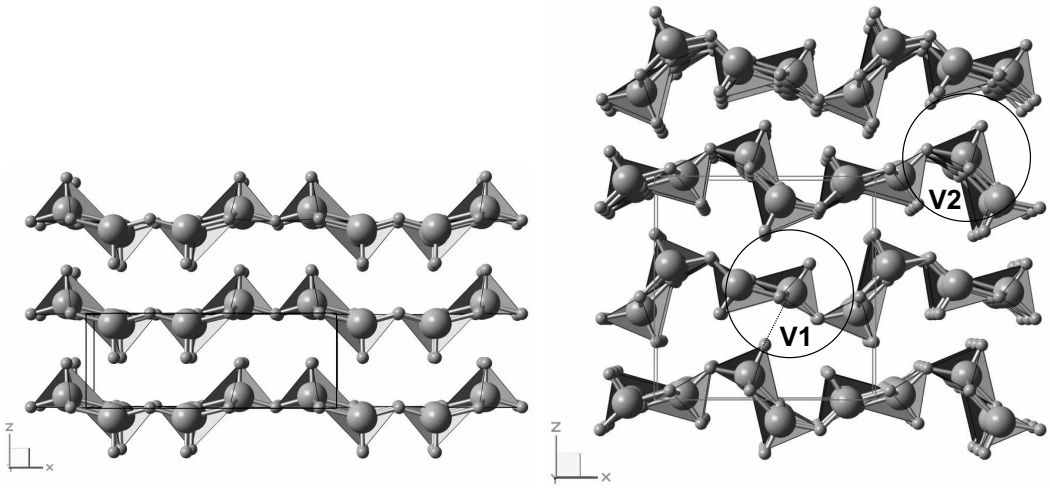

Fig. 4.1: Crystal structure of α-V_2O_5 and γ-V_2O_5. The orthorhombic unit cells are indicated; a, b and c are parallel to x, y and z, respectively. Circles labeled V1 and V2 highlight the two differently surrounded vanadium sites existing in γ-V_2O_5. Images created with [66].

The basic structural units in γ-V_2O_5 and α-V_2O_5 are distorted VO_5 pyramids (see Fig. 4.2).

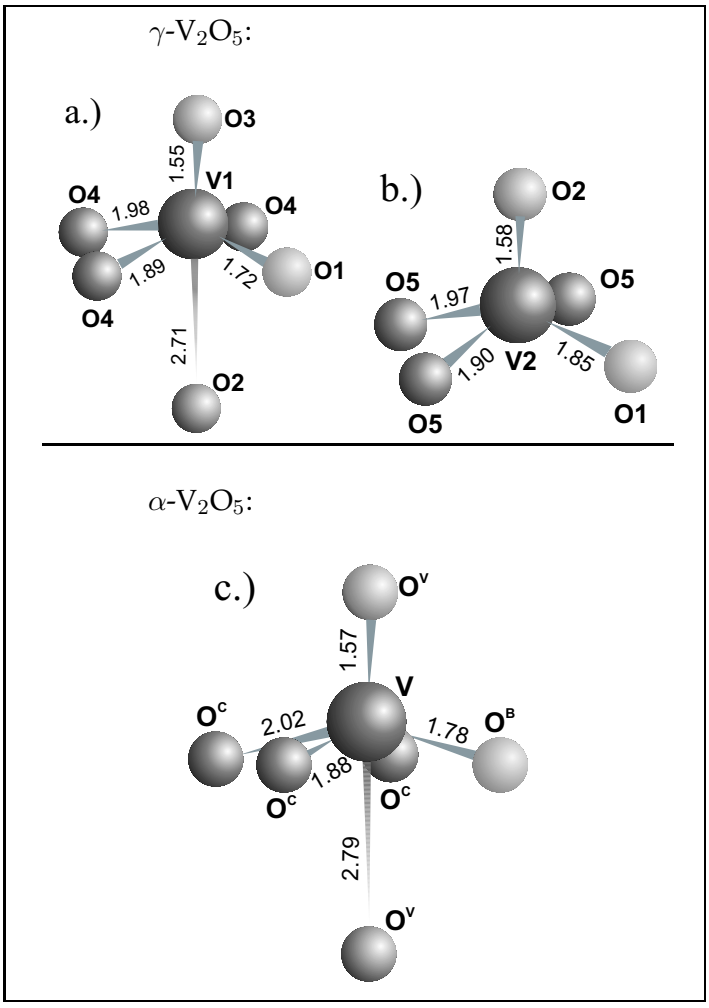

Fig. 4.2: Local surrounding at the different vanadium sites in γ-V_2O_5 (V1 (a) and V2 (b)) and in α-V_2O_5 (c). The oxygen atoms are labeled as: O3, O2, O^V: vanadyl oxygen; O4, O5, O^C: chain oxygen; O1 and O^B: bridge oxygen.

These pyramids have similar features: one short bond to the vanadyl oxygen, one bond to a bridging oxygen linking two pyramids at a pyramid corner, and three bonds to chain oxygens, of which two have the same bonding distance to the vanadium center.

However, the interatomic distances are different and from the dispersion of the V-O bonding distances in the pyramid base follows that the distortion at the V1 site is bigger than in the case of α-V_2O_5. At the V2 site, on the other hand, the distortion is less than in α-V_2O_5. The bonding distances in γ-V_2O_5 and α-V_2O_5 are compared against each other in Fig. 4.1.1.

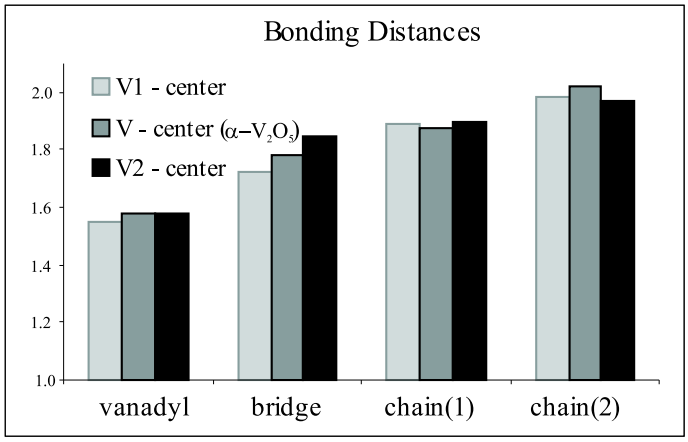

Fig. 4.3: Comparison of the bonding length at the different V-sites.

The distance from the vanadium center to a vanadyl oxygen from the adjacent plane measures 2.793 Å for α-V_2O_5 and 2.714 Å at the V1 site in γ-V_2O_5. Taking the weak interlayer bond into account results in a 6-fold coordinated vanadium.

4.1.2 Band structure and density of states

Calculation

For γ-V_2O_5 56 k-points in the irreducible part of the Brillouin zone and a plane wave cut-off R_{kmax} of 7.5 (corresponding to an energy cut-off of 28.7 Ry or 390.5 eV, respectively) was used. α-V_2O_5 was calculated with 84 k-points and a plane-wave cut off of 8 (31 Ry). In order to get a good basis set for the projection of the DOS onto p and d states in the simulation, the local coordinates at each atom of the tilted VO_5 pyramids were chosen such that the z-axis coincides with the direction of the V=O(vanadyl) bond.

In Fig. 4.4 the band structure calculated along selected high symmetry lines within the first Brillouin zone corresponding to the primitive orthorhombic lattice (see Fig.4.4) is presented. Along the direction Γ-X (i.e. parallel to the x axis) the dispersion of the bands is small and the electrons are well localized, while along the Γ-Y direction (i.e. parallel to the y axis) the dispersion measures about 0.5 eV. The y axis corresponds to the direction of the double chains (edge sharing VO_5 pyramids), along which the electrons can move more easily than along the x direction, where the bridging oxygens form connections between the double chains (corner sharing pyramids). Along the direction Γ-Z the dispersion is also weak, reflecting the localization of the electrons in the layered structure. In the conduction band the dispersion of the bands along Γ-X and Γ-Z starts to increase at about 5 eV above the Fermi level, whereas the density of the bands decreases. A remarkable feature in the band structure plot is the split-off conduction band at around 2 eV.

Insight into the chemical and physical properties is gained by observing the vanadium d states and their hybridization with the ligand p orbitals. The oxygen $2p$ and vanadium $3d$ density of states (Fig. 4.5) of γ-V_2O_5 and α-V_2O_5 attest the close relation between the structure of the two compounds since the DOS of γ-V_2O_5 exhibits features very similar to the one of α-V_2O_5 (Fig. 4.5). Both compounds are semiconductors: after a band gap of only 1.70 eV (1.75 eV in α-V_2O_5) a narrow split-off conduction band of 0.6 eV width is separated by another gap of 0.7 eV from the main conduction band. Shape and width of the split-off conduction band are nearly identical for the two polymorph and the separation to the main conduction band is only around 0.1 eV larger in the gamma phase. Similar to α-V_2O_5, the valence band of γ-V_2O_5 consists mainly of oxygen $2p$ states with only a small contribution from vanadium $3d$ states, whereas the conduction band mainly comprises the unoccupied vanadium $3d$ states. Common features in the oxygen and vanadium DOS are observed for both compounds and reflect a substantial degree of hybridization between oxygen $2p$ and vanadium $3d$ states. This hybridization has extensively been discussed by Eyert *et al.* [57] for the case of α-V_2O_5.

In the following, differences in the VO_5 building blocks will be considered in the discussion of the DOS.

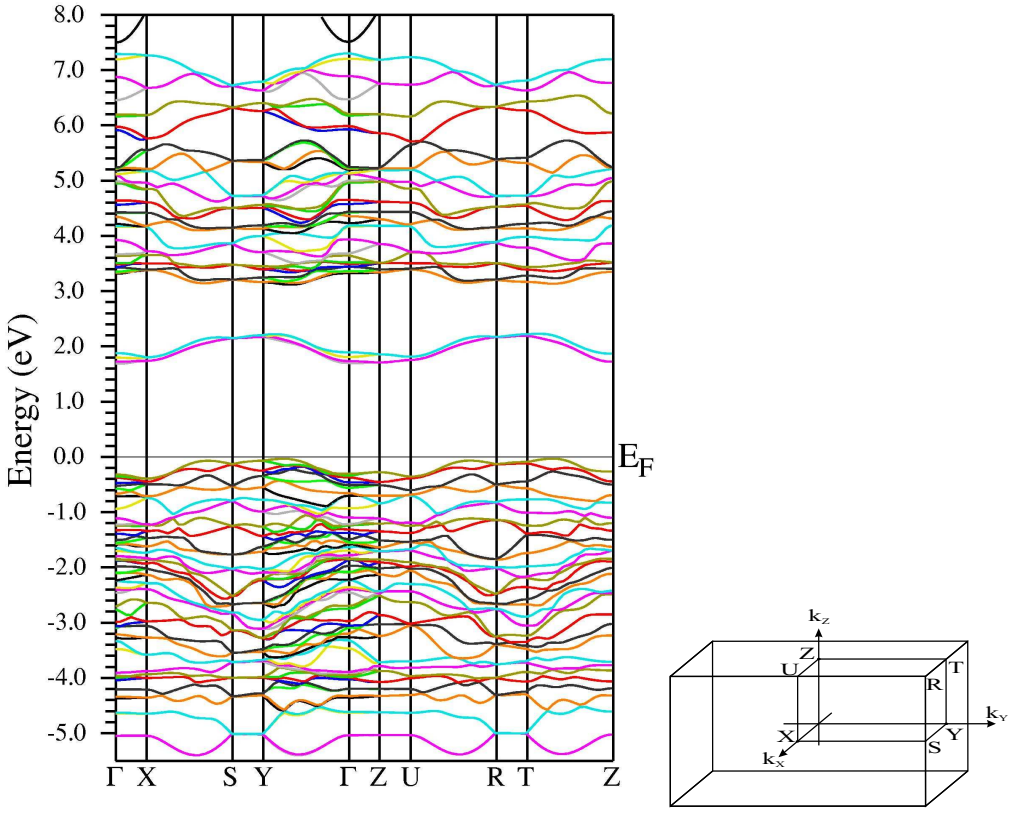

Fig. 4.4: Band structure of γ-V_2O_5 along symmetry lines within the first Brillouin zone of the simple orthorhombic lattice. Energies are given relative to the Fermi level. The corresponding Brillouin zone and the path along which the band structure was calculated is shown on the right.

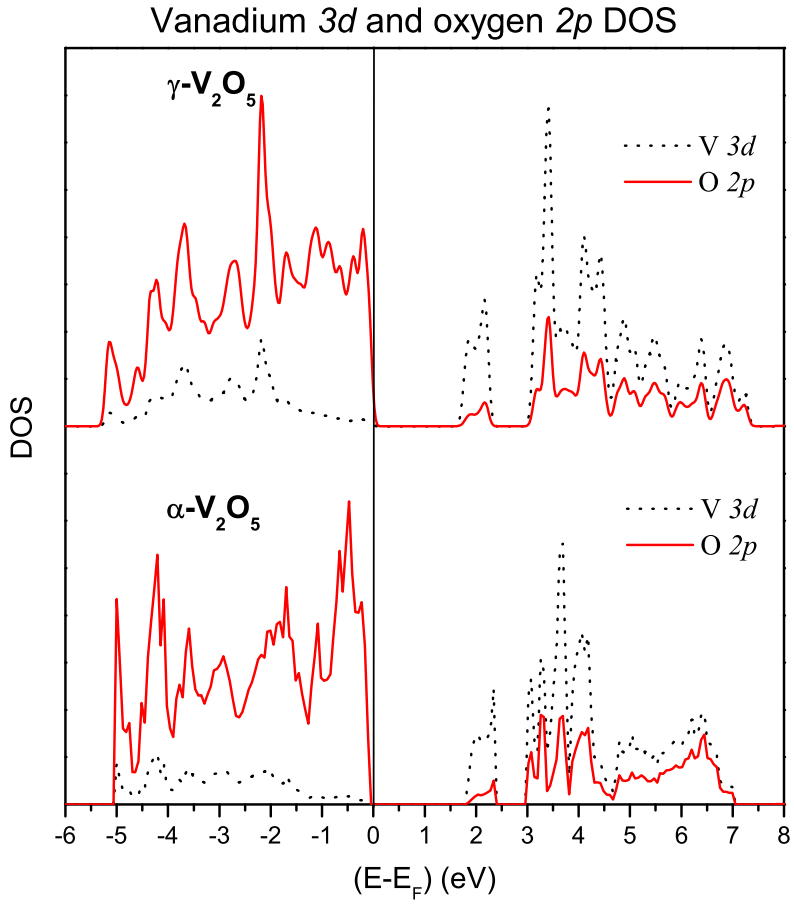

Fig. 4.5: V $3d$ and O $2p$ projected density of states of α-V_2O_5 and γ-V_2O_5.

Comparison of the different $\mathbf{VO_5}$ units in γ-$\mathbf{V_2O_5}$ and α-$\mathbf{V_2O_5}$

A characteristic of the γ-V_2O_5 structure is the existence of two different sites for the vanadium atoms.

The crystal field splitting is determined by the geometry of the surrounding oxygen atoms and leads to a separation of the lower part of the conduction band. States forming π^* antibonds appear at lower energy whereas σ^* antibonds are formed at higher energy. The two subgroups of the unoccupied orbitals are separated by a ligand field splitting. The angular momentum projected DOS (PDOS) are presented in the Figures 4.6 and 4.7 for the two vanadium sites and their oxygen ligands.

Due to the choice of the local coordinate system at each atom of the tilted pyramids, the $3d$ DOS is projected onto the different orbitals such that the vanadium $3d_{z^2-r^2}$ orbitals point towards the vanadyl oxygen and the $3d_{x^2-y^2}$ orbitals point in the direction of the three chain oxygens and the bridging oxygen. Consequently these two orbitals form σ^* antibonding combinations with the oxygen $2p$ orbitals and appear in the upper region of the lower conduction band. At the V1 site the $3d_{z^2-r^2}$ orbital provides a narrow contribution to the DOS between 6 and 7.5 eV which is identically mirrored by the vanadyl oxygen $2p_z$ orbital. The same agreement in the DOS of the $3d_{z^2-r^2}$ orbital and the vanadyl oxygen $2p_z$ orbital of the V2 site is observed in the energy range between about 4.5 to 6.5 eV. Due to the fact that the vanadium atoms are not in plane with the chain and bridge oxygens, the contribution of the $3d_{x^2-y^2}$ orbitals reaches into the π^* region. At lower energies, the vanadium $3d_{xz}$ and $3d_{yz}$ orbitals mainly combine with the vanadyl oxygen $2p_x$ and $2p_y$ orbitals by forming π^* states. Consequently, the features between around 2 and 7 eV at the V1 and between around 2 and 6 eV at the V2 center are reproduced by the respective vanadyl oxygen $2p_x$ and $2p_y$ orbitals. The remaining vanadium $3d_{xy}$ orbital lies lowest in energy and stretches in between the chain and the bridge oxygens, forming π^* combinations. At the V1 site, it forms a strong and very localized combination with the bridging O1 $2p_y$ orbital between 3 and 4 eV. Although the distance between the bridging oxygen and the V2 center is only slightly larger, the degree of hybridization between the V2 $3d_{xy}$ and the O1 $2p_y$ orbital is much smaller. Instead the V2 $3d_{xy}$ orbital provides the main contribution to the split-off conduction band by forming π^* combinations mainly with the chain oxygen (O5) $2p_x$, $2p_y$ and the bridge (O1) $2p_y$ orbital. In fact it is an interesting consequence of the different geometry of the V1 and V2 pyramids that the intensity of the two features in the respective $3d_{xy}$ DOS is reverse. For the V1 site (Fig. 4.6) and in the α phase [57], where the vanadium atom is formally sixfold coordinated in a distorted

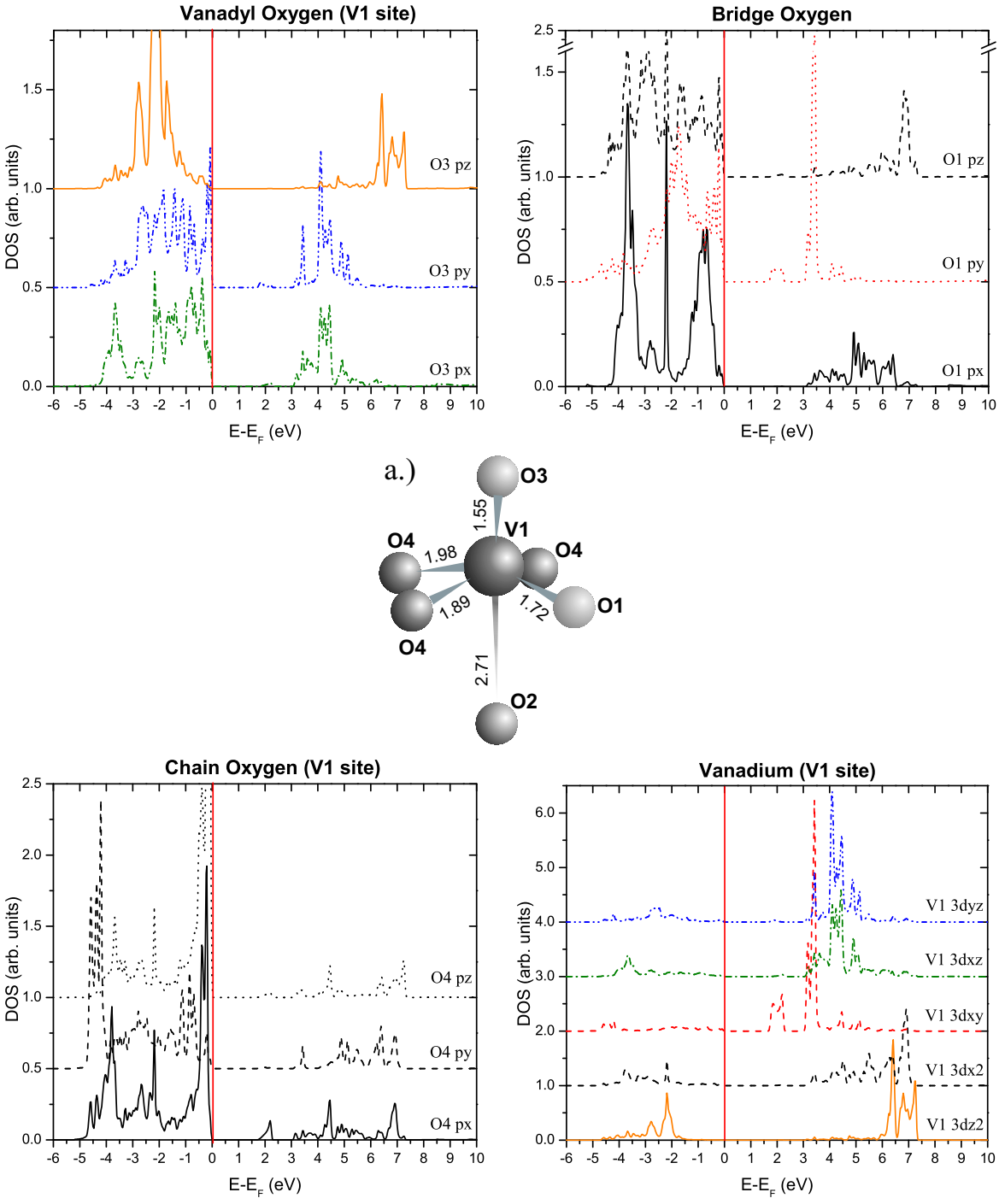

Fig. 4.6: Angular momentum projected DOS at the V1 site. In order to point out similarities in the atom projected contributions of oxygen and vanadium above the Fermi level, similar colors have been used for the most prominent overlapping contributions.

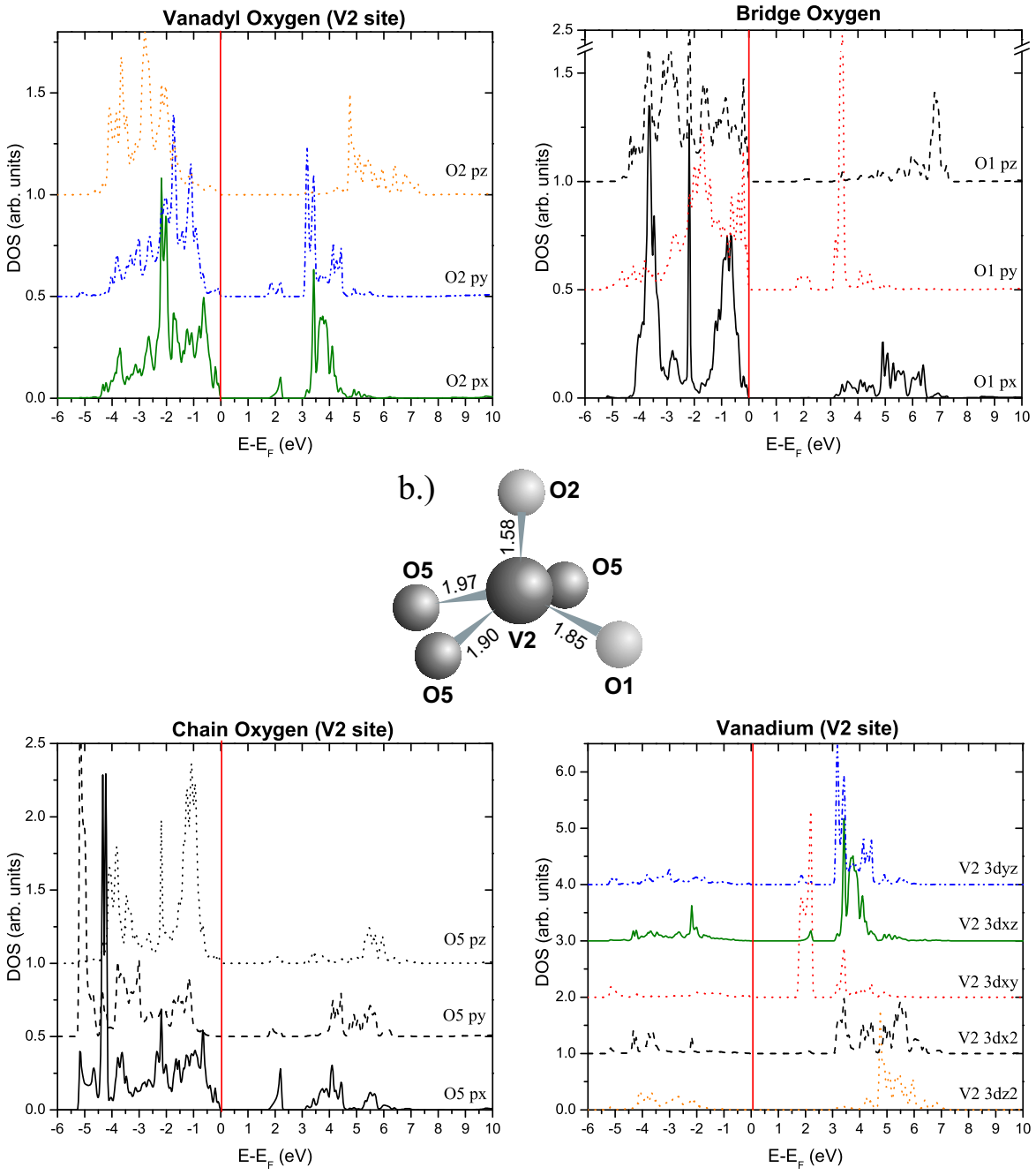

Fig. 4.7: Angular momentum projected DOS at the V2 site. In order to point out the interaction of oxygen and vanadium states in the region above the Fermi level of the atom projected DOS, similar colors have been used for the most prominent overlapping contributions.

octahedron, the crystal field splitting is well developed and clearly separates in energy π^* from σ^* forming states. The splitting is best represented in the DOS of the vanadyl oxygen (O3) $2p$ orbitals which form clear π^* and σ^* states. It measures around 2.6 eV (estimated form the separation of the center of mass of the unoccupied O3 $2p$ states). At the fivefold coordinated V2 site the difference between the longest and the shortest V-O distance is smaller and the resulting pyramid is less distorted. This is reflected in the $2p$ projected DOS of the vanadyl oxygen (O2) at the V2 site where the π^* and σ^* forming states lie closer in energy and the separation of the center of mass measures only around 1.8 eV (see Fig. 4.7).
Interlayer coupling leads to similarities in the V1 and O2 PDOS. A comparison reveals only a slight agreement in the O2 $2p_z$ and V1 $3d_{z^2-r^2}$ PDOS at around 7 eV above the Fermi level. The existence of a small hybridization comes apparent from a comparison of the width of the O3 and O2 $2p_z$ PDOS: the broadening of the latter is caused by interaction with the V1 $3d_{z^2-r^2}$ orbital. Nevertheless, the agreement is small and underlines the fact that the interlayer bonding is weak and that the picture of the five fold coordinated pyramid is more accurate than the octahedral description. In α-V_2O_5 there exists only one kind of vanadyl oxygen and therefore it is not possible to separate out information from the PDOS about the orbital overlap between the layers. Nevertheless, single layer SLAB calculations of Chakrabarti *et al.* [56] demonstrate a weak electronic interlayer coupling also in α-V_2O_5. The role of the vanadyl oxygen from the adjacent layer can therefore be neglected and the stronger crystal field splitting at the V1 results from the higher distortion of the VO_5 pyramid.

ELNES: simulation and experiment

Electron energy loss spectrometry (EELS) is applied to probe the local electronic structure and the oxidation state of vanadium in γ-V_2O_5.

The shape of the vanadium and oxygen edges is strongly related to the oxidation state of the vanadium and to the distortion of the coordination polyhedron [67]. In particular, the vanadium white line ratio reacts very sensitively on the oxidation state and the distortion of the VO_6 polyhedron [68, 69]. In α-V_2O_5, the VL_{II} edge is more intense than the VL_{III} edge [67] (Fig. 4.8 bottom), whereas, with decreasing oxidation state, the VL_{II} intensity decreases relative to the L_{III} spectral weight. This fingerprint allows a reliable assignment of the oxidation state of the vanadium. For this reason also the vanadium

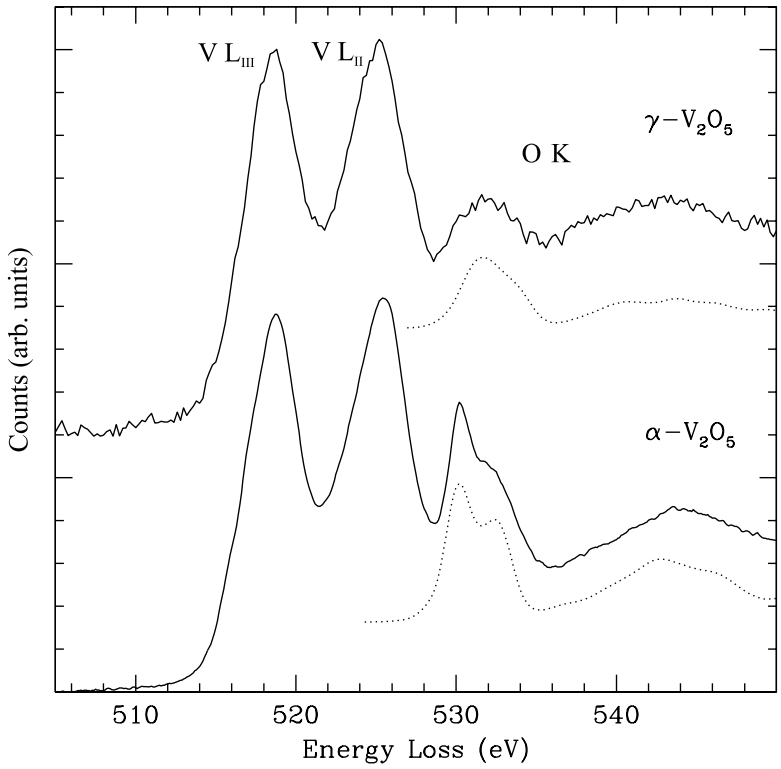

Fig. 4.8: EELS spectra recorded from α-V_2O_5 (bottom) and γ-V_2O_5 nanorods (top) showing the vanadium $2p$ and the oxygen $1s$ ionization edges. The calculated oxygen edges are printed in dotted lines.

white lines are presented, although the following discussion as well as the simulation is based on the OK edge. The focus on the OK edge is justified by the fact that within a one-electron approximation the simulation of the $2p$ to $3d$ transition giving rise to the L edge fails due to strong electron correlation effects [70]. In α-V_2O_5, the OK edge is characterized by a fine structure (Fig. 4.8) at around 530 eV exhibiting two contributions arising from transitions from an O 1s state to a final $2p$ state in π^* or in σ^* hybridization with a vanadium $3d$ state. *Ab initio* band structure calculations combined with the simulation of spectra with the TELNES program support the interpretation of the near edge fine structure in EELS and allow to directly assign features to the corresponding transitions.

Figure 4.8 demonstrates the close agreement between simulation and experiment, although the core hole left by the excited electron and the high energy tail of the preceding VL_{II} edge where not taken into account in the simulation.
In the spectra of γ-V_2O_5, the vanadium VL_{II} peak is more intense than the VL_{III} in correspondence with an oxidation state of +5 of vanadium in case binary vanadium oxides [67]. Slight differences in the shape of the white lines of the two polymorph are related to differences in the crystal field splitting. Additionally, some artifacts are observed in the case of γ-V_2O_5 due to the low counting rate and the low signal to noise ratio in the EELS spectra. The shape of the OK feature centered at 531.6 eV is quite different to the one observed for α-V_2O_5 and consists of a single asymmetric peak centered at around 532 eV and a broad peak at around 544 eV. The calculations for γ-V_2O_5 (dotted line in Fig. 4.8) agree very well with the experimental data. The close agreement with the bulk simulation also confirms the weak interlayer interaction as the size and surface effects of the γ-V_2O_5 nanorods have negligible effect on the ELNES. Simulation and experiment show that the fine structure visible in the OK edge of α-V_2O_5 has vanished. An explanation follows from a closer observation of the two different vanadium surroundings present in γ-V_2O_5. Five differently coordinated oxygen atoms contribute to the spectrum and the total OK spectral weight is the sum of these contributions, of which each has its individual shape. As a result the π^* and σ^* components overlap and are no longer distinguishable in the total OK edge. In Fig. 4.9 the single contributions of the different oxygens to the ELNES are presented. When the contributions of the corresponding oxygens surrounding the V1 and V2 centers are added up, the representative ELNES of the two pyramids are obtained (Fig. 4.9 bottom). Knowing that the interlayer bond is very weak and can be neglected in this respect, one ends up comparing three differently distorted VO_5 pyramids (at the V1 and V2 site and in the α phase). The separation between

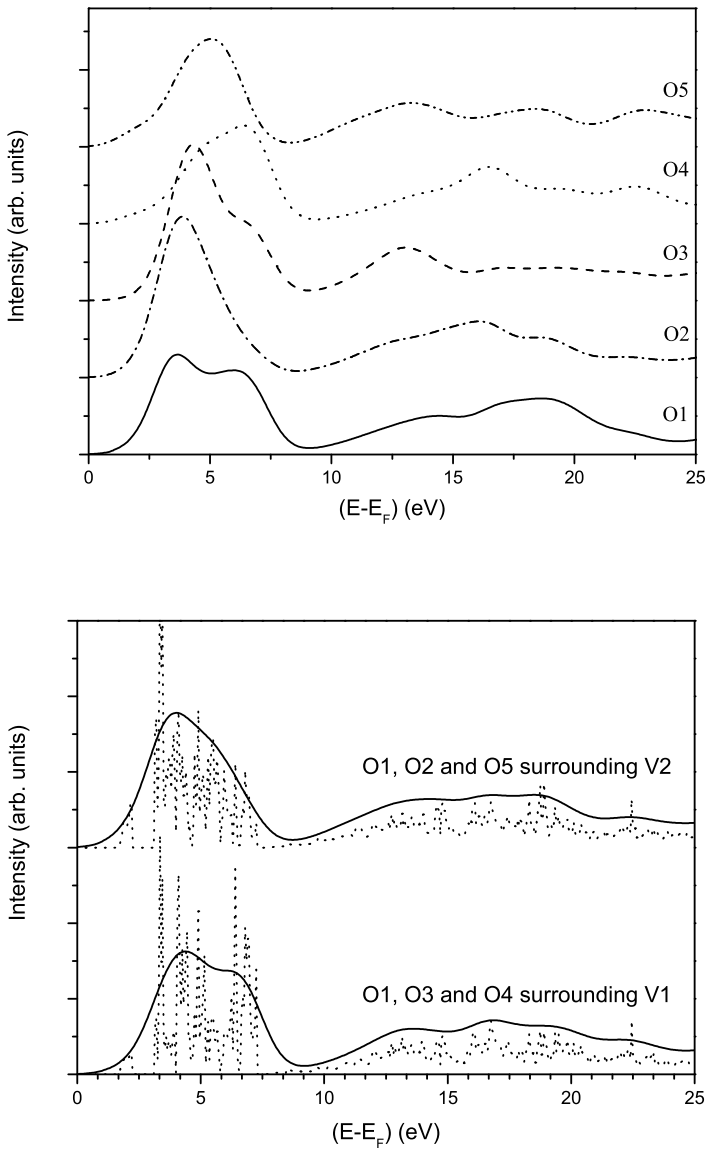

Fig. 4.9: Single contributions of the different oxygens to the OK ELNES (top) and sum over oxygen contributions arising from VO_5 pyramids at the V1 and V2 site of γ-V_2O_5 (with and without experimental broadening) (bottom).

the π^* and σ^* states are visible in the calculated ELNES of the V1 pyramid whereas this separation is no more observable at the V2 site. This underlines the similarity between the VO_5 pyramid at the V1 site and the pyramid of the α phase (see Fig. 4.8).

4.1.3 Discussion

The theoretical investigation of the band structure and density of states of different VO_5 building blocks in γ-V_2O_5 and α-V_2O_5 gives insight into the relation between geometric and electronic structure. The general distribution of features like the split-off conduction band and the width of band gaps in the oxygen and vanadium DOS of the two compounds attest the close agreement between the two structures. However, the angular-momentum projected DOS reveals a splitting of the vanadium d states into π^* and σ^* forming states which is very sensitive to the geometry of the O ligands. At the V1 site, where the distortion of the VO_5 pyramid, measured from the dispersion of the bonding distances is largest, the splitting is well pronounced. At the V2 site the distortion is smaller and the π^* and σ^* regions show a slight overlap. The splitting at each site is best reproduced by the respective vanadyl oxygen $2p$ orbitals. A detailed investigation of the angular-momentum projected DOS reveals that the distribution of intensities in the DOS acts very sensitively on small changes in the bonding distance and geometry. The determined difference in electronic structure of the two polymorph results from their different geometric structure. Differences in the electronic structure combined with a fixed chemical composition allows, in a further step, to elucidate a correlation between the DOS and relevant chemical properties, such as catalytic performance. From this information one can then draw back conclusions about electronic properties relevant for a specific catalytic process.

From a comparison of similar features in the DOS of V1 and the vanadyl oxygen of the adjacent layer (O2) it could be concluded that the interlayer coupling is indeed very weak and that the picture of a distorted pyramidal surrounding has to be favored with respect to a distorted octahedral description. The close agreement between simulated and measured OK ELNES supports the interpretation of the changing in the fine structure of the OK edge between the α and γ phase. With respect to the catalytic potential of α-V_2O_5 it is of relevance to have now two polymorph of the same chemical composition with known differences in the electronic properties available. They allow, in a further step, to probe the concept of structure-activity correlation in a rigorous manner.

Chapter 5

Vanadium (V) phosphorous oxide Phases

This chapter deals with the electronic and geometric structure of the most prominent vanadium (V^{5+}) phosphorus oxide phases. After a brief overview on the different existing phases, the electronic and geometric structure of β, α_{II} and α_I will be discussed.

5.1 Overview of (V^{5+}) $VOPO_4$ phases

Depending on the synthesis conditions, $VOPO_4$ crystallizes under numerous forms and several different polymorph of $VOPO_4$ have been reported in the literature: α_I-$VOPO_4$, α_{II}-$VOPO_4$, β-$VOPO_4$, γ-$VOPO_4$, δ-$VOPO_4$, ϵ-$VOPO_4$ and ω-$VOPO_4$. To date, no full structural determination (i.e., a full space group analysis with definite atomic coordinates) was performed and published for α_I-, γ-, δ-, ϵ- and ω-$VOPO_4$. The reason for the unresolved structures lies in the fact that (i) these systems are prone to very strong texture effects due to their platelike nature, (ii) their rapid hydration effects in ambient atmospheric conditions and, the most complicating factor, (iii), that the slight differences between the synthesis conditions often lead to mixtures, notably for α_I-, α_{II}-, γ-, and δ-VOPO4.

Therefore, structural models have been proposed which take into account the conditions due to stoichiometry and possible geometrical arrangement of VO_6 octahedra and PO_4 tetrahedra. Some authors assume that α_I-$VOPO_4$ is isotypic with $VOSO_4$ [71]. Bordes *et al.* [72] proposed a structure for γ-$VOPO_4$ based on the structure of $VOAsO_4$. In this

model, pairs of distorted VO_6 octahedra share one edge and their unicoordinated V=O bonds appear in trans position whereas all the other oxygens are shared with a PO_4 tetrahedron, either belonging to the same or the next sheet. Another structural proposal for γ-$VOPO_4$ was given by Ben Abdelouahab *et al.* [33] in which the structure is an intermediate form between those of α_I and α_{II}, with all V=O bonds parallel and pointing half inside, half outside the layers. A possible structure for δ-$VOPO_4$ was also proposed by the same group from its behavior during hydration experiments and is supposed to have slightly more complex structure, with lines of adjacent octahedra with their V=O short bonds directed upwards alternating with lines in which they are directed downwards, regardless of belonging to the bottom or the upper sublayer [73]. ϵ-$VOPO_4$ is thought to have some structural relation with β-$VOPO_4$ [74]. In the case of ω-$VOPO_4$, a possible metastable structure which still contains some contradictions has been published [11].

Phase transitions between the V^{5+} VPO phases

During thermal treatment at high temperature the consecutive transitions $\alpha_I \rightarrow \alpha_{II} \rightarrow \beta$-$VOPO_4$ or $\delta \rightarrow \gamma \rightarrow \beta$-$VOPO_4$ have been observed [1]. β-$VOPO_4$ is considered to be the most stable phase among anhydrous orthophosphates. Schrader et al. [75, 76] observed the conversion of β-$VOPO_4$ to $(VO)_2P_2O_7$ at 500 °C in 2% n-butane/air. In this reduction process single V06 octahedra form pairs by loss of oxide anions. $(VO)_2P_2O_7$ can also be oxidized to β-$VOPO_4$ by means of O_2 [77].

5.2 $\beta-$**VOPO**$_4$

This section is focused on the characterization of β-$VOPO_4$ by a combination of theoretical and experimental methods. *Ab initio* band structure calculations based on density functional theory (DFT) were performed in order to evaluate the bulk electronic structure. Core level spectroscopic methods were applied to experimentally probe the electronic structure at the ionized species: electron energy loss spectrometry, EELS, at the oxygen K-edge and near edge X-ray absorption spectroscopy, NEXAFS, at the V K-edge. The gained spectra are interpreted by means of the calculated band structure and compared to simulated spectra.

5.2.1 Geometric Structure

The β-$VOPO_4$ phase crystallizes in the orthorhombic space group D_{2h}^{16} Pnma. Its crystal structure was first determined in 1972 by Gopal *et al.* [78] and is isostructural with that of β-VSO_5. It consists of PO_4 tetrahedra and irregular VO_6 double pyramids which are linked along the *a* (x) direction by sharing a common apex. Rows of double pyramids form a zig-zag like chain in which the pyramid axis are alternately tilted by $\pm$ 20.8 $^\circ$ toward the *c* (z) direction (see Fig. 5.1). Within a double pyramid, the vanadium atom is shifted from the center of the square plane toward the vanadyl oxygen (see Fig. 5.2). The singly coordinated vanadyl oxygen (O4) defines the pyramid axes by a short V=O double bond of 1.57 Å and an additional, faint interaction with the vanadium atom of the next pyramid at a distance of 2.59 Å. Three structurally different oxygens (O1 - O3) define the four equatorial corners of the double pyramid: O1 defines the two corners in the *y*-direction, O2 and O3 define the corners in *x* direction. The resulting distorted geometry of the pyramids is typical for vanadium in an oxidation state of *V* or *IV* [79]. Chains of VO_6 units are separated from each other by PO_4 tetrahedra which are linked to the oxygens of the equatorial plane. Each PO_4 tetrahedra spans the space between three neighboring chains of double pyramids by sharing two corners (O2, O3) with two subsequent double pyramids of one chain and two corners (2xO1) with the adjacent chains in +y and -y direction, respectively. The primitive cell comprises four formula units.

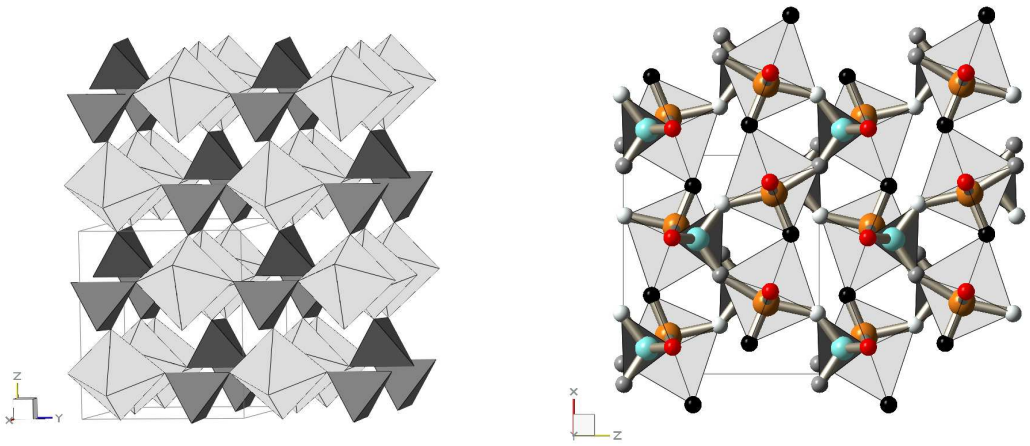

Fig. 5.1: Crystal structure of β-$VOPO_4$, viewed from [100] direction in (a) and from [010] direction (b). The orthorhombic unit cells are indicated; a, b and c are parallel to x, y and z axis, respectively. Four structurally different oxygens are present: vanadyl oxygen (O4, black) is bond only to vanadium, bridging oxygens (O1, red, O2, white and O3, gray) are shared between vanadium and phosphorus. For clarity, groups of atoms are combined to VO_6 octahedra and PO_4 tetrahedra.

5.2.2 Synthesis and characterization

Due to the easy transformation between the different $VOPO_4$ polymorph and the close agreement in their synthesis procedure, the preparation has to be done very carefully. β-$VOPO_4$ was synthesized by oxydehydration of $VOHPO_4{\cdot}0.5H_2O$ at 680 °C for 4 h under dry oxygen. In order to check the phase purity of the synthesized product, a combination of characterization methods were applied: scanning electron microscopy (SEM) and energy dispersive X-ray detection (EDX) to investigate the morphology and the atomic ratio, respectively; X-ray diffraction (XRD) for phase analysis and high resolution transmission electron microscopy (HRTEM) for micro structural analysis.

The SEM investigation reveals that β-$VOPO_4$ is composed of irregular shaped particles of a size varying from 0.5 μm to 2 μm (see Fig. 5.3). The measured atomic ratios are consistent with the stoichiometry of β-$VOPO_4$. XRD measurements obtained using Cu K_α radiation in the angular range (2θ) of 15° to 75° show a good agreement with the simulated (PowderCell software [80]) X-ray diffraction diagram in both positions and intensities of the peaks (see Fig 5.4). No unassigned peaks are visible in the recorded angular range. Due to the likely existence of small portions of phases which are below

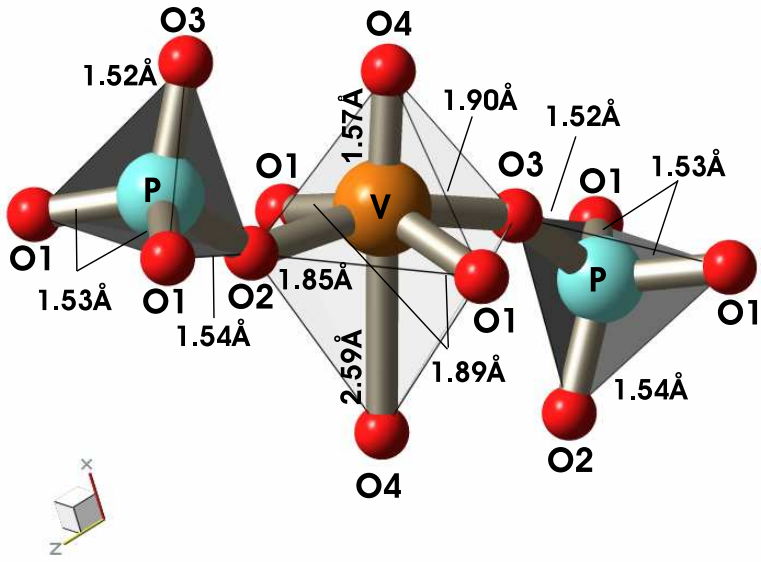

Fig. 5.2: Arrangement and bonding distances of the different oxygens in β-VOPO$_4$ The simulations of β-VOPO$_4$ are based on the experimentally derived structure taken from the literature [78].

the detection limit of XRD it can only be stated that the synthesized product is at least 'XRD-pure'. Changes during the recording process due to X-ray irradiation could not be observed. The crystallinity of β-$VOPO_4$ is observed in lattice fringes images obtained by HRTEM as shown in Fig 5.5. However, amorphous parts were observed to appear during high dose electron irradiation.

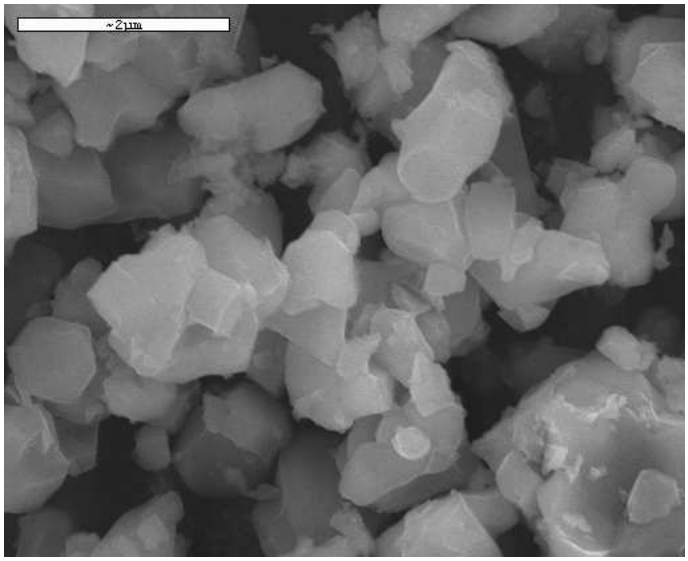

Fig. 5.3: SEM image showing irregular shaped particles of β-$VOPO_4$.

5.2.3 Band structure calculations and EELS, NEXAFS - experiments

Due to the high stability of the β-phase with respect to the other $VOPO_4$ phases, its structure can be determined by a combination of XRD and Riedfeld refinement. The calculations are based on the unit cell parameters provided by [78].

The calculation was performed with 80 k-points in the irreducible part of the Brillouin zone and a plane wave cut-off parameter R_{kmax} of 7.0 (corresponding to an energy cut-off of 28.7 Ry). The values of muffin-tin sphere radii were taken equal to 1.45 Bohr for V and P and 1.3 Bohr for O, respectively. In order to get a good basis set for the projection of the DOS onto p and d states in the simulation, the local coordinates at each atom of the tilted VO_5 pyramids were chosen such that the z axis coincides with the direction of the V=O vanadyl bond. This choice also determines the orientation of the local coordinates at the PO_4 tetrahedra except for the one oxygen that is shared with a VO_5 pyramid of different orientation.

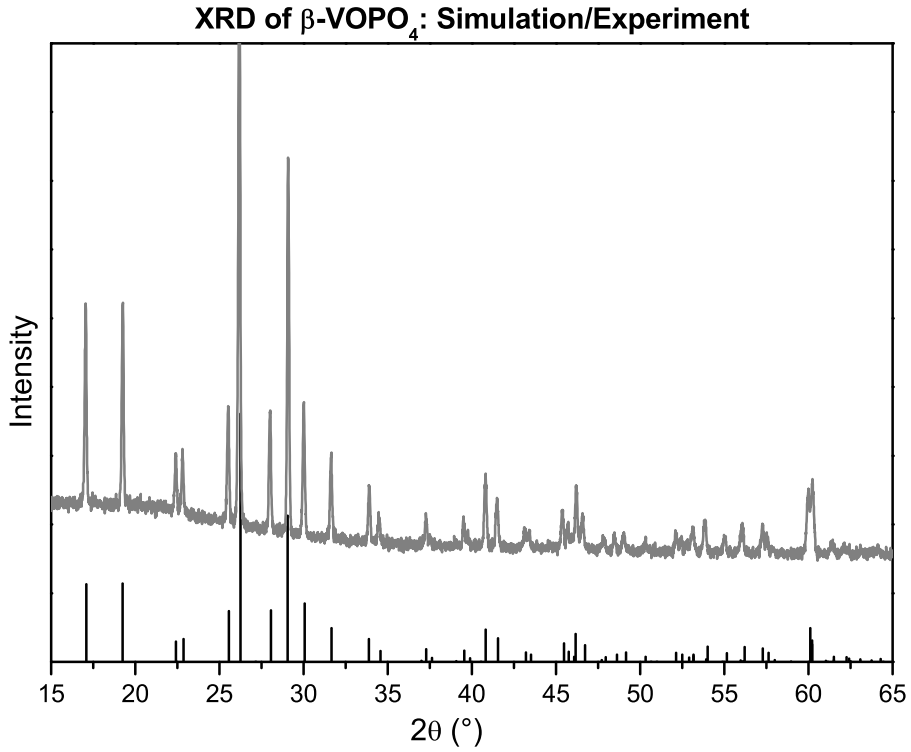

Fig. 5.4: XRD of β-VOPO$_4$. Calculated and experimental XRD spectra present a good agreement in both peak positions and intensities.

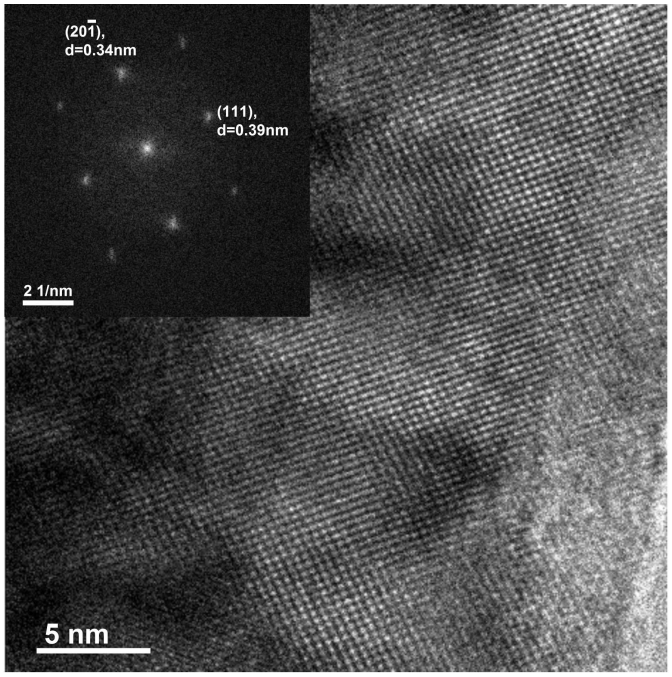

Fig. 5.5: HRTEM image of β-$VOPO_4$ in the [132] zone axis. The inset shows the two dimensional FFT and indicates the corresponding planes. The image contains contrast variations due to defects and variations in the thickness of the sample.

5.2.4 Results and Discussion

Electron density

Figure 5.6 shows the electron density within a plane perpendicular to the b axis, chosen to intersect with vanadium centers and the bonds formed to bridging oxygens (V-O-P) and vanadyl oxygens (V=O). From the electron density distribution one can conclude that the bonds between vanadium centers and vanadyl oxygen exhibit more covalent than ionic bonding character, whereas in the case of bonds to bridging oxygens the situation is reversed. The electron density also reveals the reason for the characteristic difference between β-VOPO$_4$ and the layer structures of α_I-, α_{II}-, γ-, δ- and ϵ-VOPO$_4$: In case of β-VOPO$_4$, the weak interaction between the vanadium center and the vanadyl oxygen belonging to the neighboring vanadium center (at a distance of 2.59 Å) is "bridged" by the strong covalent bonded PO$_4$ units. They form a three-dimensional network by linking two oxygens of two subsequent VO$_5$ pyramids.

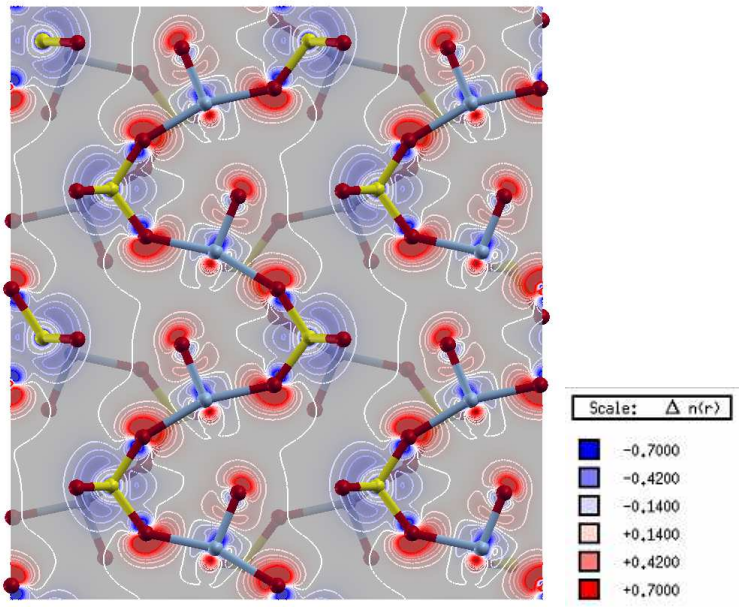

Fig. 5.6: Difference density plot of β-VOPO$_4$ showing the difference between converged crystalline electron density and the superposition of the atomic sites. The difference density is given for a plane perpendicular to the b axis, passing through V-O-P and V=O bonds. Oxygen atoms are plotted in red, phosphorus atoms in yellow and vanadium atoms in blue.

Density of states

Total DOS

The total DOS and the contributions of vanadium, oxygen and phosphorus to the DOS in an energy region between -10 and 20 eV around the Fermi-level are presented in Fig. 5.7. Below the Fermi-level the DOS consists of three blocks of bands. From a comparison of the different contributions follows that these bands mainly comprise oxygen states that are mixed with phosphorus states in the lower two sets of bands between -9 and -5 eV and with vanadium states in the energy range between -4.5 eV and the Fermi-level.

Above the Fermi-level the DOS is dominated by vanadium states with only a small contribution from oxygen states in the lower conduction band between around 1.5 and 6 eV and by a combination of phosphorus and oxygen states in the upper conduction band above 8 eV.

Projected DOS

A deeper insight into the bonding relations and the hybridization of states is obtained form the angular momentum projected DOS at the vanadium, phosphorous and oxygen sites, which are presented in the Figures 5.8 - 5.10. An inspection of the lower lying valence states reveals that bonding phosphorus s states are concentrated in the region between -9 and -7.5 eV followed by states of p character between -6.5 and -5 eV. Both form strong covalent σ bonds with $2p$ states from the surrounding oxygen atoms (O1, O2 and O3): the former with a_1 - and the latter with t_2 - symmetry. In contrast, the oxygen $2p$ states in the region between -4.5 eV and the Fermi-level form bonding combinations with states of V $3d$ character. The conduction band starts after a band gap of around 1.7 eV. The low lying conduction band between 1.7 and 6.2 eV originates mainly from V $3d$ states with only a small $2p$ contribution from oxygen. Due to crystal field effects the d band is split into three parts. This can be understood by considering the double pyramid as a distorted octahedron, in which the z axis coincides with the direction of the vanadyl bond. The V d_{xy} orbital is found well separated at the bottom of the d band and forms π^* combinations with the oxygen ligands of the pyramid base. The intermediate block, also corresponding to antibonding π^* states, is made up from d_{xz} and d_{yz} orbitals. They are slightly shifted to higher energies because of the small bonding distance to the vanadyl oxygen in z direction. Antibonding σ^* states are formed by $d_{x^2-y^2}$ and d_{z^2} orbitals at the top of the d band. After an additional band gap of around 1 eV the conduction band is

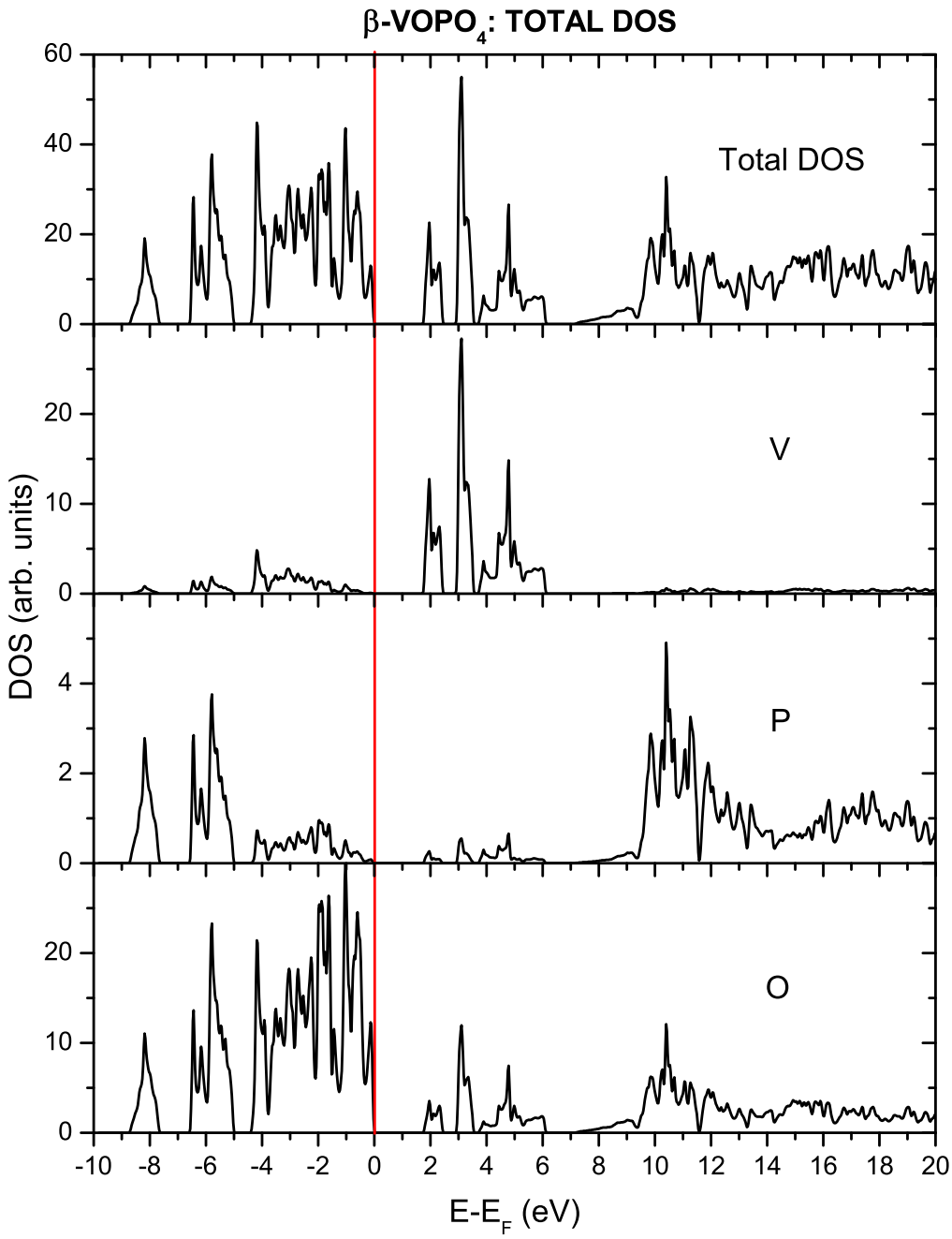

Fig. 5.7: Total DOS and the contributions of V, P and O to the DOS of β-VOPO$_4$. Note the different scaling for the intensities in the diagrams.

dominated by antibonding combinations of oxygen $2p$ states with phosphorus 3σ states. The appearance of oxygen $2p$ character over the whole range of unoccupied states as well as the mixing of vanadium $3d$ states with oxygen $2p$ states in the valence band attests a covalent contribution to the bonding.

Differently coordinated oxygens

The existence of structurally different oxygens (see Fig. 5.2) becomes evident when the conduction band region of the different atom projected DOS are compared with each other. In the case of the vanadyl oxygen O4 the hybridization with vanadium $3d$ states leads to very localized antibonding π^* states at around 3 eV. These states are formed by a combination of O4 $2p_x$ with V $3d_{xz}$ and O4 $2p_y$ with V $3d_{yz}$ orbitals, respectively. The remaining O4 $2p_z$ orbital contributes to a less localized σ^* combination with the V $3d_{z^2-r^2}$ orbital between 4.5 and 6.1 eV. The hybridization between these states is attested by the close agreement in the shapes of their projected DOS. Three structurally different oxygens set up the pyramid base. O1 makes up the two corners in the y-direction of the base and forms π^* combinations with the V $3d_{xy}$ orbital and σ^* combinations along the y direction between its $2p_y$ orbital and the V $3d_{x^2-y^2}$ orbital. O2 and O3 define the corners of the pyramid basis in x-direction. Their $2p_y$ orbitals form π^* combinations with the V $3d_{xy}$ orbitals, while their $2p_x$ orbitals form σ^* combinations with V $3d_{x^2-y^2}$ orbitals. Due to the longer bond length between the V atom and the oxygen atoms of the pyramid base compared to the bonding distance of the vanadyl oxygen (O4), the splitting between bonding and antibonding combinations is lower for the former. This explains the fact that the π^* and σ^* combinations formed in the pyramid plane (i.e. d_{xy} and $d_{x^2-y^2}$) lie lower in energy than those formed with the vanadyl oxygen. Since the oxygen atoms of the pyramidal plane also form a bond to a phosphorus atom, their $2p$-projected DOS show intensities from antibonding and bonding combinations with the P $3\sigma^*$ states which are absent in the case of the vanadyl oxygen O4. An overview of overlapping orbitals is given in table 5.1.

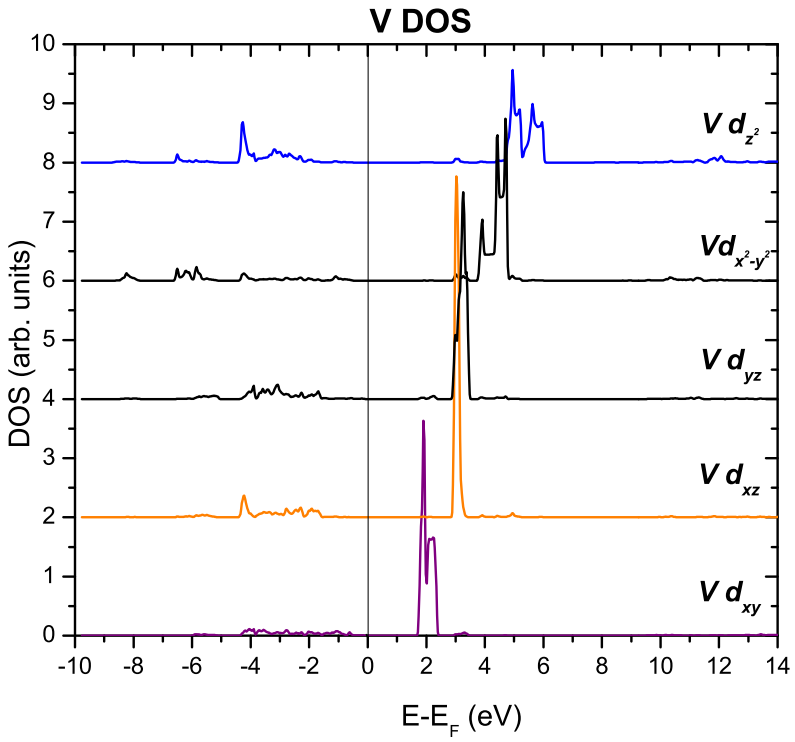

Fig. 5.8: β-VOPO$_4$: Vanadium $3d$ projected DOS. The five $3d$ states are aligned in energy position in accordance with the crystal field imposed by the geometry of the surrounding oxygen atoms.

	O1	O2	O3	O4
V $3d_{xy}$	$2p_x$	$2p_y$	$2p_y$	
V $3d_{xz}$		$2p_z$	$2p_z$	$2p_x$
V $3d_{yz}$	$2p_z$			$2p_y$
V $3d_{x^2-y^2}$	$2p_y$	$2p_x$	$2p_x$	
V $3d_{z^2}$				$2p_z$

Table 5.1: Summary of the main V $3d$ - O $2p$ orbital overlap contributions. The interaction of oxygen $2p$ states with the V $3d_{xy}$, $3d_{xz}$ and $3d_{yz}$ states are of π^*, those with $3d_{x^2-y^2}$ and $3d_{z^2}$ states of σ^* type, respectively.

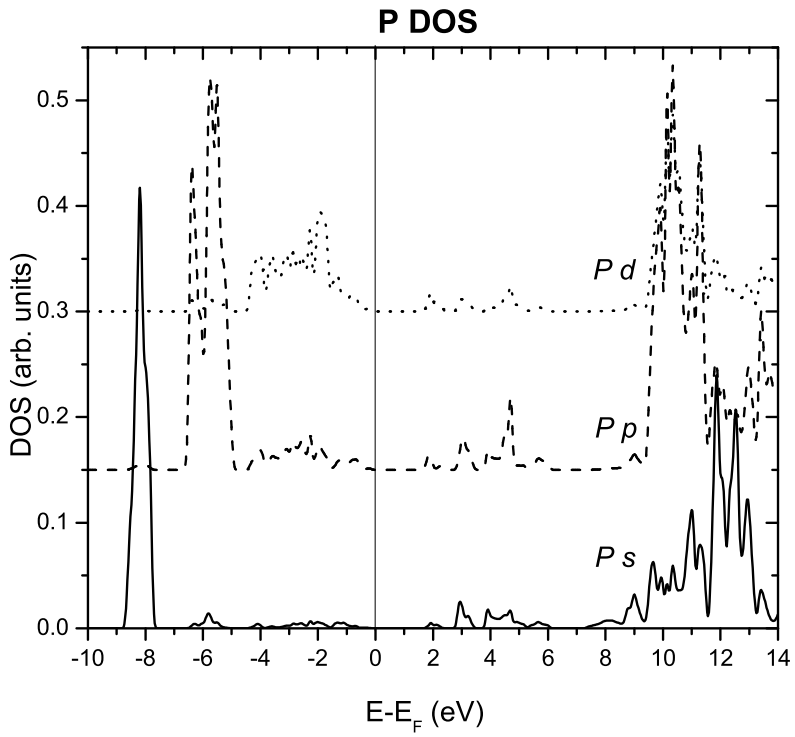

Fig. 5.9: β-$VOPO_4$: Phosphorus $3s$, $3p$ and $3d$ projected DOS. A clear splitting of the s, p and d contributions is observed below the Fermi level.

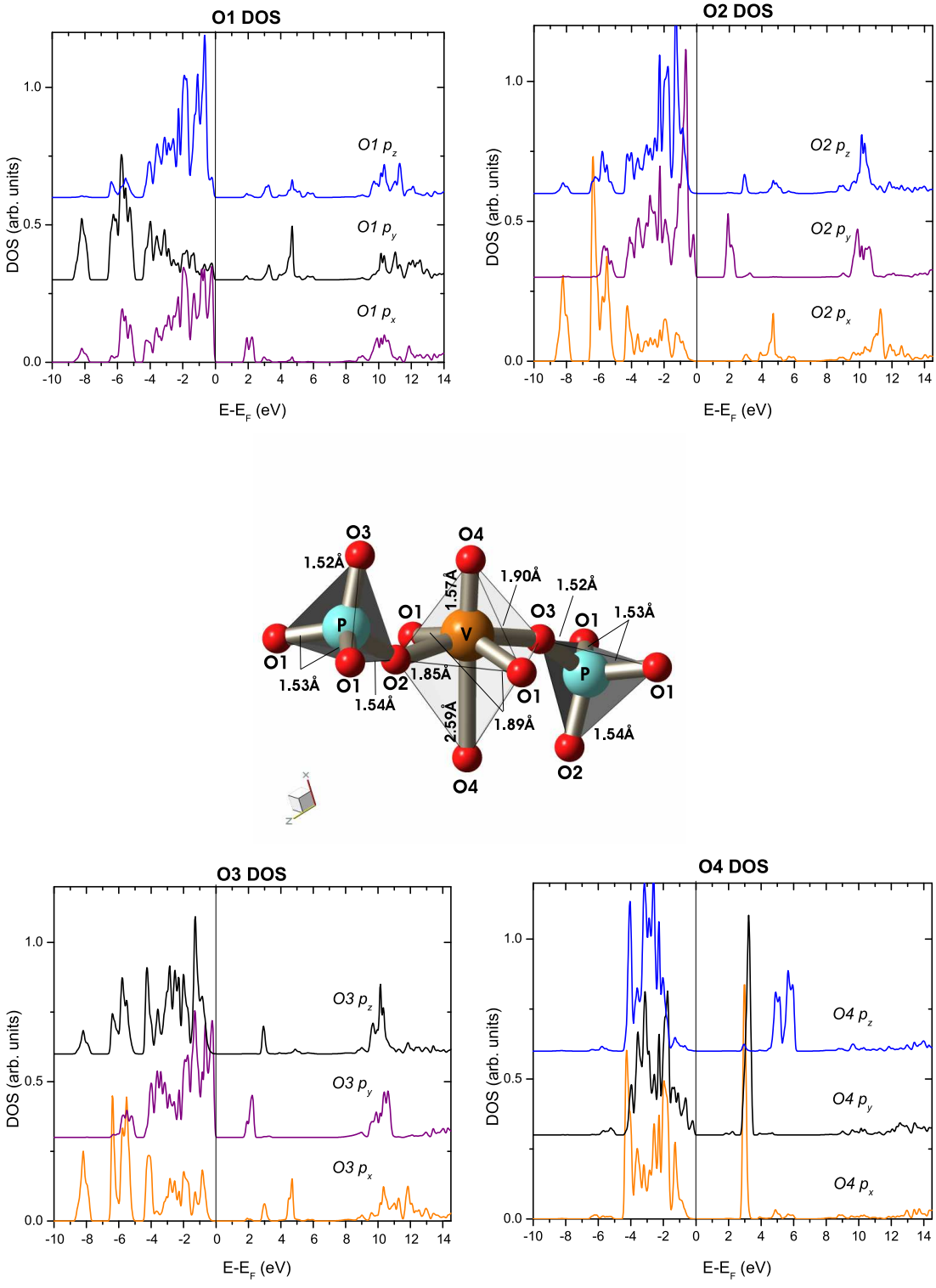

Fig. 5.10: β-VOPO$_4$: O1, O2, O3 and O4 $2p$ projected DOS.

O-K ELNES and V-K NEXAFS

EELS as well as NEXAFS were applied to probe the local electronic structure of oxygen and vanadium in β-$VOPO_4$, respectively. The shape of the vanadium and oxygen edges is strongly related to the oxidation state of the vanadium and to the distortion of the coordination polyhedron [67]. EELS measurements were performed in the energy region of the V $L_{2,3}$ and the oxygen K ionization edges. Vanadium oxides and vanadium phosphorus oxides are easily reduced by the electron beam in the TEM [67]. Therefore, special care was taken in order to minimize irradiation effects. A recorded spectrum is presented in Fig. 5.11 after background subtraction and multiple scattering correction [44]. The V $L_{2,3}$ ionization edges correspond to transitions from V $2p_{1/2}$ and $2p_{3/2}$ states to empty $3d$ states and show up as narrow peaks (white lines) at about 525.7 and 519 eV, respectively. From their position, the oxidation state of vanadium can be estimated [81] as +5. The maximum peak intensity of the two white lines is reversed with respect to the case of V_2O_5: while the intensity maximum of the L_2 edge is higher in the spectrum of V_2O_5, it is the L_3 edge that shows the highest intensity in β-$VOPO_4$. This is due to the different width of the $3d$ band in the two compounds. In principle, the ratio between the integrated L_3 and L_2 intensity should correspond to the statistical ratio of 2:1 in the case of a d^0 initial state, if the background in the spectrum is correctly removed (which is difficult in the case of overlapping edges). The 2:1 intensity ratio is a result of the different initial state occupation (4 electrons in a $2p_{3/2}$ versus 2 electrons in a $2p_{1/2}$ state). But due to the shorter lifetime of a hole in a $2p_{1/2}$ state (it can be filled via a Coster-Kronig decay from a $2p_{3/2}$ state), the lifetime broadening of the L_2 edge is slightly larger than the one of the L_3 edge [70]. The effect of this difference on the final spectrum is bigger in the case of narrow $3d$ states and has to be taken into account in the comparison of the white line ratios.

While the fine structure of the O K ionization edge resembles the density of unoccupied states of p character, the shape and intensity of the V $L_{2,3}$ edges are strongly influenced by electron correlation effects. As these effects are not accounted for within the present one-electron approximation, the simulation of their intensities fails. For this reason the following discussion is focused on the O K ionization edge.

Figure 5.11 shows the close agreement between simulation and experiment although the core hole left by the excited electron and the high-energy tail of the preceding V L_2 edge were not taken into account in the simulation. As already observed in the discussion of the DOS, the first empty states above the Fermi-level are formed by a combination of un-

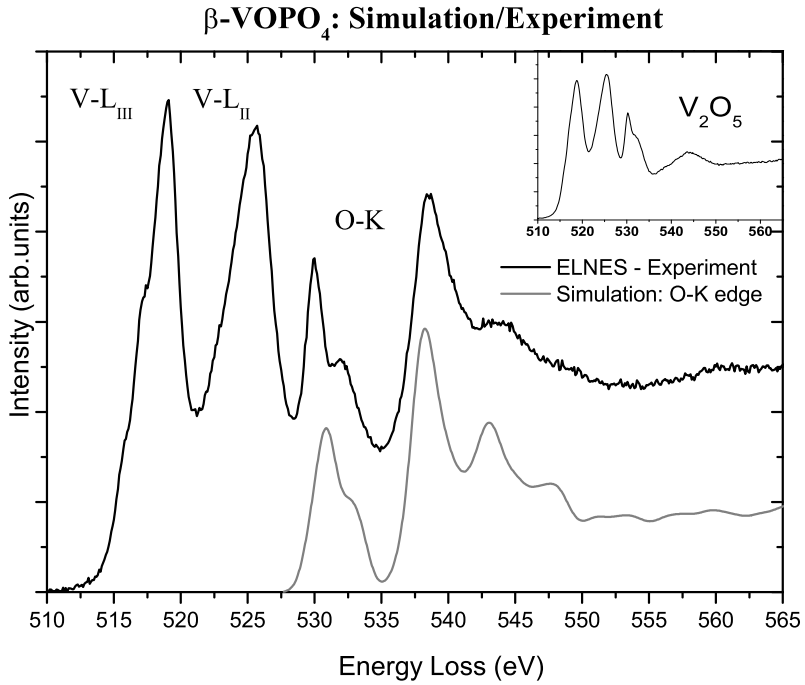

Fig. 5.11: EELS spectra of β-VOPO$_4$ and simulated oxygen K ionization edge (dotted line). For comparison, the spectrum of V_2O_5 is given in the upper right corner. The existence of distorted VO_5 pyramids in both compounds leads to the close agreement in the first region of the oxygen K edge.

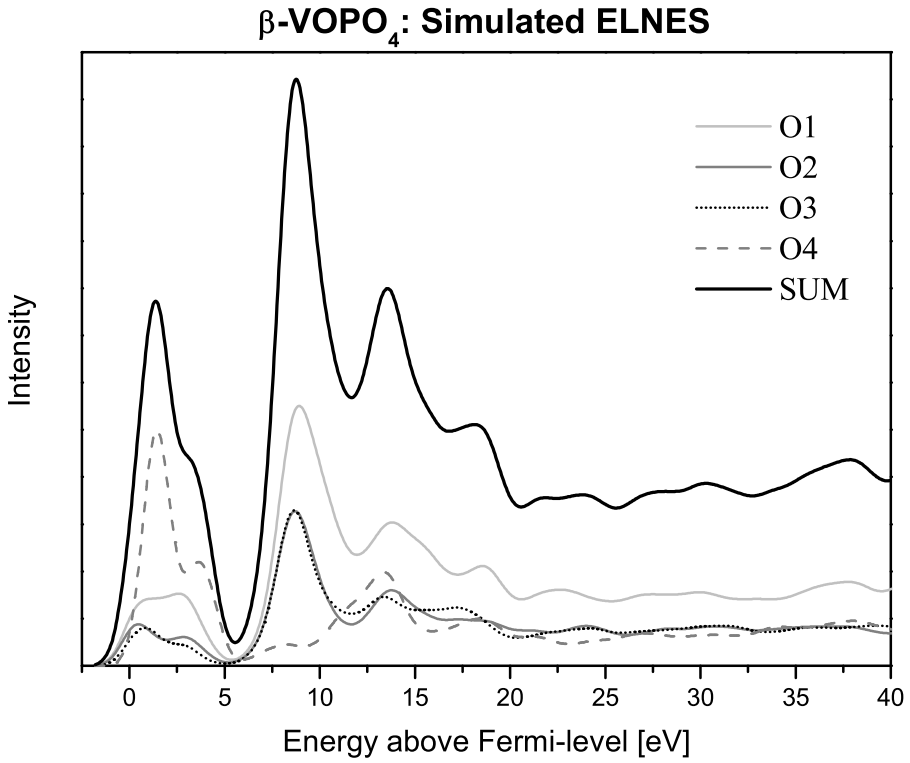

Fig. 5.12: Contributions of the different oxygens to the oxygen K ELNES of β-$VOPO_4$.

occupied V $3d$ states with some admixture of O $2p$ character. The shape of the O K-edge in the EELS spectrum between around 528 and 535 eV therefore resembles the electronic structure at the distorted VO_5 pyramid. This becomes evident when this region is compared to the spectra of V_2O_5 which consists of similarly distorted VO_5 pyramids (see inset in Fig. 5.11). Two clearly developed peaks, separated by a ligand field splitting of approx. 2 eV reproduce transitions from a oxygen $1s$ state into unoccupied π^* and σ^* states, respectively. Above 535 eV another feature arises from transitions into unoccupied states formed by hybridization of O $2p$ and P 3σ states. A closer insight into the structure of the O K-edge is gained by splitting it into the contributions arising from the differently coordinated oxygens as shown in Fig. 5.12. This clearly demonstrates the role of the tightly bound vanadyl oxygen for the development of the first peak. The contributions from O2 and O3 are very alike, reflecting the close agreement in their surrounding. O1 contributes with a higher weight to the spectrum since it occupies two equivalent positions in each VO_5 pyramid.

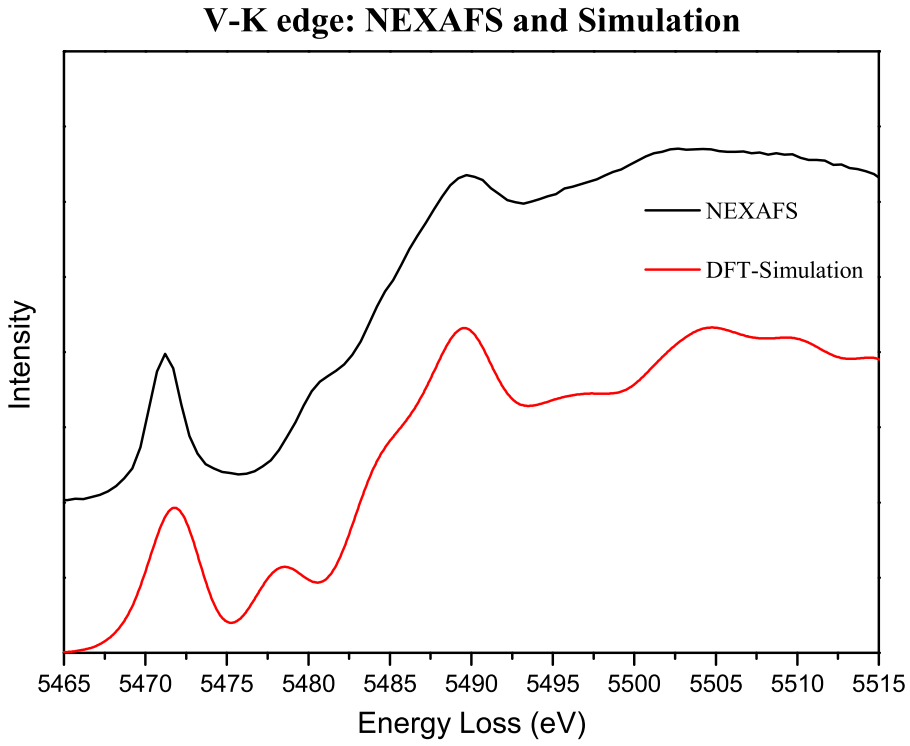

Fig. 5.13: β-$VOPO_4$: Vanadium K edge: NEXAFS experiment and DFT simulation (dotted line). Note that the energy scale of the simulated spectra was stretched by a factor of 1.2 (see text of more details).

The NEXAFS of the V K ionization edge, recorded at the Berlin electron synchrotron facility BESSY, is presented in Fig.5.13. Comparison with the simulated spectrum shows a good agreement although the energy scale in the simulation had to be stretched in order to account for self-energy effects. These effects, which are a consequence of the chosen exchange-correlation functional, are larger for the V K-edge than for the O K-edge. It is well known that generalized gradient ("GGA") functionals include unphysical electron self-interactions which lead to an energy dependent compression of the energy axis in the simulated spectra [82, 83].

A narrow pre-edge peak is observed in front of the main edge. It arises mainly from dipole transitions to the lowest empty states localized at the coordination polyhedron (i.e., the distorted VO_6 octahedron) of vanadium. As already discussed, these states are mainly made up from vanadium $3d$ atomic orbitals. Since the initial $1s$ state is a gerade state, the $1s \rightarrow 3d$ transition is strictly dipole forbidden. Transitions into these final states can therefore only occur because of the nonzero p-component relative to the vanadium atom, which is induced by the distortion of the coordination polyhedron. Lowering the symmetry of the ligands from O_h leads to the breaking of the inversion center and to a stronger $3d - 4p$ mixing and overlap of the $3d$ orbitals with the $2p$ orbitals of the ligands.

The observed p-d mixing, which is also a measure for the covalent character of a bond, can mainly be traced back to the bond formed between vanadium and the vanadyl oxygen.

This can be seen in Fig. 5.14, where a comparison of the simulated shapes of the oxygen and vanadium K ionization edge monitors the development of the $2p$ character over the region of the edges. In the region of the pre-edge peak between 0 and 5 eV, the intensity of the oxygen K edge mirrors the oxygen $2p$ character in the $3d$ dominated unoccupied DOS. The intensity of the V K edge in the same energy region rises with increasing degree of hybridization between oxygen $2p$ states and vanadium $3d$ states and therefore mirrors the the $2p$ character in the unoccupied DOS induced by covalency. This p-d mixing is biggest in the case of the hybridization between the vanadyl oxygen $2p_z$ and the vanadium $3d_{z^2}$ state, at which the pre-edge peaks. The strength of this bond is related to the distortion of the coordination polyhedron. Since the distortion of the coordination polyhedron is related to the oxidation state of vanadium, the intensity of the pre-edge peak in the vanadium K ionization edge can be used as a measure for the oxidation state of vanadium.

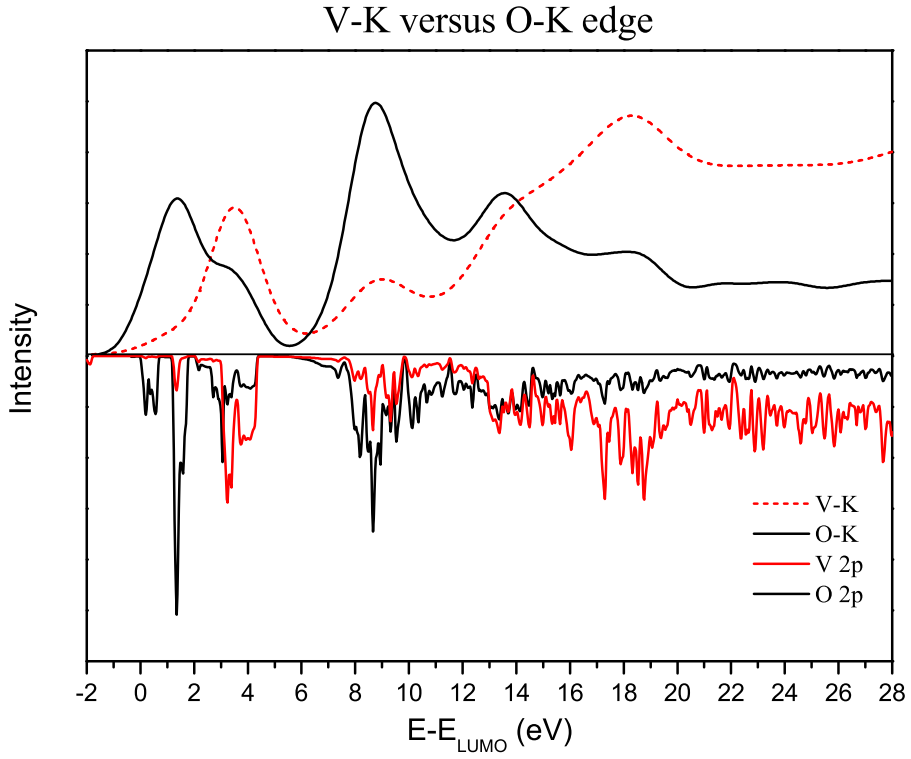

Fig. 5.14: Vanadium and oxygen K ionization edge of β-VOPO$_4$. Both spectra have common features with intensities related to the corresponding $2p$ projected DOS. The rising $2p$ character in the $3d$ dominated DOS of vanadium in the pre-edge region is related to a rising degree of covalency.

5.3 α_{II}- and α_I-$VOPO_4$

In this section, the α_{II}- and α_I-$VOPO_4$ phases are investigated. The result of structure optimizations are presented and details of the bulk electronic structure are discussed in view of differences in the geometric structure of the polymorph.

5.3.1 Synthesis and characterization

Different synthesis routines for α_I- and α_{II}-$VOPO_4$ are reported in the literature [33, 84]. The α_{II}-$VOPO_4$ sample studied in this work was synthesized by dehydration of $VOPO_4 \cdot 2H_2O$ in dry air at 750°C for 17h with a heating rate of 4°C. The hydrate has a structure belonging to the same space group as α-$VOPO_4$. During the decomposition of the hydrate, the water molecules that link the layers are removed.

α_I-$VOPO_4$ was obtained by decomposition of the same precursor, $VOPO_4{\cdot}2H_2O$, at 650°C and otherwise similar conditions as above. As already mentioned in the introduction to the V^{5+} phases, both α-phases can be transformed to β-$VOPO_4$ in air or O_2: α_{II} is transformed to β-$VOPO_4$ above 750°C and α_I-$VOPO_4$ is first transformed to α_{II} near 720°C and finally to β-$VOPO_4$ [1].

Characterization of α_{II}-$VOPO_4$

Synthesis of pure α_I-$VOPO_4$ is very difficult and the characterization is complicated by the fact that α_I-$VOPO_4$ hydrates in air within a few minutes [73]. For this reason, the discussion of the α_I phase is focused on theoretical results and here, only the characterization of the α_{II}-phase is presented .

The synthesized α_{II}-$VOPO_4$ was characterized in a similar manner as β-$VOPO_4$, using scanning electron microscopy (SEM) and energy dispersive X-ray detection (EDX), X-ray diffraction (XRD) and high resolution transmission electron microscopy (HRTEM).

SEM images of the sample reveal nice flat particles with a clean surface and uniform thickness, indicating that the α_{II} phase crystallizes in a layered structure. The atomic ratios measured with EDX are consistent with the stoichiometry of α_{II}-$VOPO_4$.

XRD measurements obtained using Cu K_α radiation in the angular range (2θ) of 15 ° to 75 ° show a good crystallinity of the sample (see Fig 5.16). A comparison with the simulated (PowderCell software [80]) X-ray diffraction diagram reveals that the most intense

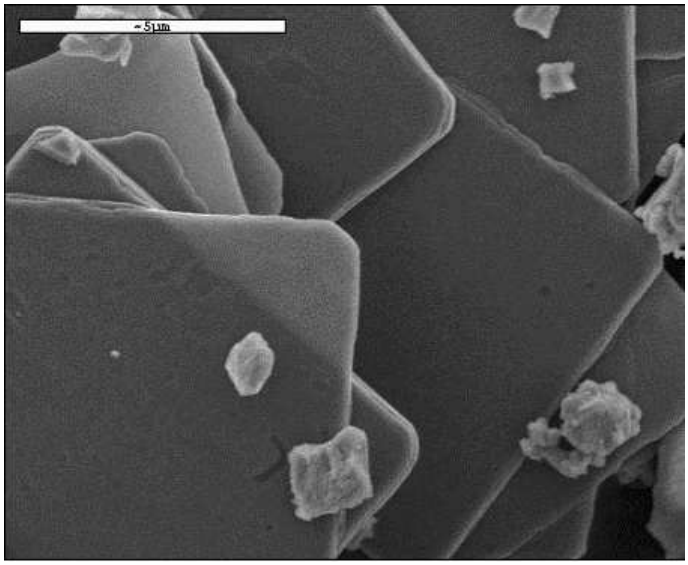

Fig. 5.15: SEM image showing that the morphology of α_{II}-VOPO$_4$ is dominated by large and flat plates.

reflections of the α_{II}-phase are present, but additionally, strong reflections which can be attributed to the γ-phase are present. The sample corresponds therefore to a mixture of α_{II}- and γ-VOPO$_4$. Besides that, it is reasonable that small portions of phases which are below the detection limit of XRD are also present.

Crystallites of the α-VOPO$_4$ phase can be identified by using HRTEM and electron diffraction techniques. The observed lattice fringes of HRTEM images such as the one shown in Fig 5.17 are in agreement with the α_{II}-VOPO$_4$ phase. But since both α-VOPO$_4$ phases preferentially expose the (001) faces and because of the close agreement in their *a* and *b* unit cell parameters it is difficult to unambiguously distinguish between α_I and α_{II} polymorph by using HRTEM imaging and selected area diffraction.

The α_{II}-phase is much more prone to electron beam irradiation than the β phase and lattice fringes disappear after a few seconds of irradiation. Therefore, special care has to be taken in order to keep the intensity and dose as low as possible in order to prevent the reduction and amorphization of the sample.

5.3.2 Geometric Structure of α_{II}-VOPO$_4$

α_{II}-VOPO$_4$ crystallizes in a layered structure with layers made up from VO$_5$ pyramids linked together by PO$_4$ tetrahedra as shown in Fig. 5.18.

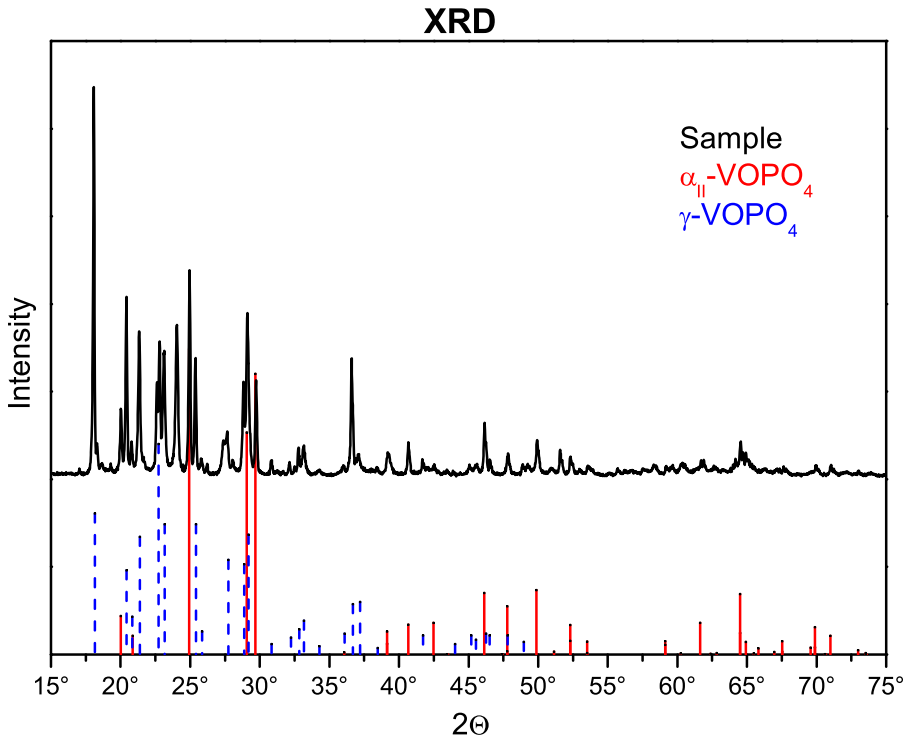

Fig. 5.16: XRD spectra of the synthesized product. The peaks can be assigned to a mixture of α_{II}- and γ-$VOPO_4$.

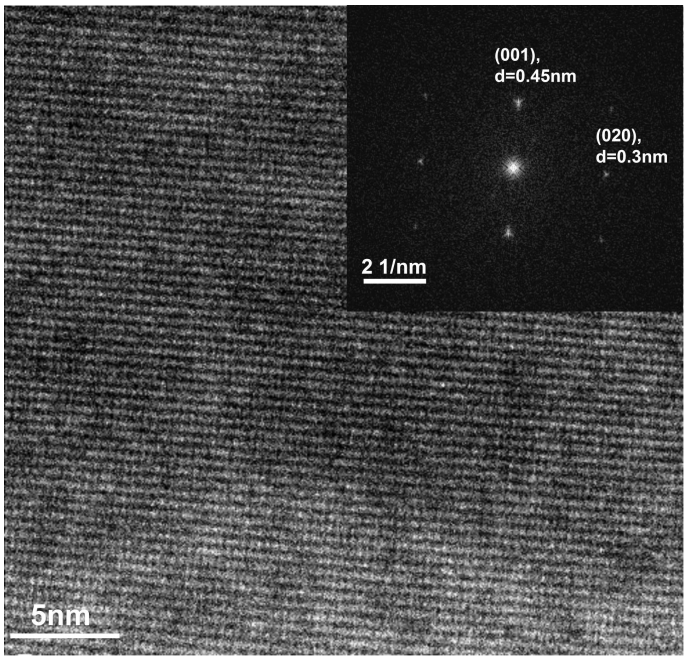

Fig. 5.17: HRTEM image of α_{II}-$VOPO_4$ in the [100] zone axis. In the top right corner the Fourier transformation is shown. Variations in the contrast in the image are due to thickness variations.

Two structurally different oxygens are present in α_{II}-$VOPO_4$: the vanadyl oxygen, O1, and the bridging oxygen, O2 (see Fig. 5.18). The singly coordinated vanadyl oxygen defines the pyramid axes by a short V=O double bond of 1.59 Å and an additional, faint interaction with a vanadium atom in the adjacent layer at a distance of 2.85 Å. In the α_{II}-$VOPO_4$ structure, layers are connected in a zip-like manner via the outermost vanadyl groups. The weak interlayer bonding can be described as a weak Lewis acid → Lewis base interaction (V=O→V=O). In the resulting layers, the vanadium and phosphorus atoms lie on alternate sides of the pyramid bases and the V=O vanadyl bonds point outside of the layers. Additionally, the vanadium atom is shifted from the center of the square plane toward the vanadyl oxygen in a manner typical for vanadium in a 5+ oxidation state. Bridging oxygen atoms define the corners at which the VO_5 pyramids are linked with the PO_4 tetrahedra. They form a bond with one vanadium and one phosphorus atom at 1.9 Å and 1.55 Å, respectively. Each PO_4 tetrahedra is oriented such that it spans the space between four VO_5 pyramids within a layer.

In α_{II}-$VOPO_4$, the vibration amplitude of the V atom along z is much larger than in the other directions [85]. Changes of the position of vanadium inside the octahedron are thus

possible without significantly changing the arrangement of the octahedra and tetrahedra of a sheet. This leads to the structurally closely related α_I phase.

5.3.3 Geometric Structure of α_I-$VOPO_4$

The α_I-$VOPO_4$ phase is supposed to be isostructural with α-$VOSO_4$ [71]. Its structure is closely related to the structure of the α_{II}-$VOPO_4$ phase. In going from α_{II}-$VOPO_4$ to α_I-$VOPO_4$, the vanadium atoms basically shift from one side of the equatorial plane to the other, followed by a decrease of the height of the octahedron along the z axis and a slight elongation of the edge of the equatorial square (see Fig. 5.18). As a result, the vanadium and phosphorus atoms are situated on the same side of the pyramid base in α_I-$VOPO_4$ and the vanadyl bond points into the plane.

α_I-$VOPO_4$ contains two structurally different oxygens of the same type as $\alpha_{II}-VOPO_4$ with only slightly different bonding distances and, in the case of the bridging oxygen, also bond angles. In the final unit cell obtained after structure optimization, the bond length of the vanadyl oxygen measures 1.59 Å for the short double bond and 2.53 Å for the weak interaction with the vanadium atom of the next pyramid. The bridging oxygen forms bonds at 1.55 Å and 1.9 Å with a phosphorus and a vanadium atom, respectively. Similarly to α_{II}, the primitive cell comprises two formula units.

5.3.4 Structure optimization

As already mentioned, it is the similarity between the various $VOPO_4$ phases that makes the synthesis of pure phases and hence the structure determination by means of X-ray or neutron diffraction technique very difficult, except for the more stable β-$VOPO_4$ phase.

Density functional theory provides an elegant framework in which the total energy of solid-state systems can be obtained for any geometrical configuration of the nuclei. This method can therefore be used to determine the total energy of different arrangements and lattice constants of a compound. Experimentally obtained atomic positions are used for the initial calculation and the free internal structural parameters are optimized using the calculated forces on the nuclei in an iterative way. The force minimization was performed using the PORT method as implemented in the Wien2k code [51].

α_{II}-VOPO$_4$

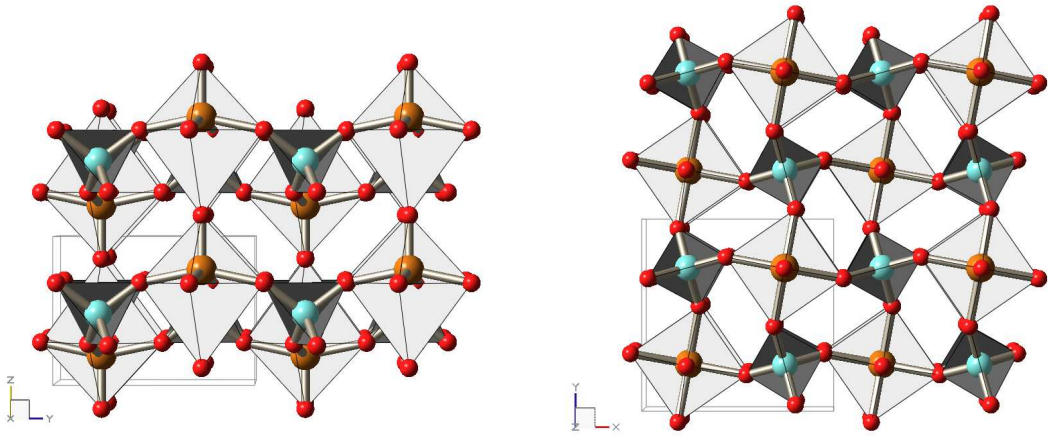

[100] [001]

α_I-VOPO$_4$

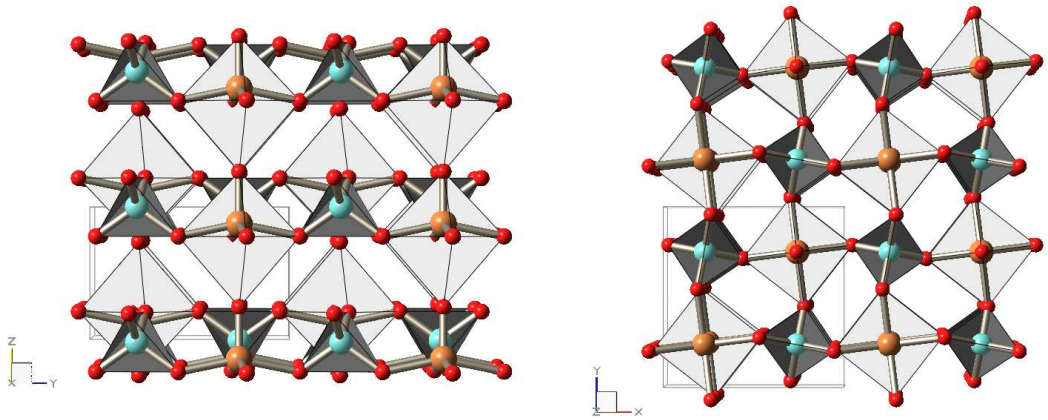

[100] [001]

Fig. 5.18: Crystal structure of α_{II}- and α_I-VOPO$_4$ viewed from [100] and [001] direction. The orthorhombic unit cells are indicated; *a*, *b* and *c* are parallel to the *x*, *y* and *z* axis, respectively. In the figures, vanadyl oxygens, O1, are only bonded to vanadium and bridging oxygens, O2 are bond to one vanadium and one phosphorus atom. For clarity, groups of atoms are combined to VO_6 octahedra (grey) and PO_4 tetrahedra (dark grey).

Basis set used in the calculations

The calculation for α_I- and α_{II}-$VOPO_4$ were performed with 65 k-points in the irreducible part of the Brillouin zone and a plane wave cut-off parameter R_{kmax} of 7.0 (corresponding to an energy cut-off of 28.7 Ry) after a thorough testing of the basis set convergence as shown in Fig. 5.19. The values of muffin-tin sphere radii were taken equal to 1.45 Bohr for V and P and 1.3 Bohr for O, respectively.

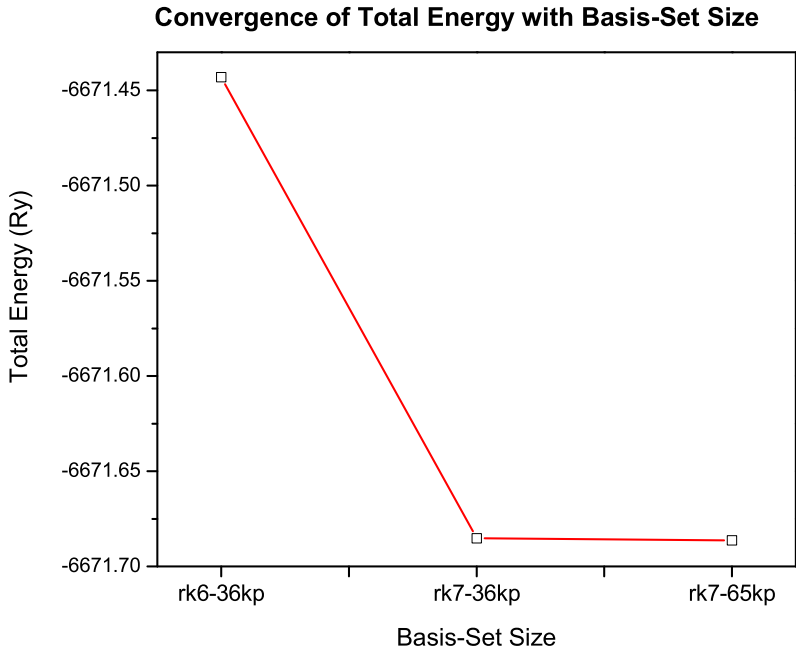

Fig. 5.19: Total energy versus basis set size used for the simulation of α_{II}-$VOPO_4$. The numbers labeled with rk and kp are the values of Rk_{max} and the number of k-points in the irreducible Brillouin zone, respectively.

Structure optimization: α_{II}-$VOPO_4$

Starting with the crystallographic data provided in the literature [86,87], the total energy was minimized in a first step as a function of the unit cell dimensions by varying *c* versus *a* and *b* at constant volume and *a/b*-ratio. According to Fig. 5.20 the total energy reached a minimum for unit cell dimensions only slightly smaller (less than -0.5%) than those reported in the literature [4,86,87]. This is due to the fact that DFT simulations with a LDA or GGA exchange-correlation potential in general tend to over-bind and hence result in smaller lattice distances than the experimentally observed ones. In a second step, the

structure was further optimized by relaxing the positions of the atoms according to the derived forces [51] acting on the nuclei. During the search for the equilibrium positions the symmetry constrains of the space group were conserved.

In principle, the unit cell parameters have to be optimized after each relaxation and vice versa. But since the forces were small from the beginning of the structure optimization procedure and due to the fact that the unit cell parameters are easier to determine experimentally with higher accuracy than the atomic positions, the atomic positions were relaxed without further optimizing the dimensions of the unit cell. The optimization was stopped after the convergence criteria was fulfilled (forces below 2 mRy/a.u.). The arrangement of atoms in the structural units of α_{II}-VOPO$_4$ after structure optimization is shown in Fig. 5.23. Table 5.2 presents the derived atomic positions after structure optimization. For comparison, the atomic positions that are reported in the literature [87] are also given. During the optimization, the bonding distance of the P-O bonds decreased slightly (from 1.543 Å to 1.541 Å), while the distances from vanadium to oxygen atoms was slightly increased (from 1.578 Å to 1.585 Å in the case of the vanadyl oxygen and from 1.858 Å to 1.870 Å in the case of the bridging oxygens).

	optimized			literature		
	x	y	z	x	y	z
V	0.250000	0.250000	0.212026	0.250000	0.250000	0.213900
P	0.250000	0.750000	0.250000	0.500000	0.750000	0.500000
O1	0.250000	0.250000	0.854567	0.250000	0.250000	0.858000
O2	0.195120	0.950403	0.296806	0.196500	0.952200	0.298700

Table 5.2: .
Optimized fractional coordinates of the α_{II}-VOPO$_4$ structure.

Structure optimization: α_I-VOPO$_4$

As a starting point for the structure determination of α_I-VOPO$_4$, the fractional coordinates of the atoms in the unit cell of α-VOSO$_4$ [71] were applied to the experimentally deduced unit cell dimensions of α_I-VOPO$_4$ [1, 4, 33]. The relaxation of the atomic positions were performed until the forces converged to values below *3.5 mRy/a.u.* The graph shown in Fig. 5.22 shows the convergence behavior of the total energy with the number of minimization steps.

As a reference, an additional calculation was performed for a different hypothetically

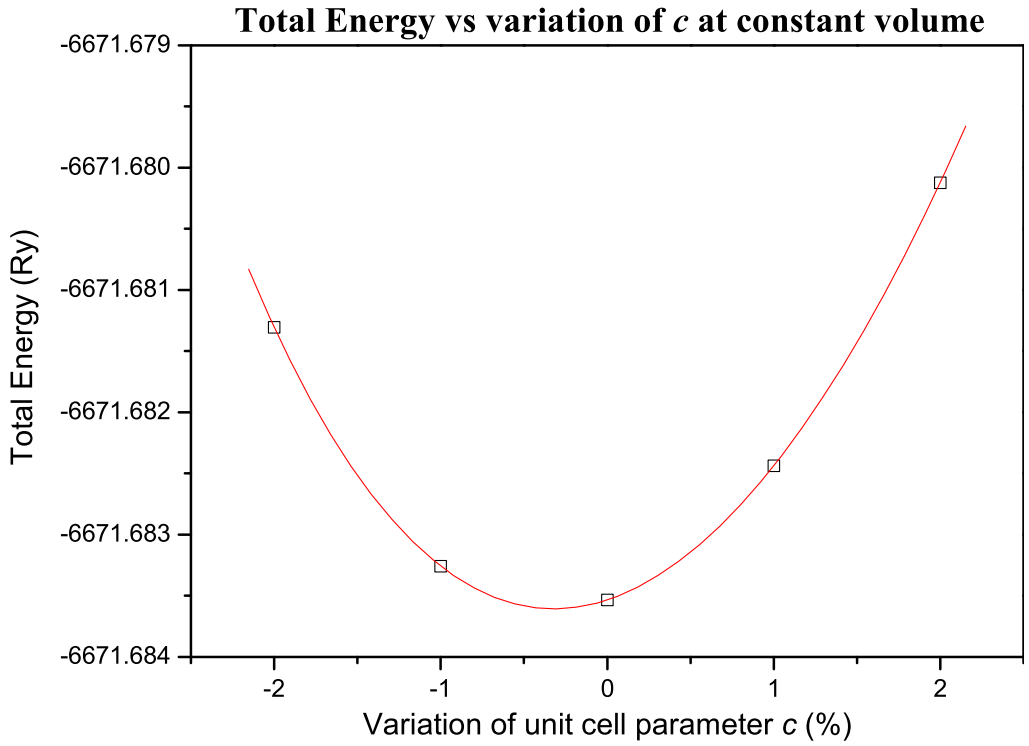

Fig. 5.20: Change of the total energy of α_{II}-$VOPO_4$ with respect to changes in the c/a ratio at a constant volume and a/b ratio

possible arrangement of VO_5 and PO_4 units. The total energy per atom calculated for the structure presented in Fig. 5.21 lies slightly higher than the one in the α-$VOSO_4$ structure of the above structure by 2 mRy. The difference in total energy is very small. Nevertheless, the hypothetical structure is discarded for the moment and the structure that is iso strucural with α-$VOSO_4$ is considered as the real structure of α_I-$VOPO_4$.

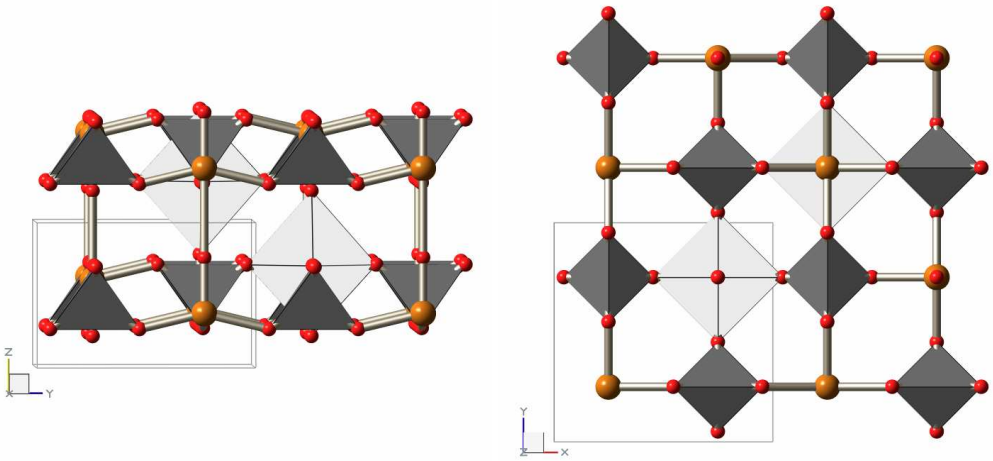

Fig. 5.21: Hypothetical $VOPO_4$ structure with slightly different arrangement of VO_5 and PO_4 building blocks.

The arrangement of atoms in the structural units of α_I-$VOPO_4$ after structure optimization is shown in Fig. 5.23.

5.3.5 Electronic structure

Electron density

Plots of the difference between converged crystalline charge density and the superposition of atomic densities of α_{II}-$VOPO_4$ and α_I-$VOPO_4$ are presented in Fig. 5.24. The difference density is shown for a (010) plane passing through V=O bonds. The redistribution of charge in the crystal with respect to superposed atomic charge nicely points out the covalent character of the V=O bond and the bonds between the phosphorus and oxygen atoms in the PO_4 units. On the other hand, a more ionic kind of interaction is found between the oxygens of the pyramid plane and the vanadium atom of the VO_5 unit. The weak interaction between the sheets, specially in the case of the α_I phase becomes obvious from Fig. 5.24 and has direct consequences in properties such as the observed

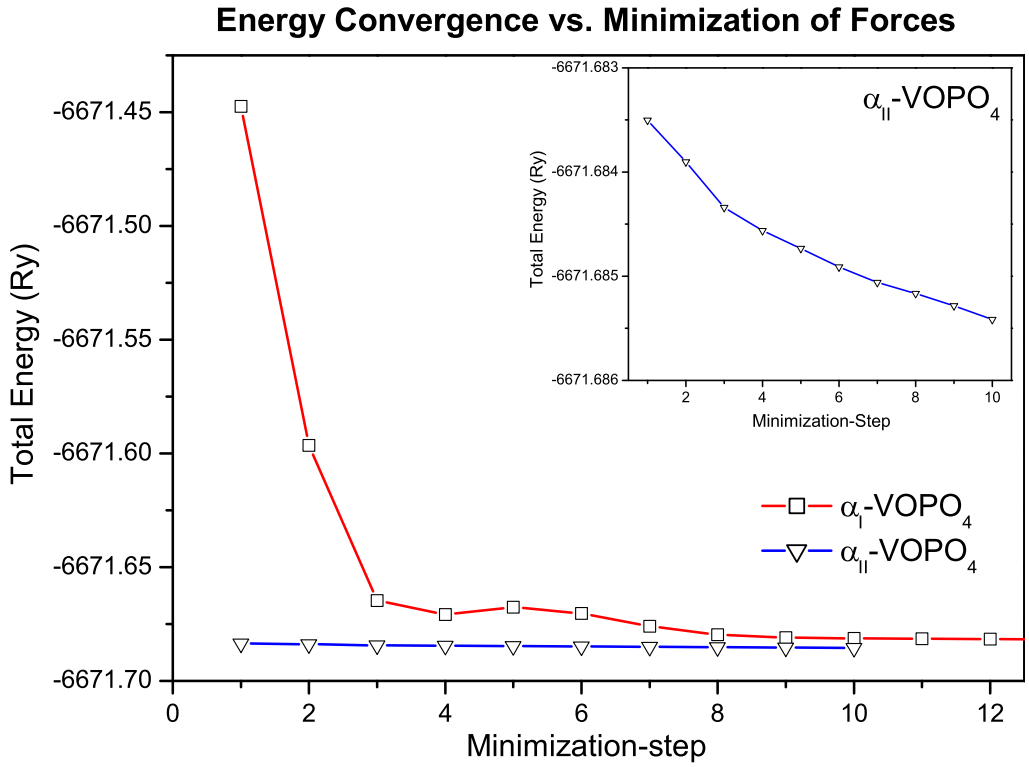

Fig. 5.22: Convergence of the total energy during minimization of the forces acting on the individual atoms in α_I- and α_{II}-$VOPO_4$.

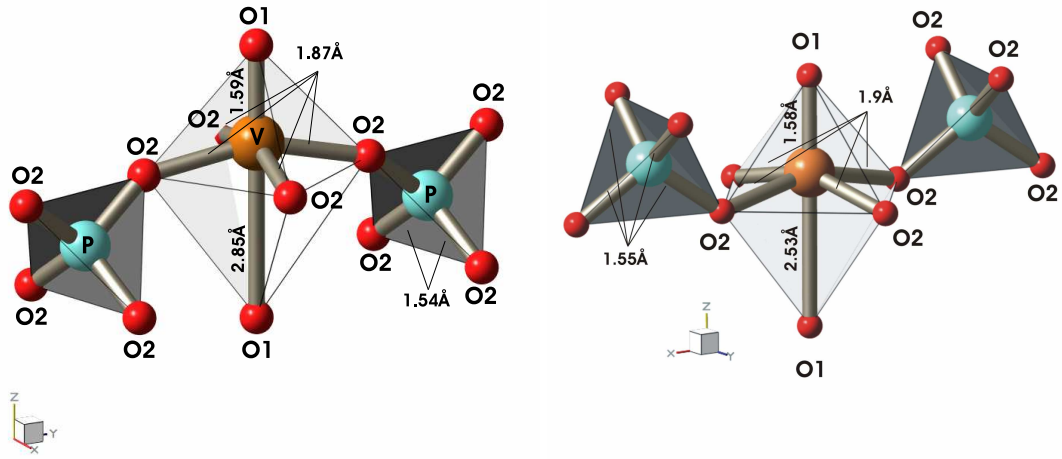

Fig. 5.23: Arrangement and bonding distances of the different oxygens in α_{II}- and α_I-$VOPO_4$ after structure optimization.

difference in the hydration behavior of the α_I and α_{II} phase. Indeed, Ben Abdelouahab *et al.* [73] reported that first changes in the Raman spectrum of α_I are visible after a few minutes in air saturated with water and that the hydration is complete within 45 minutes, whereas α_{II} hydrates completely within 4h.

Density of states

Total DOS

The total DOS and the contributions from vanadium, oxygen and phosphorus to the DOS in the energy region between -10 and 20 eV around the Fermi-level are presented in Fig. 5.25. Similarly to the case of β-VOPO$_4$, the DOS consists of three blocks of bands below the Fermi-level. Oxygen states are mixed with phosphorus states in the lower two sets of bands between -9 and -5 eV and with vanadium states in the energy range between -4.5 eV and the Fermi-level. The first region above the Fermi-level is dominated by antibonding states of mainly vanadium $3d$ character with some oxygen $2p$ admixture. Above 7 eV, the unoccupied DOS is dominated by the antibonding counterpart of the covalent oxygen - phosphorus bonds and some small contributions from unoccupied vanadium $4s$ and $4p$ states. Slight differences in position, width and intensity of features in the DOS of the two polymorph correspond to differences in dispersion and energy of the underlying bands. They are directly related to structural differences between the phases and will be discussed in more detail in the following.

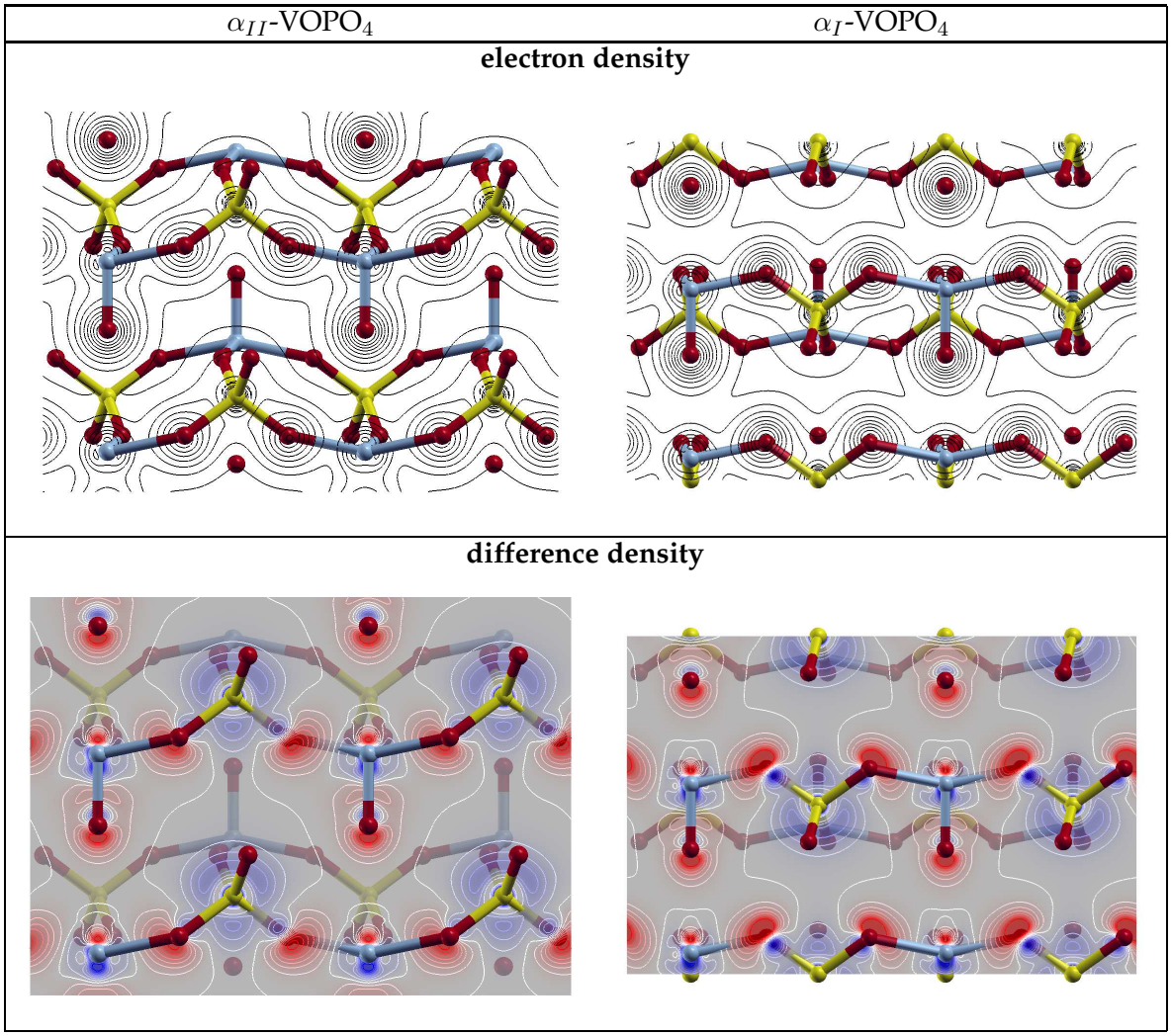

Fig. 5.24: Electron density and difference density plot of α_{II}- and α_I- $VOPO_4$. The electron density plot contains 10 contour lines spanning a range from 0 to 5 e/Å^3 on a sqrt scale. The difference density plots in the lower part show the difference between converged crystalline electron density and the superposition of the atomic densities. The density is given in the range between -0.7 (blue color) and 0.7 e/Å^3 (red) on a linear scale. Contour levels correspond to steps of 0.10 e/Å^3.

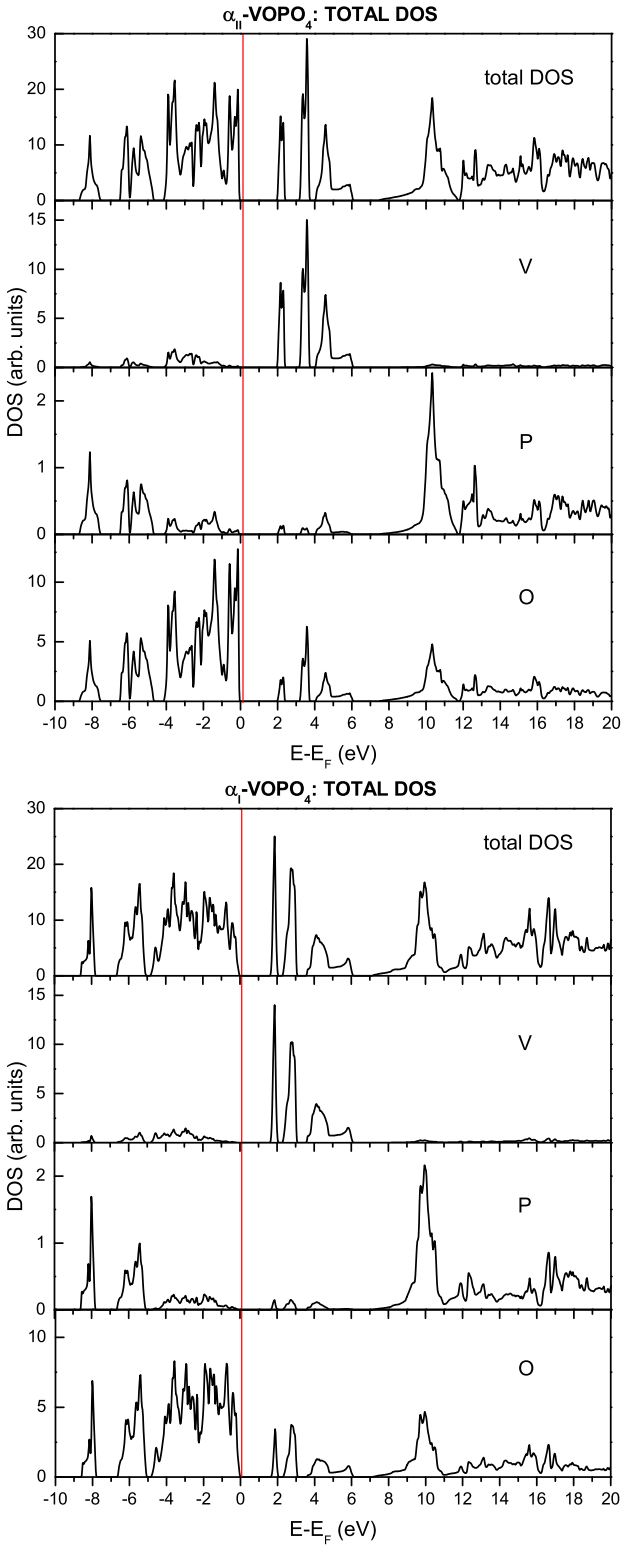

Fig. 5.25: Total DOS and the contributions of V, P and O to the DOS of α_{II}- and α_I-VOPO$_4$. Note the different scaling for the intensities in the diagrams. The total DOS in the top diagram corresponds to the sum of the atom projected DOS plus the DOS in the interstitial

Projected DOS

A deeper insight into the bonding relations and the hybridization of states is obtained form the angular momentum projected DOS at the vanadium, phosphorus and oxygen sites, which are presented in the Figures 5.26 - 5.28.

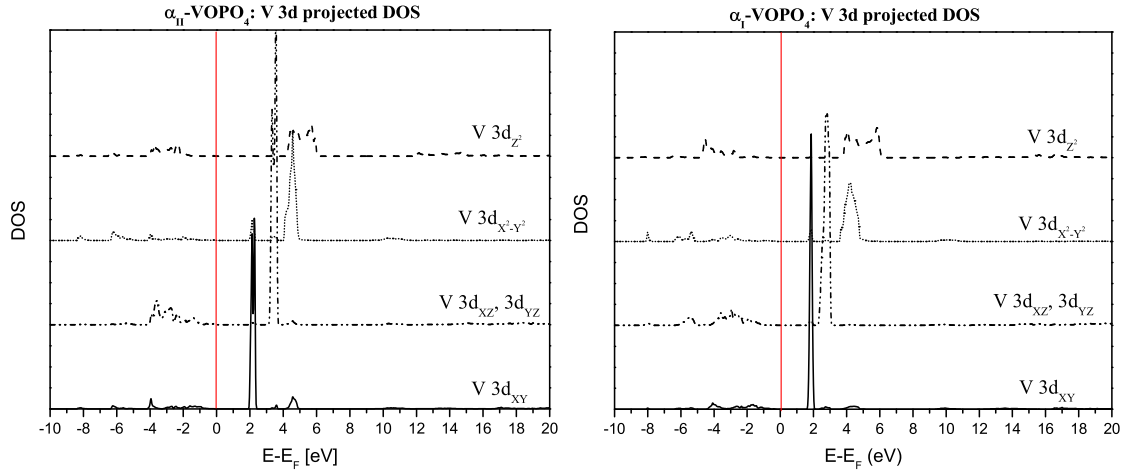

Fig. 5.26: α_{II}- and α_I-$VOPO_4$: Vanadium $3d$ projected DOS.

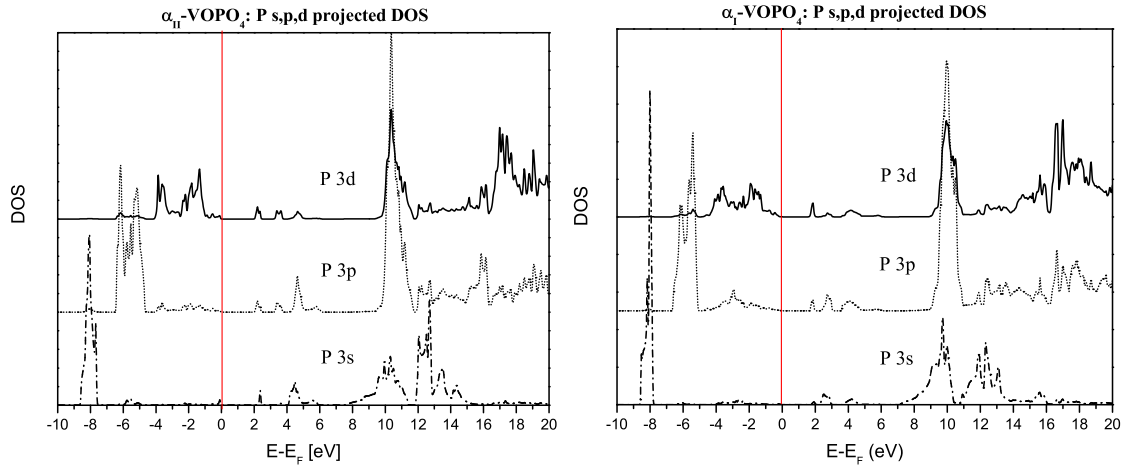

Fig. 5.27: α_{II}- and α_I-$VOPO_4$: Phosphorus $3s$, $3p$ and $3d$ projected DOS.

As opposed to β-$VOPO_4$, the d_{xz} and d_{yz} states are degenerate in the α phases, due to the higher symmetry of their VO_5 pyramids (see Fig. 5.33). For the same reason, the divergence of the d_{xy} band is smaller in the latter phases as compared to the β phase, where the oxygens in the basal plane of the pyramid are found at different bonding distances.

The same is valid for the dispersion of the $d_{x^2-y^2}$ band. The energy position of the empty d_{xy} and $d_{x^2-y^2}$ bands is related to the distance between the vanadium atom and the oxygen atoms of the pyramid plane. In α_{II} this distance measures 1.87 Å and the two bands appear between 2 - 2.4 eV and 4 - 5 eV, respectively. In α_I this V-O distance is slightly larger (1.9 Å) and the corresponding bands are found between 1.6 - 2 eV and 3.5 - 5 eV. The empty d_{xy} and $d_{x^2-y^2}$ states are pushed further above the Fermi-level in α_{II}. This is because the splitting between bonding and antibonding combinations increases with decreasing distance and with increasing interaction between the bonding partners. This effect is visible, although the difference in bond length is very small. In the β-phase, the distances from the vanadium to the oxygens of the basal plane ranges from 1.85 to 1.90 Å and the resulting d_{xy} and $d_{x^2-y^2}$ bands are therefore less localized. Things are getting more complicated when leaving the pyramidal plane. An investigation of the degenerated $3d_{xz}$ and $3d_{yz}$ bands reveals that the dispersion is higher in α_I and at the same time, the splitting from the $3d_{xy}$ band is smaller as compared to α_{II}. The appearance of these states at lower energy results from the presence of upwards tilted PO_4 units in α_I. They have a destabilizing effect on the $3d_{xz}$ and $3d_{yz}$ bands and bring them thereby closer to the $3d_{xy}$ states. Empty $3d_{x^2-y^2}$ and $3d_{z^2}$ states are broader and appear at higher energy since they form stronger sigma interactions with oxygens of the bridging and the vanadyl oxygens, respectively. Phosphorus $3s$, $3p$ and $3d$ states are shown in Fig. 5.27. The bonding s, p and d states appear in a row of clearly separated energy regions of increasing width. Phosphorus contributions to the DOS are complementary to the vanadium contributions, since vanadium states are mainly located in regions where the phosphorus contributions are minuscule and vice versa. It is the task of the oxygen atoms to bridge the energy regions of the two. The situation is clear in the case of the vanadyl oxygen, which only forms π interactions between its $2p_x$ and $2p_y$ states and the vanadium $3d_{xz}$ and $3d_{yz}$ states and stronger σ interactions with the vanadium $3d_{z^2}$ state in the same manner as already discussed for the β-$VOPO_4$ phase (see Fig. 5.28). The oxygens of the pyramid plane are more involved in the relatively stronger covalent interaction with the phosphorus atom than in the interaction with the vanadium atom which is weaker and mainly of ionic type. They provide sp^2 orbitals for bond formation with phosphorus sp^3 states in the range between around -9 and -4 eV. The corresponding antibonding states appear in the DOS of phosphorus and oxygen in the energy range between 9 and around 19 eV. A slight ionic interaction with vanadium $3d_{xz}$, $3d_{yz}$ and $3d_{x^2-y^2}$ is also evident from common features in the DOS of the both at an energy of around 3 to 5 eV. Only two $2p$ and one s orbital are involved in the formation of sp^2 hybrids at the bridging oxygens.

The remaining $2p_x$ orbital can be considered as the orbital that holds the lone pair, as can also be seen in the electron density plot shown in Fig. 5.29. It is only slightly involved in π^* interactions with the vanadium $3d_{xy}$ states at energies slightly above and below 2 eV in α_{II}- and α_I, respectively. But the same orbital also contributes to interactions with phosphorus states around -6 and above around 9 eV.

Some statements about the width of the vanadium $3d$ states:
The oxygens of the pyramid plane are "more involved" in the covalent interaction with the phosphorus atom as in the interaction with the vanadium atom, which is less strong and mainly of ionic type. Additionally, the vanadium-vanadium distance is relatively large due to the separation of VO_5 pyramids by the PO_4 units. As a consequence, the unoccupied vanadium $3d$ states are very localized and narrow. On the other hand, in the case of the binary vanadium oxides such as V_2O_5, the oxygens of the pyramidal plane are only involved in interactions with vanadium atoms (with two vanadium atoms in the case of bridging oxygen atoms and three in the case of the chain oxygen atoms (see Chapter 4)). In this interactions, π^* and σ^* combinations are formed. Due to the closer vanadium-vanadium distance in the binary vanadium oxides, the resulting bands are broader as compared to the case of the $VOPO_4$ phases.

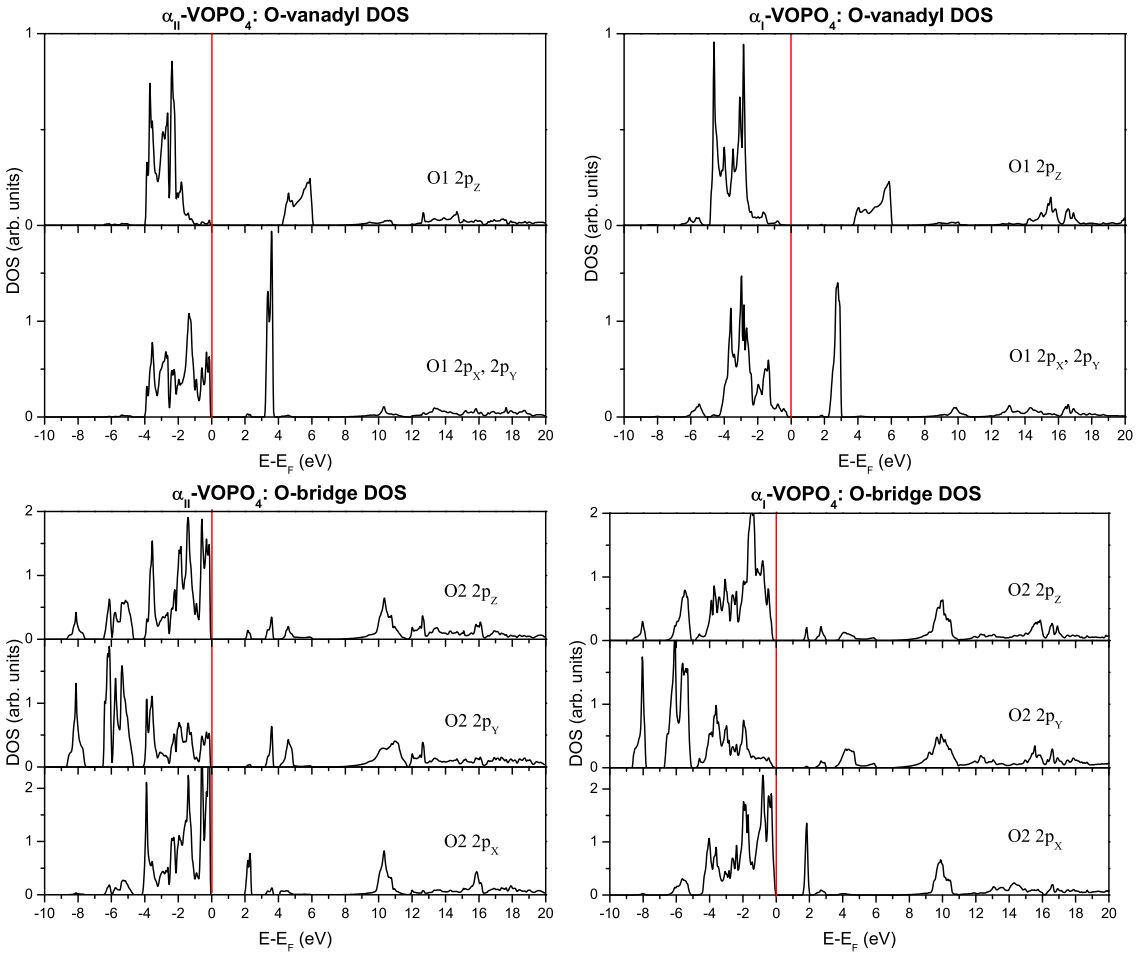

Fig. 5.28: α_{II}- and α_I-VOPO$_4$: vanadyl and bridge oxygen $2p$ projected DOS. For comparison of the different contributions, the scaling of the y axis is given.

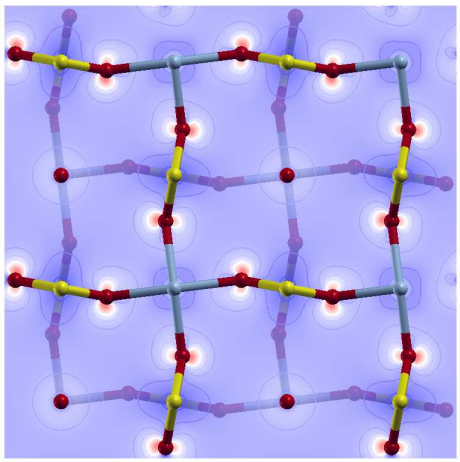

Fig. 5.29: Difference electron density in the plane of the equatorial oxygens of α_I-$VOPO_4$ plotted in the range between -0.7 (blue color) and 0.7 e/Å^3 (red). It shows the location of the lone pair at the O2 atom. The electrons are localized in a state corresponding mainly to a $2p_x$ orbital, as can also be seen in the projected O2 DOS.

ELNES and the contributions of different oxygens

In case of the α_{II}- and α_I-$VOPO_4$ phases, the two differently coordinated oxygens have very distinct contributions to the density of unoccupied states. Transitions into these states are measured when an oxygen K ionization edge is recorded. Consequently the two different oxygens contribute differently to the total shape of the ionization edge, as can be seen in Fig. 5.30.

The vanadyl oxygen is only involved in bond formation with vanadium and therefore contributes mainly to the unoccupied DOS within the first 6 eV above the Fermi-level. This is the region where the vandyl oxygen (O1) has the highest spectral weight. Bridging oxygens (O2), on the other hand, form a relatively strong covalent bond with a phosphorus atom and additionally interact with vanadium. As a result, they are mainly responsible for the feature starting about 8 eV after the edge onset, although, due to the interaction with vanadium, they also contribute to the first feature in the spectrum. Due to the higher symmetry of the PO_4 tetrahedra in the α phases, the peak at around 10 eV is narrower as compared to the one in the β phase (see also Fig. 5.12).

EELS measurements were performed in the energy region of the V $L_{2,3}$ and the oxygen K ionization edges. The recorded spectra are presented in Fig. 5.31 and 5.32 after back-

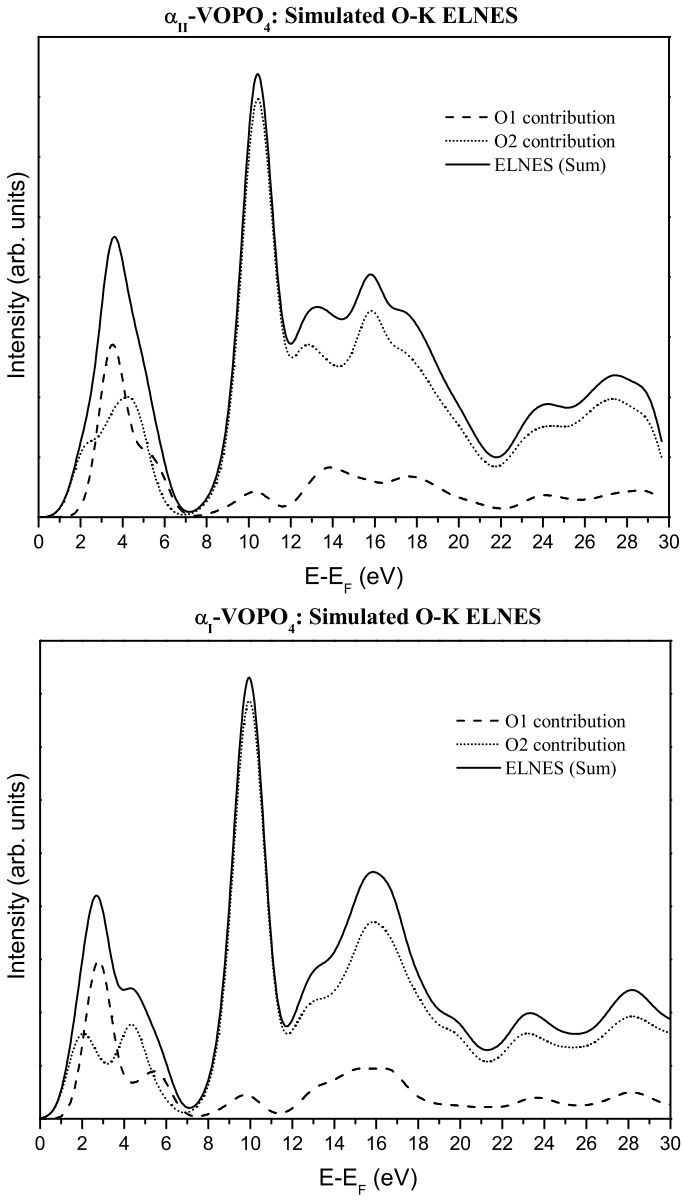

Fig. 5.30: O1 and O2 contributions to the ELNES of α_{II}- and α_I-VOPO$_4$.

ground subtraction and multiple scattering correction [44]. The V $L_{2,3}$ ionization edges are very narrow and appear at about 525.7 and 519 eV, respectively. From their position the oxidation state of vanadium can be estimated as +5 in both cases [81]. The two shoulders that are visible in the rising slope of the L_3 edge of α_{II}- and α_I-$VOPO_4$ appear at different energy as compared to those observed in the case of the β phase. This is an indication for differences in the crystal field splitting in the α- and β-$VOPO_4$ phases. Comparison between the simulated and measured oxygen K ionization edge demonstrates a reasonable agreement in the overall spectral shape, although the agreement in the case of α_{II} is not as good as expected. The disagreement is related to (i) difficulties in the preparation of phase pure samples, (ii) to the limited stability of the samples and (iii) to the high beam sensitivity of the samples. Therefore, both experimental spectra might contain some artifacts due to phase admixture and beam damage.

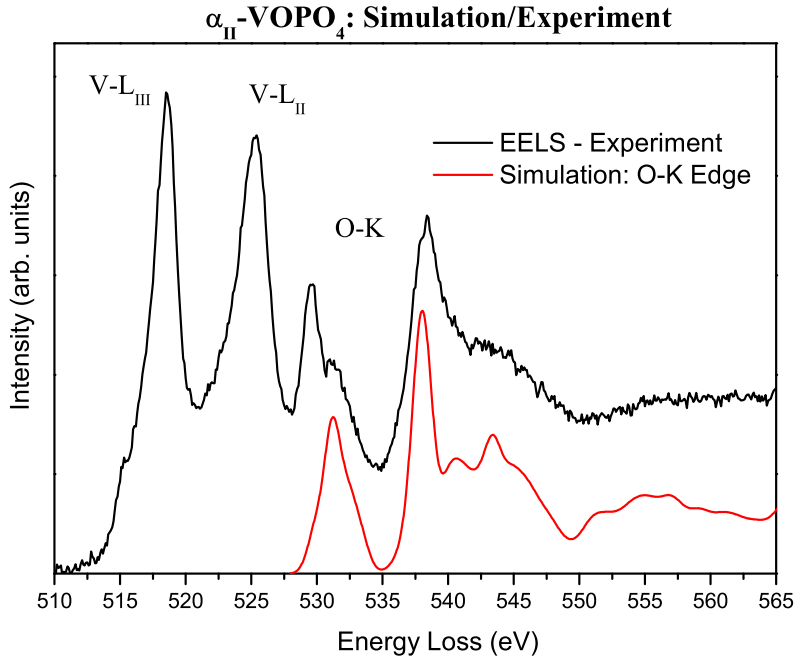

Fig. 5.31: EELS spectra of α_{II}-$VOPO_4$ and simulated oxygen K ionization edge.

5.4 Total energy and stability of the phases

The α_I-, α_{II}- and β-$VOPO_4$ polymorph are set up of similar basic structural units. This units share common corners leading to a three dimensional structure that is determined

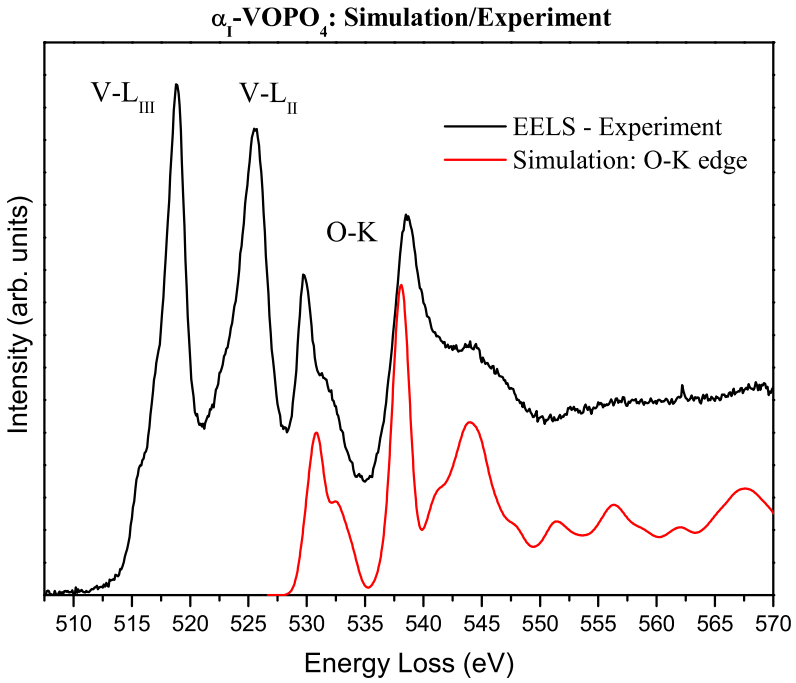

Fig. 5.32: EELS spectra of α_I-$VOPO_4$ and simulated oxygen K ionization edge.

by the way how these units are linked to one another. The V-O-P bonds of the bridging oxygens allow for different orientations of the tetrahedra relative to the orientation of the pyramids. In the case of α_I- and α_{II}-$VOPO_4$ the resulting three dimensional structure consists of weakly interacting layers, whereas a three dimensional network is formed in β-$VOPO_4$.

In order to get an insight on the benefits of certain linking geometries of building blocks with respect to the stability of a phase, the total energies were derived using a well tested and converged basis set. The results are presented in Fig. 5.33 and show that the total energy per atom of the investigated polymorph lies very close, with variations in the range of a vew mRy. Within the the accuracy of the present approach and the accuracy of the chosen basis set, there is no significant difference in the total energy of the three polymorph detectable.

The fact that the β phase is the thermodynamically most stable phase can therefore not be concluded from total energy calculations of the ground state at T = 0 K. Instead, thermodynamic effects have to be taken into account in combination with the observed dif-

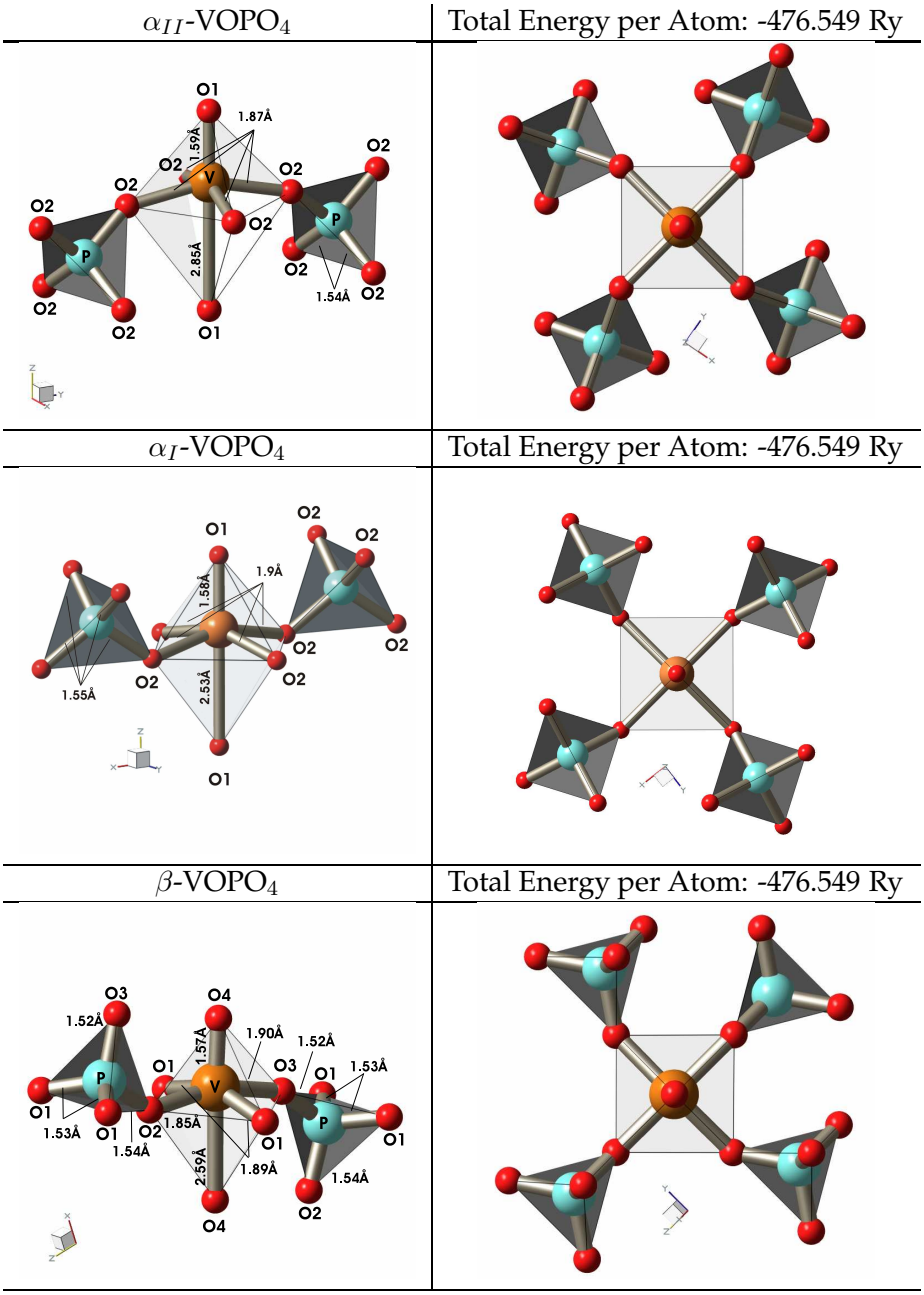

Fig. 5.33: Different arrangement of structural PO_4 and VO_5 units in α_{II}, α_I-$VOPO_4$ and β-$VOPO_4$ and the resulting total energy.

ferences in the geometry of the polymorph. The three dimensional structure of β-$VOPO_4$ exhibits a higher degree of interlacing as compared to the layered α-phases. This results in a lower structural flexibility of the β-phase. As a consequence, β-$VOPO_4$ offers a higher stability against hydration [73]. It is also related with the fact that both α-phases can be transformed into β-$VOPO_4$, but once arrived there, the structure is stuck and the transformation can not be reversed.

From the close agreement in the total energy of these phases (including the hypothetical $VOPO_4$ phase shown in Fig. 5.21) follows that the variation of the arrangements of building blocks has, within reasonable limits, only a small effect on the total energy. Small changes in the total energy resulting from a rearrangement can be balanced by accompanied slight changes in the geometry of the VO_5 pyramids and PO_4 tetrahedra themselves. This gives rise to the conclusion that, to a certain degree, these units can be considered as relatively independent building blocks.

5.5 Discussion

The results of simulations and the presented EELS spectra point out the close agreement between the electronic structure of the investigated polymorph. A detailed insight into bonding properties such as hybridization and covalent versus ionic bonding was gained from an inspection of the site and angular momentum projected density of states. The view of chemically independent PO_4 and VO_5 building blocks is justified by the fact that contributions to the density of states are well separated in energy for different bonds and by the different type of interactions (covalent versus ionic). An additional indication for relatively independent structural units is provided by the fact that the total energy as well as details in the electronic structure are mainly determined by the distortion and geometry of the VO_5 and PO_4 units whereas their relative arrangement is of minor influence. On the other hand it is the arrangement of these units that determines the three dimensional structure and properties such as phase stability and sensitivity toward hydration.

In the layer compounds, PO_4 units are connect to four VO_5 pyramids within a plane, and the only interaction between the planes is defined by a weak van der Waals interaction between the vanadium centers and the distant vanadyl oxygens of the next layer.

It is therefore the three dimensional network formed by the interconnection of PO_4 and VO_5 units in β-$VOPO_4$ that gives rise to its greater stability and the fact that the transformation from the layer $VOPO_4$ phases into β-$VOPO_4$ is irreversible.

In view of catalysis, the greater stability might also explain the lower activity of β-$VOPO_4$ as compared to the layered $VOPO_4$ phases [88]. The greater stability of the β- phase also accounts for a loss of catalytic performance for butane oxidation with the presence of β-$VOPO_4$ in used or inactive catalysts as reported by Bordes *et al.* [89] and Centi *et al.* [40, 89].

The close structural relation between the two α- phases suggests a degree of freedom in the position of the vanadium atom in the layered phases since the transformation of one phase into the other is easily achieved by shifting the vanadium atom along the (001) direction. On a local scale, such a transformation might be induced by a removal of vanadyl oxygen in the surface layer in a manner similar to the one reported by Ganduglia-Pirovano *et al.* [90] for the case of V_2O_5. Theoretical investigations on the formation of oxygen vacancies at the (001) surface of V_2O_5 revealed that the reduction of the surface, which is accompanied by the creation of reduced V centers, leads to structure relaxations resulting in the formation of V-O-V bonds between the layers of the α-V_2O_5 crystal. The vanadium atom thereby principally shifts toward the vanadyl oxygen of the next layer. Such a mechanism might explain the higher redox rate and higher rates of diffusion of oxygen into the bulk structure in the layered $VOPO_4$ phases as reported by Srilaxmi *et al.* [88].

Chapter 6

Vanadium (IV) phosphorous oxide Phases

This chapter deals with the electronic and geometric structure of two V^{4+} phases. The aim of this chapter is to add systems with a different vanadium oxidation state to the discussion of the relation between geometric and electronic structure. All results presented within this section are solely based on theoretical investigations. Spin polarized calculation were performed in order to account for the unpaired electron residing in the lowest $3d$ state of each vanadium atom.

6.1 $VO(PO_3)_2$

Vanadyl metaphosphate, $VO(PO_3)_2$ contains vanadium in a 4+ oxidation state and consists of otherwise similar structural units as the $VOPO_4$ phases discussed in the previous chapter. It is obtained by calcination of $VO(H_2PO_4)_2$, which has been identified as an alternative potential precursor phase of vanadium phosphate catalysts. In contrast to the industrially used VPP catalyst, the $VO(PO_3)_2$ catalyst has a P/V ratio of 2. Catalytic testing of amorphous as well as partly crystalline $VO(PO_3)_2$ catalysts revealed a specific rate per area of MA formation in the *n*-butane oxidation comparable to that of VPP, although the MA selectivity is lower for $VO(PO_3)_2$ [91,92].

6.1.1 Geometric Structure

$VO(PO_3)_2$ crystallizes in the monoclinic space group C^6_{2h} $C12/c1$. The structure is set up by chains of distorted VO_6 octahedra which are separated from each other by pairs of PO_4 tetrahedra. The VO_6 chains are running along the z - direction and are linked to the PO_4 tetrahedra by sharing common corners via the bridging oxygens. Corner sharing PO_4 tetrahedra (linear metaphosphate $(PO_3)_2$ groups) form zick-zack rows which are embedded between four VO_6 chains (see Fig 6.1). Their common corners are defined by the phosphate oxygen atoms. In total, there exist three different types of oxygens in $VO(PO_3)_2$. Bridging oxygens O1 and O2 set up the four corners defining the equatorial plane of the VO_6 octahedra. They form bonds to one vanadium and one phosphorus atom at slightly different bonding distances and P-O-V angles of 142.0 ° and 158.6 °, respectively. Vanadyl oxygens, O3, are only bond to vanadium and define the axes of the octahedra. They form a short V=O double bond of 1.64 Å and an additional weak interaction with the vanadium atom of the next octahedra at a distance of 2.56 Å. Due to this weak interaction, the picture of a distorted pyramidal surrounding is used in the discussion of the local environment of the vanadium atoms. The third kind of oxygen atoms are the phosphate oxygen atoms (O4) which form only bonds with two phosphorus atoms. The primitive cell comprises four formula units.

The local environment of the vanadium atoms in $VO(PO_3)_2$ is similar to the one present in α_{II}-$VOPO_4$, as can be seen in Fig. 6.2. In both compounds, the PO_4 units connected to the plane of the VO_5 pyramids are tilted downwards with respect to the orientation of the pyramids. The close agreement in the local surrounding of the vanadium atoms allows to study the effect of a varying vanadium oxidation state on the electronic structure. Another motivational aspect for the investigation of $VO(PO_3)_2$ is the presence of corner sharing PO_4 units. They contain the phosphate oxygen atoms that are only bond to two phosphorus atoms (P-O-P) and thereby add a new type of oxygen to the discussion.

6.1.2 Electronic structure

Electron density

Electron density plots calculated for a plane intersecting the V=O bonds are shown in Fig. 6.3. The plots demonstrate how zig-zag chains of covalently bonded PO_4 units bridge the weak interaction between VO_5 pyramids of a chain. As a result, a three dimensional

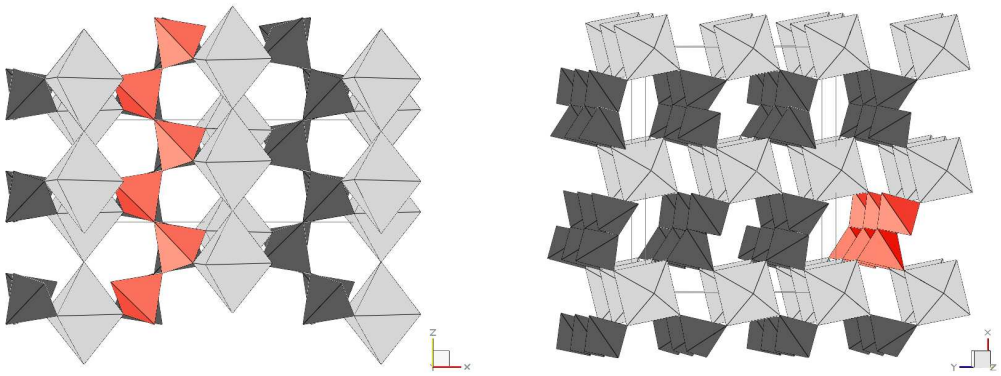

Fig. 6.1: Crystal structure of $VO(PO_3)_2$, viewed from the [010] and [001] direction, respectively. The unit cell of the orthorhombic representation used in the simulation is indicated; *a*, *b* and *c* are parallel to *x*, *y* and *z* axis, respectively. For clarity, groups of atoms are combined to VO_6 octahedra and PO_4 tetrahedra. In order to point out the interconnection of PO_4 units, one of the chains is highlighted.

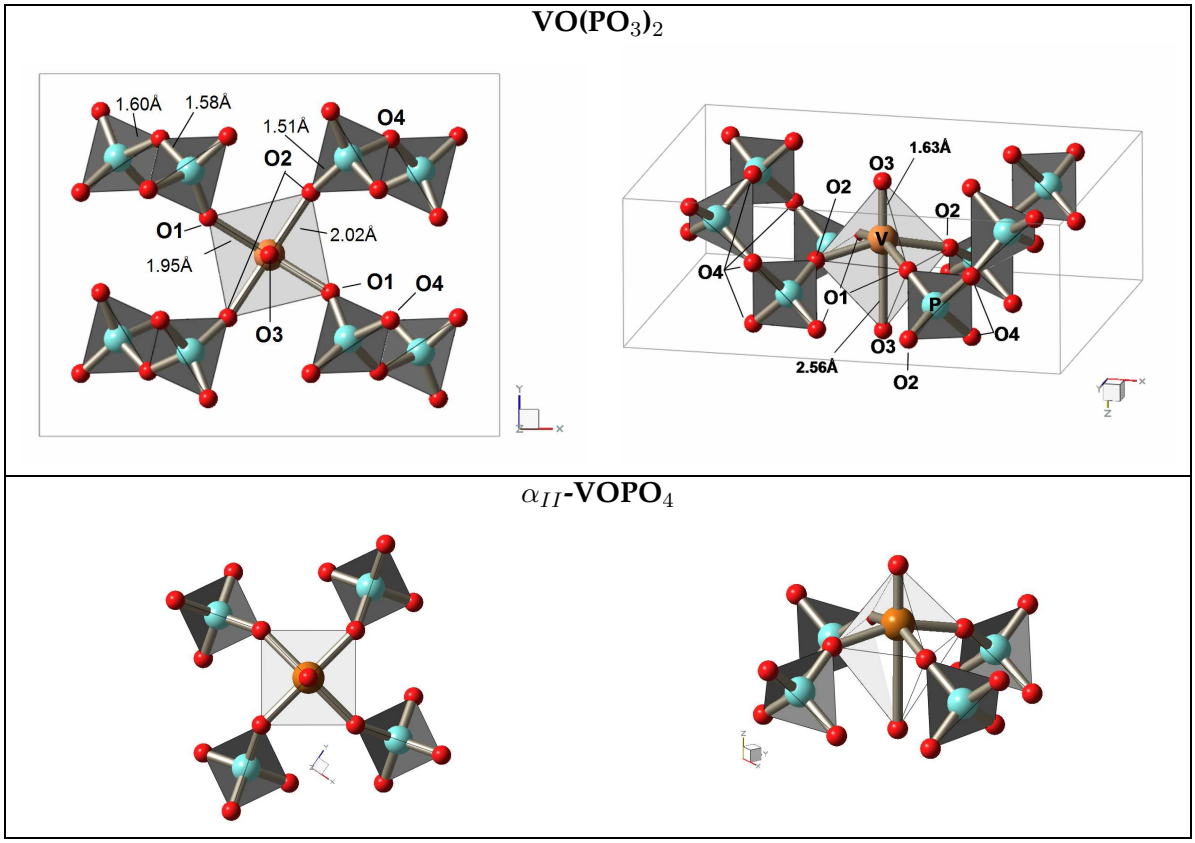

Fig. 6.2: Arrangement of the basic structural units in $VO(PO_3)_2$. To demonstrate the similarity, the arrangement is also given for the α_{II}-$VOPO_4$ phase.

network is formed. Apart from this, the local electron density distribution at the VO_5 units and along the VO_6 chains shows similarities with the one of α_{II}-$VOPO_4$.

Density of states

Total DOS

Compared to the V^{5+} phases discussed in the previous chapter, vanadyl metaphosphate contains one additional electron per vanadium site that is available for filling into the lowest empty states. This results in an upwards shift of the Fermi-level, as can be seen in the total DOS presented in Fig. 6.4. The atom projected DOS is presented in Fig. 6.5. The diagram reveals that the corresponding states appearing just below the Fermi-level are indeed localized at the vanadium sites. Each vanadium site being in a d^1 electronic configuration has a local spin of $1/2$. The richness of exchange pathways between these paramagnetic centers is responsible for a variety of magnetic interactions which are beyond the scope of the present investigations [93–95]. The results presented in this chapter are based on a spin-polarized calculation, resulting in a parallel alignment of the unpaired electron spins. The presence of an electron in a localized vanadium state effects the remaining unoccupied states, as can be seen in the up and down components of the DOS in Fig. 6.4. Apart from the shift of the Fermi-level, the overall DOS shows similarities with the cases discussed in the previous chapter. Oxygen states dominate the valence band between -18.5 and -2.7 eV and are followed by a narrow band of vanadium valence states. The remaining vanadium $3d$ states dominate the lower conduction band between 1 and 4 eV above the Fermi level. The upper conduction band starting at around 4.5 eV is dominated by combinations of oxygen and phosphorus states with some contribution from vanadium.

Projected DOS

The vanadium $3d$ projected DOS is presented in Fig. 6.7. It clearly demonstrates that the unpaired electron at the vanadium site occupies a state localized in the basal plane of the VO_5 pyramid. This state corresponds to an atomic like state, since it is only weakly overlapping with the $2p$ states of the surrounding atoms (see Fig. 6.6). Due to the local coordinate system used in the projection of the DOS, this isolated state is composed of mainly $3d_{x^2-y^2}$ with some admixture of $3d_{xy}$ character. The unpaired electron in the unhybridized HOMO state at the vanadium is suitable for radical reactions. Due to the

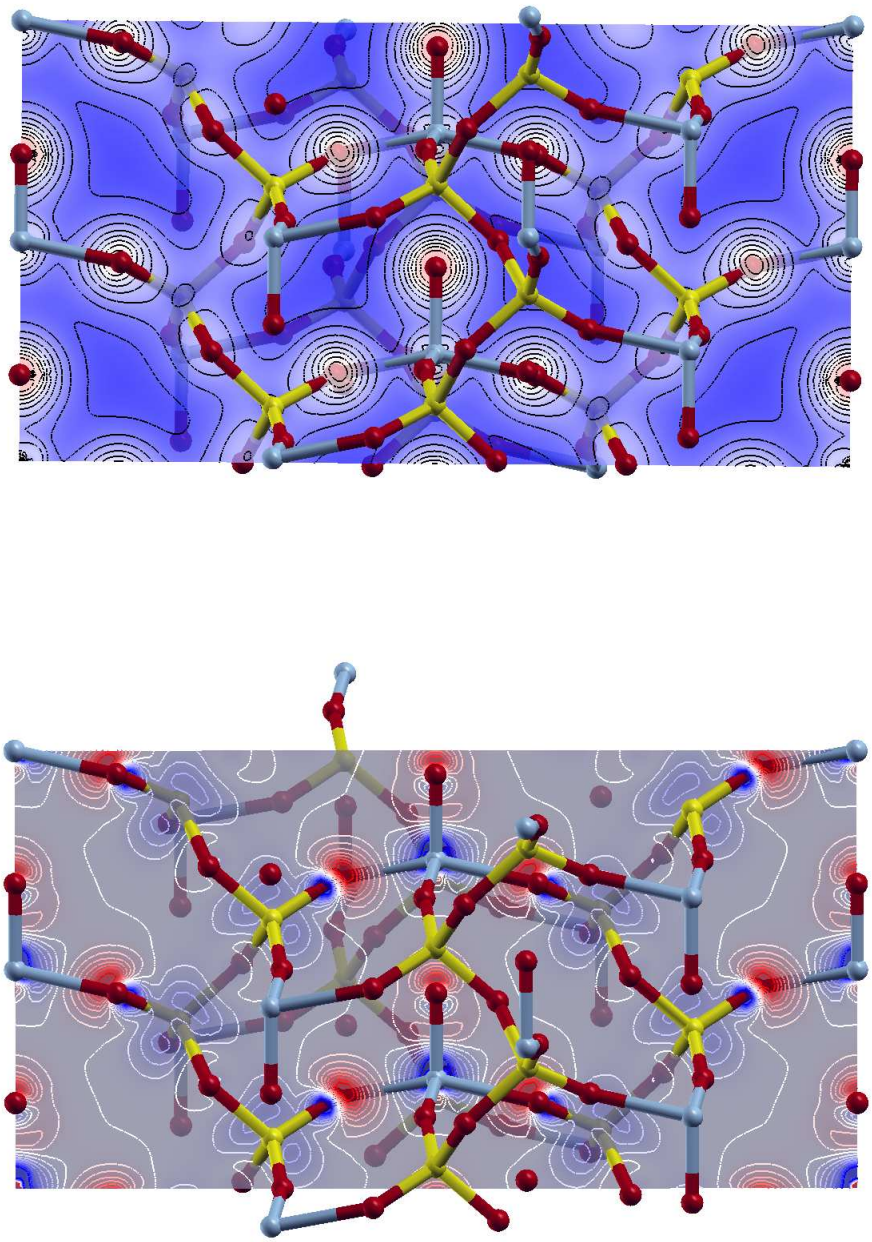

Fig. 6.3: Electron density plot of $VO(PO_3)_2$ given for a (110) plane intersecting V=O bonds. Fifteen contour levels are plotted in the range between 0 and 14 $e^-/Å^3$ on a square root scale. The difference density plot, showing the difference between converged crystalline electron density and a superposition of atomic densities is given in the range between -0.8 (blue color) and 0.8 $e^-/Å^3$ (red) with contour levels for each step of 0.1 $e^-/Å^3$.

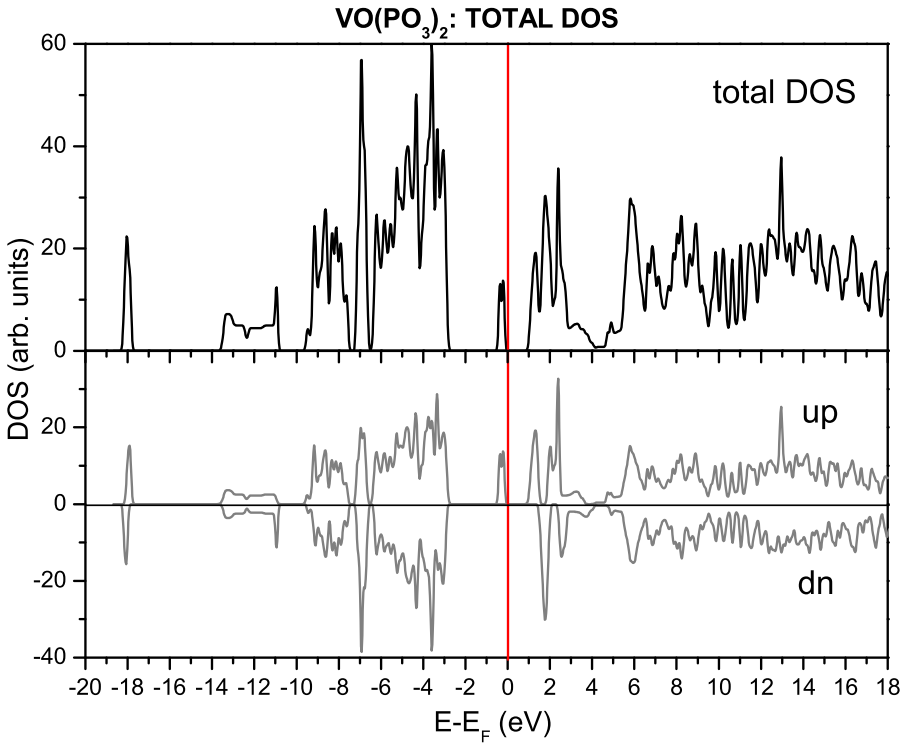

Fig. 6.4: Total DOS and the contributions from spin-up and spin-down to the DOS of $VO(PO_3)_2$ total DOS.

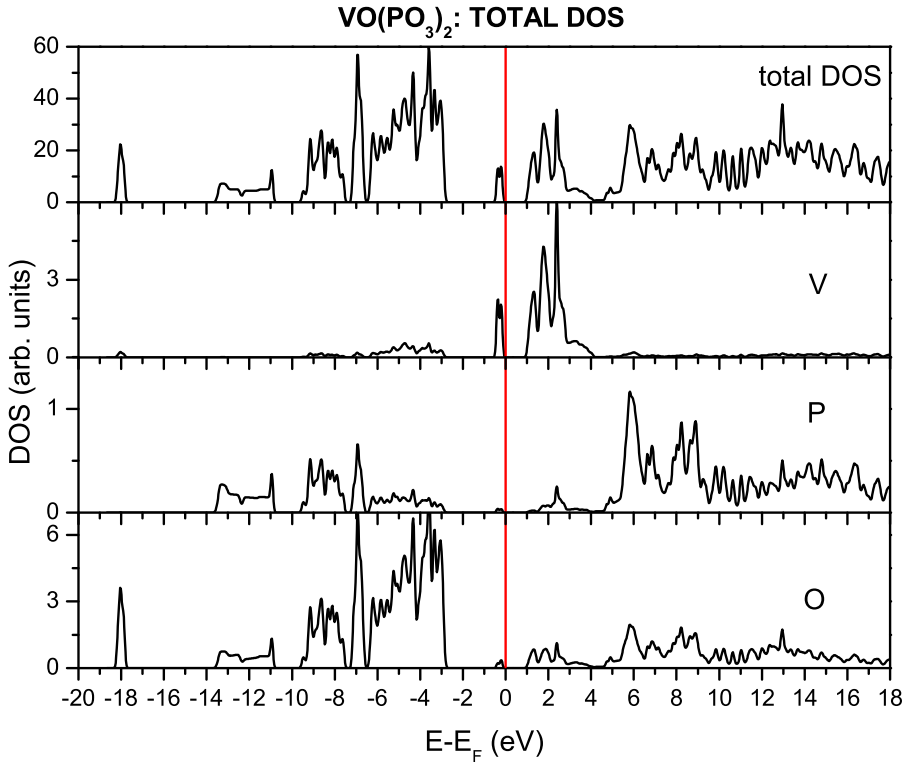

Fig. 6.5: Total DOS and the contributions of V, P and O to the DOS of $VO(PO_3)_2$. Note the different scaling for the intensities in the diagrams.

on-site exchange splitting between the filled and the empty $3d_{x^2-y^2}$ state, the latter is shifted upwards by about 2 eV. As a result, the $3d_{xz}$ and $3d_{yz}$ states become the lowest states in the conduction band. They form antibonding π^* combinations with the oxygen ligands and are followed at higher energy by the $3d_{z^2}$ and $3d_{xy}$ states which form σ^* combinations. Due to the local coordinate system, these states contain also some contribution from $3d_{x^2-y^2}$.

The phosphorus s, p and d projected DOS is displayed in Fig. 6.8. Contributions to the valence band appear in the energy region between -13.6 and -3 eV. Combinations of s and p states dominate the lower two blocks of bands while combinations of p and d states are found in the region between around -7.3 and -3 eV below the Fermi-level. Above the Fermi-level, some s-p combination contributes to the region that is otherwise dominated by antibonding vanadium $3d$ - oxygen $2p$ combinations. At higher energies, the DOS is dominated by antibonding combinations between phosphorus s, p, d and oxygen s, p states.

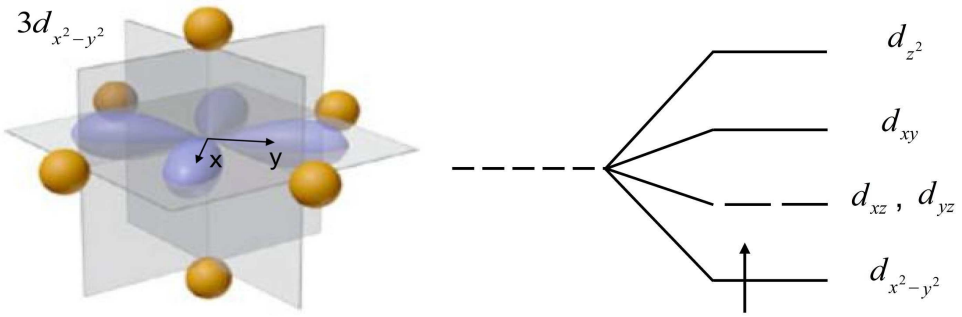

Fig. 6.6: Occupation of the lowest vanadium d state in $VO(PO_3)_2$ with one electron.

Differently coordinated Oxygens

Vanadyl metaphosphate contains three types of differently coordinated oxygens allowing for comparison and discussion. The presence of characteristic differences in the projected DOS is obvious, as shown in Fig. 6.9. The bridging oxygens O1 and O2 are bond to one phosphorus and one vanadium atom. Although their bonding geometry is slightly different, their contributions to the DOS is very similar. They contribute to the valence region of the DOS mainly between around -10 and -3 eV. Overlapping $2s$ and $2p$ contributions are found in the region between -13.7 and -6.5 of the DOS. These sp hybrids form bonds

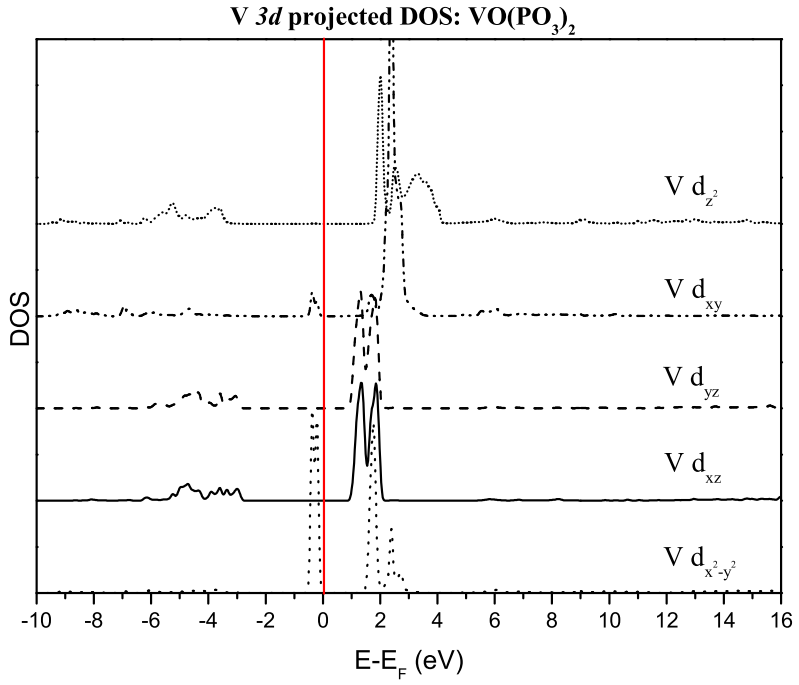

Fig. 6.7: Vanadium $3d$ projected DOS in $VO(PO_3)_2$. Spin up and down components are summed over.

with phosphorus $p-d$ dominated hybrids, as can be concluded from similarities with the phosphorus p and d projected DOS. States in the remaining part of the valence band arise from interaction with both, vanadium and phosphorus atoms. Vanadyl oxygens, O3, are interacting with vanadium, giving rise to the states appearing between -7.3 and around -2.8 eV in the valence region and between 1 and 4 eV in the conduction band. The features observed between 1 and 2 eV result from the formation of π^* antibonding states between vanadyl oxygen $2p_x$, $2p_y$ and vanadium $3d_{xz}$ and $3d_{xz}$ orbitals, while σ^* combinations are formed with the vanadium $3d_{z^2}$ states between 2 and 4 eV. As opposed to the bridging oxygens, the vanadyl oxygen $2s$ state remains well localized at around -18 eV below the Fermi-level. It interacts with a combination of a vanadium $4s$ and $4p_z$ state.

The phosphate oxygen O4 forms covalent bonds with two phosphorus atoms. These covalent interactions give rise to an additional block of valence bands appearing between -13.7 and -10.8 eV. The fact that O2 is only involved in the formation of bonds with phosphorus becomes evident from a comparison of the phosphorus s, p and d DOS with the O2 $2p$ DOS.

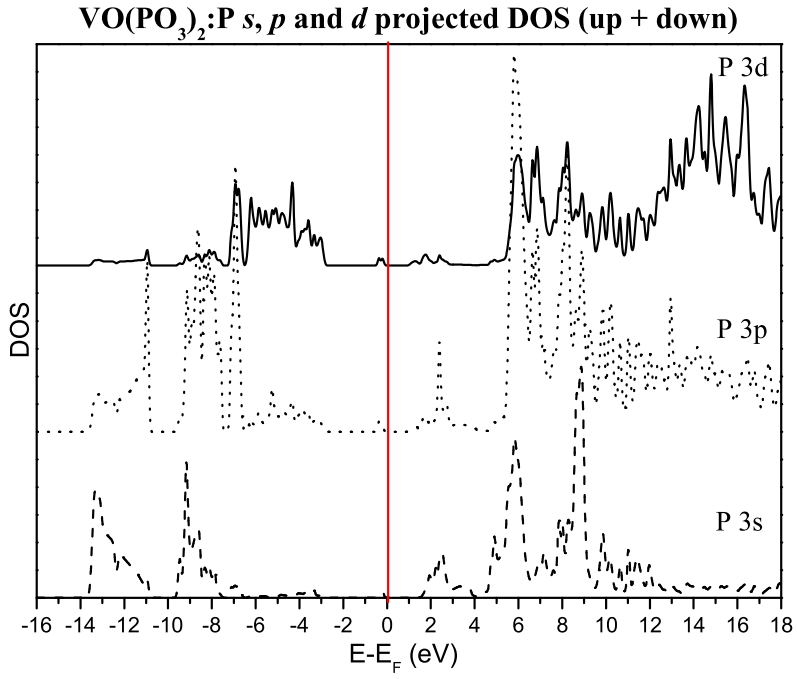

Fig. 6.8: Angular momentum projected DOS at the phosphorus site in $VO(PO_3)_2$. Spin up and down components are summed over.

ELNES and the contributions of different oxygens

The simulated oxygen K ionization edge and the contributions of the different oxygens to the total oxygen K edge is shown in Fig. 6.10. Due to the small energy separation between the unoccupied vanadium $3d$ states, the first peak does not show a distinct splitting. This can be explained to one part by the fact that the crystal field splitting in $VO(PO_3)_2$ is smaller due to a slightly lower distortion of the VO_5 pyramid and second, by the occupation of the lowest lying t_{2g} state with one electron. This does not only close one channel for the transition of the excited electron, but also shifts the empty counterpart of the half occupied state upwards in energy due to on site coulomb repulsion. As a result, only a slight shoulder is observed at the high energy side of the peak. This shoulder results from excitations of a vanadyl oxygen $1s$ state into a final state corresponding to oxygen $2p_z$ - vanadium $3d_{z^2}$ hybrid.At higher energies, in the region between 4 and 10 eV above the edge onset, a peak with a shoulder is observed. Intensity in this region is caused by transitions into empty antibonding states formed between oxygen and phosphorus. As shown in Fig. 6.10, this shoulder mainly arises from transitions at the phosphate oxygen O2. In case of the next feature, peaking at around 13 eV, a distinction of contributions is

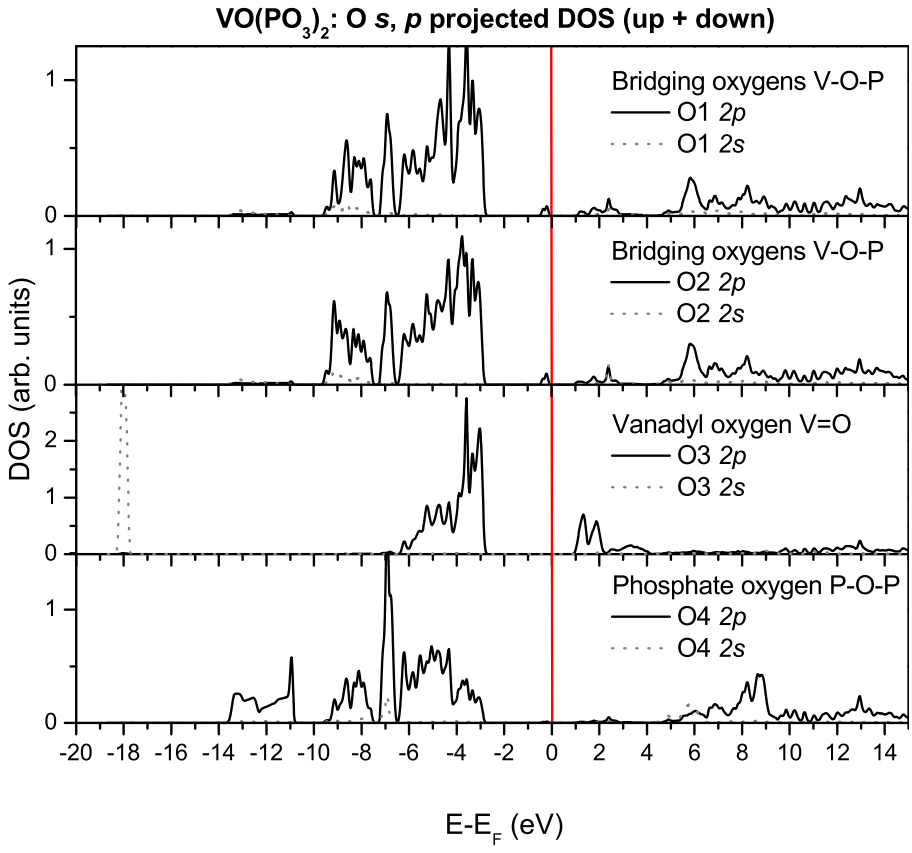

Fig. 6.9: Oxygen $2p$ projected DOS at different oxygen sites in $VO(PO_3)_2$. Note the different scaling for the intensities in the diagrams.

difficult, since all the oxygens contribute in a similar manner.

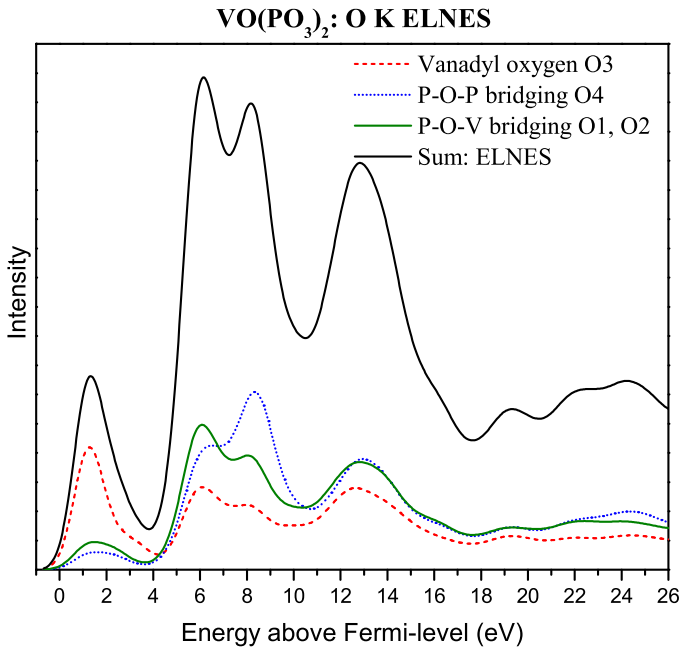

Fig. 6.10: Contribution of differently coordinated oxygens to the K edge of $VO(PO_3)_2$.

6.2 $VO(H_2PO_4)_2$

Vanadyl acid orthophospate, $VO(H_2PO_4)_2$, is used as a precursor for the $VO(PO_3)_2$ phase. During calcination, the structural water is lost and a rearrangement of VO_6 and PO_4 units takes place. Vanadyl acid orthophosphate is prepared using the reaction of V_2O_5 and H_3PO_4 or $VOPO_4{\cdot}2H_2O$ with an aldehyde or ketone as a reducing agent [84], or alternatively, by reduction of $VOPO_4$ phases with alcohols.

6.2.1 Geometric Structure

Vanadyl acid orthophosphate crystallizes in the tetragonal space group D_{4h}^8 $P4/ncc$ with a unit cell containing four formula units. The geometric structure is illustrated in Fig. 6.11. It consists of chains of distorted VO_6 octahedra that are stacked along the z-direction and separated from each other by PO_4 tetrahedra. Along the chains, the octahedra are alternately rotated along their octahedral axis by $\pm$ 9.12 °. Tetrahedra are made up of two oxygen atoms belonging to the equatorial plane of two individual octahedra and of two oxygen atoms that are saturated by hydrogen atoms. The structure contains three differently coordinated oxygen atoms, as shown in Fig. 6.12. Bridging oxygens, O1, form bonds to one vanadium and one phosphorus atom. They define the equatorial plane of the octahedra and two corners of each tetrahedra. The remaining two corners of the PO_4 tetrahedra are defined by the O2 atoms. These atoms form two bonds: one to a phosphorus and one to a hydrogen atom. From geometric considerations it seems plausible that these are the positions where structural water is removed in the calcination from $VO(H_2PO_4)_2$ towards $VO(PO_3)_2$. Two hydrogen atoms and one oxygen atom are released when the connection of PO_4 units along O2 corners is formed. Finally, vanadyl oxygen, O3, define the apex, along which the VO_6 octahedra are connected. They form a short V=O double bond of 1.60 Å and additionally interact faintly with the vanadium atom at a distance of 2.38 Å . Due to this weak interaction, the discussion of the local environment of the vanadium atoms is again based on the viewpoint of a distorted pyramidal surrounding.

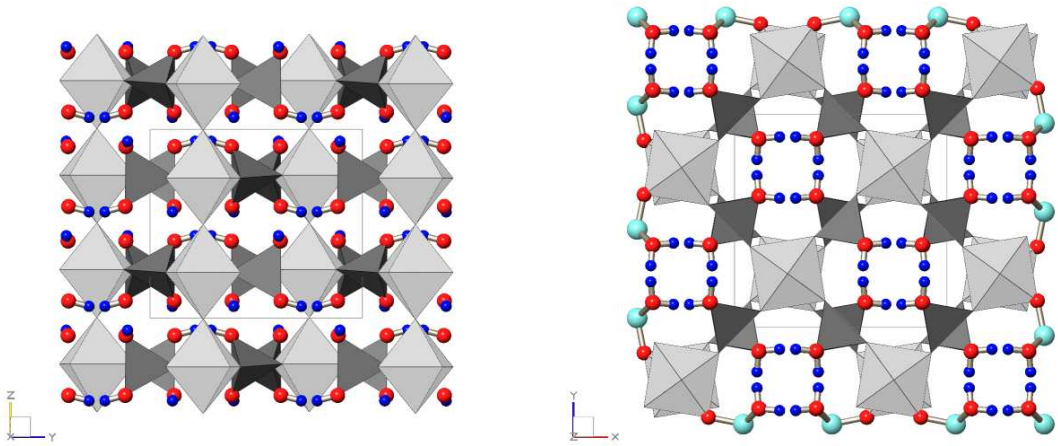

Fig. 6.11: Crystal structure of $VO(H_2PO_4)_2$ (ICSD number: 20182) viewed from [100] and [001] direction, respectively. The tetragonal unit cell is indicated and groups of atoms are combined to VO_6 octahedra (light gray) and PO_4 tetrahedra (dark gray) for clarity.

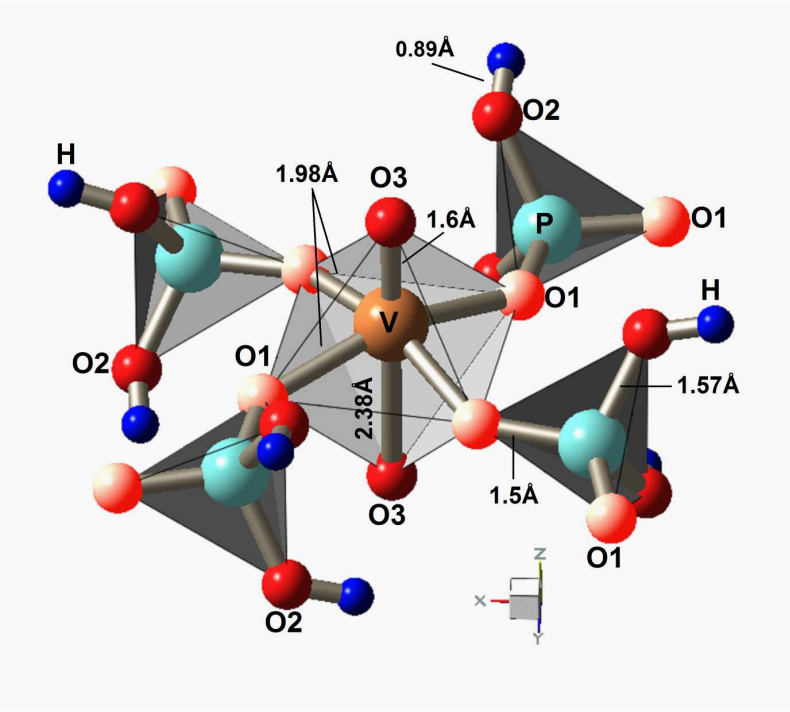

Fig. 6.12: Linking of the basic structural units in $VO(H_2PO_4)_2$

6.2.2 Electronic structure

Density of states

Total and atom projected DOS

The total DOS with spin-up and spin-down components and the atom projected DOS are presented in the figures 6.15 and 6.14, respectively. The overall DOS shows similarities with the DOS of $VO(PO_3)_2$ over the displayed energy range. Oxygen states dominate the valence band and form bonding combinations with hydrogen and phosphorus states. Vanadium states are mainly concentrated around the Fermi-level and show only a small admixture with oxygen states due to the mainly ionic type of interaction between the both. Since the general features have already been described in the preceding section, the discussion will be focused on the effect of the hydrogen atoms on the electronic DOS.

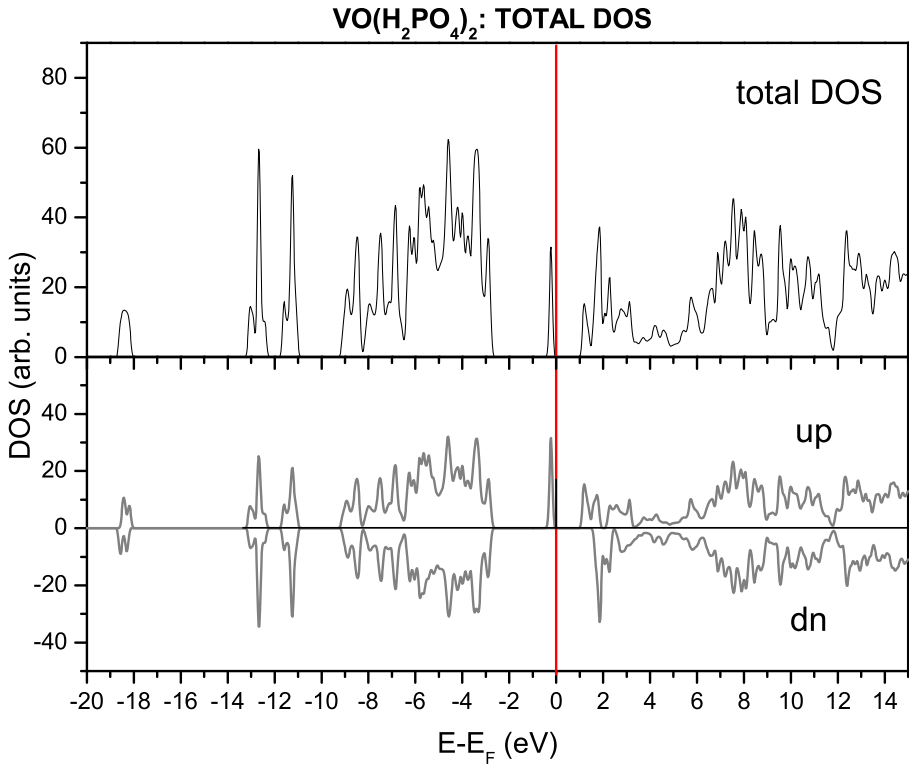

Fig. 6.13: Total DOS and the contributions from spin-up and spin-down to the DOS of $VO(H_2PO_4)_2$.

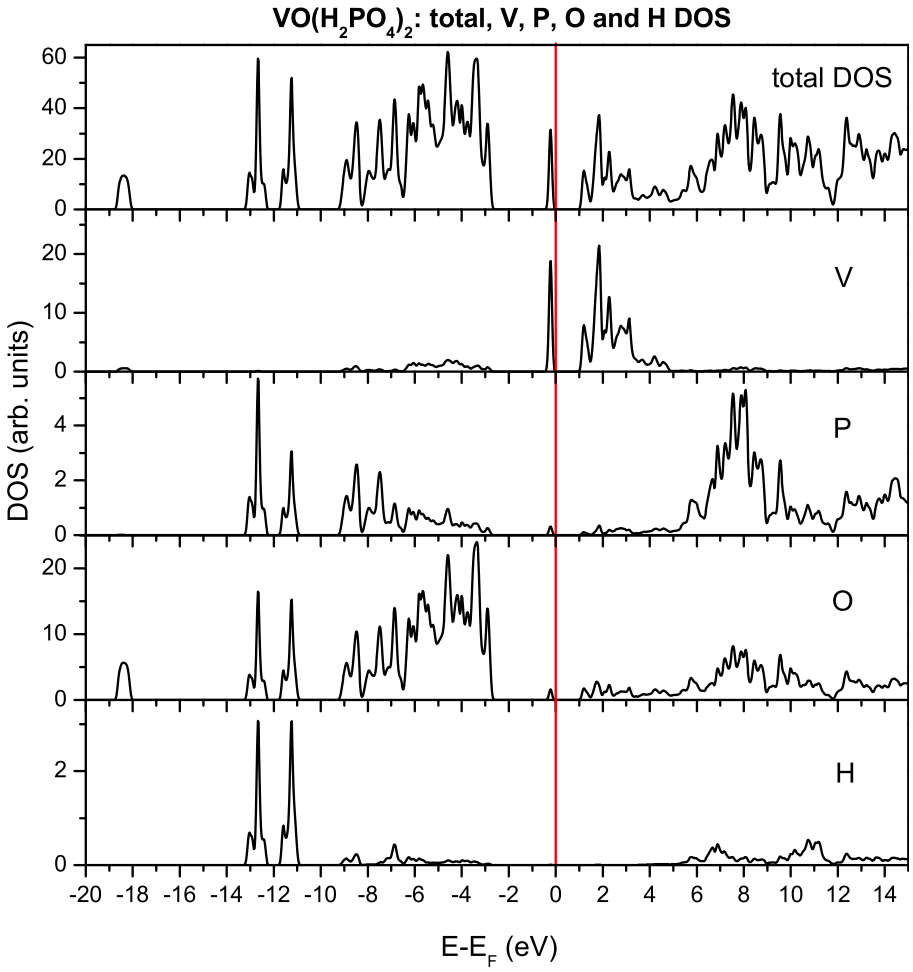

Fig. 6.14: Total DOS and the contributions of V, P, O and H to the DOS of $VO(H_2PO_4)_2$. Note the different scaling for the intensities in the diagrams.

Angular momentum projected DOS

The vanadium $3d$ projected DOS is presented in Fig. 6.15. Similarly to the case of vanadyl metaphosphate, the highest occupied state just below the Fermi-level corresponds to a state localized at the vanadium atom. Due to the choice of the local coordinate system used in the projection of the DOS onto vanadium atomic orbitals, this state corresponds to a $3d_{x^2-y^2}$ orbital. It points in between the oxygen ligands of the pyramidal plane and forms weak antibonding interactions with the ligand $2p$ orbitals. The empty counterpart of this state is shifted upwards by around 2 eV due to the on-site exchange splitting and appears above the Fermi-level. The remaining $3d$ projected states appear at energies the higher, the larger their overlap with the ligand $2p$ orbitals is, in accordance with the crystal field determined by the surrounding of the vanadium atom.

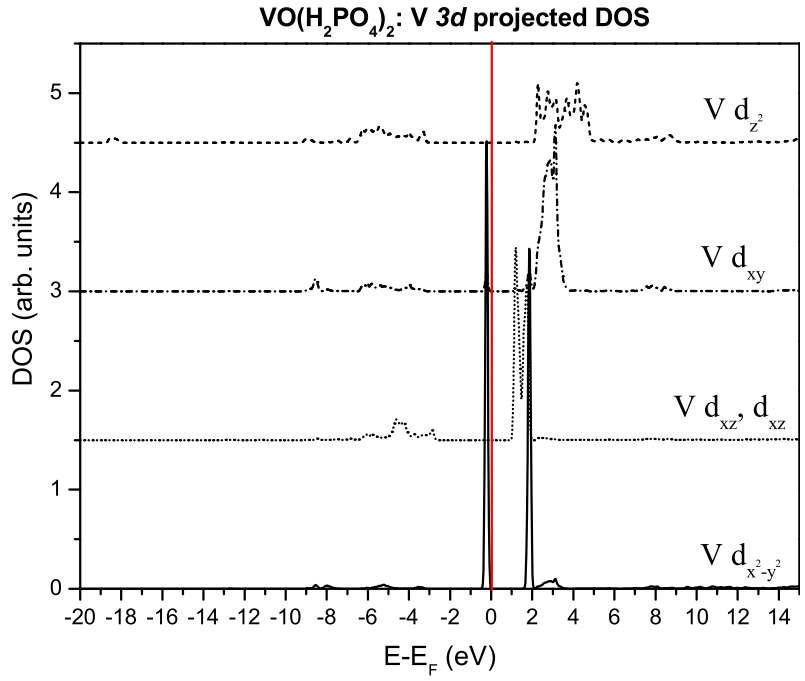

Fig. 6.15: Angular momentum projected DOS at the vanadium site in $VO(H_2PO_4)_2$. Spin up and down components are summed over.

The phosphorus s, p and d projected DOS is displayed in Fig. 6.16. The effect of the hydrogen atoms that are bond to the O2 atoms is clearly visible in the DOS. With respect to the phosphorus projected DOS of vanadium metaphosphate, the bands are more localized and a change of the shape and in the mixing of the s, p and d contributions is observed

in the valence band region. The main features observed in the phosphorus DOS are also present in the oxygen and hydrogen contributions to the DOS as can be seen in Fig. 6.14 and 6.17. In the lower valence band, phosphorus s, p and d states form spd hybrids between -13.3 and -12.2 eV and between around -9.2 and -8.2 eV for bond formation with hybrid orbitals of O2 and O1, respectively. On the other hand, states of nearly pure p character are observed in the phosphorus DOS between -11.7 and -10.9 eV and between -8.3 and -7.2. These states are mixed with p orbitals of O2 and O1, respectively.

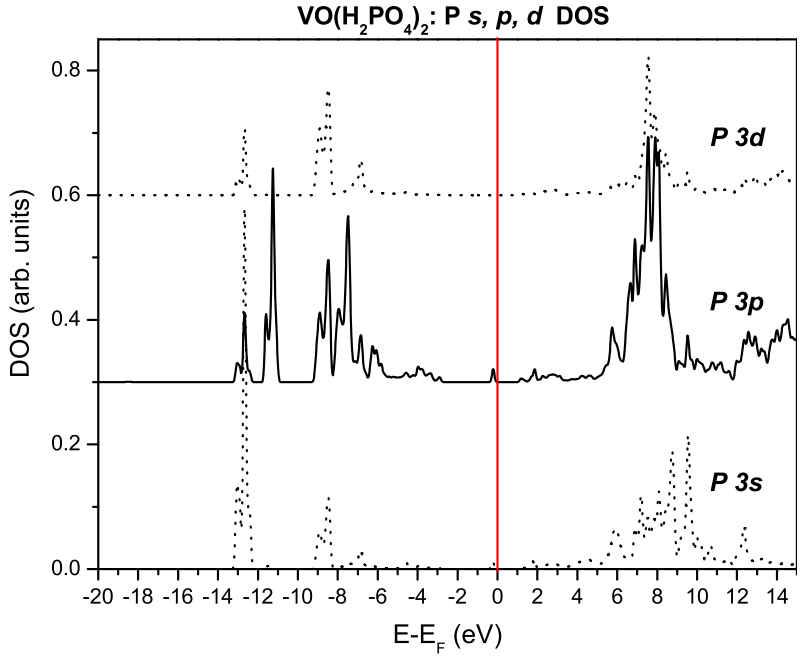

Fig. 6.16: Angular momentum projected DOS at the phosphorus site in $VO(H_2PO_4)_2$. Spin up and down components are summed over.

The figures 6.17 and 6.18 demonstrate that the energy levels of O2 $2p$ states are pulled down due to the bond formed with the hydrogen atom. As a consequence, the bond formed between O2 and the phosphorus atom also shifts downwards in energy. The atom projected DOS of O2 and H reveals the covalent character of the O2-H bonds, although some polarity follows from the different intensity of the common features observed in the range between -11 and -13 eV. The polarity of this bond is an indication for the acidity of the O2-H group. The DOS of the vanadyl oxygen, O3, shows a narrow s state localized between -19 and -18 eV. This state forms a bond with a vanadium $4s$ - $4p_z$ - $3d_{z^2}$ hybrid. Finally, the vanadyl oxygen $2p_z$ and the $2p_x$, $2p_y$ orbitals form σ^* and π^* combinations

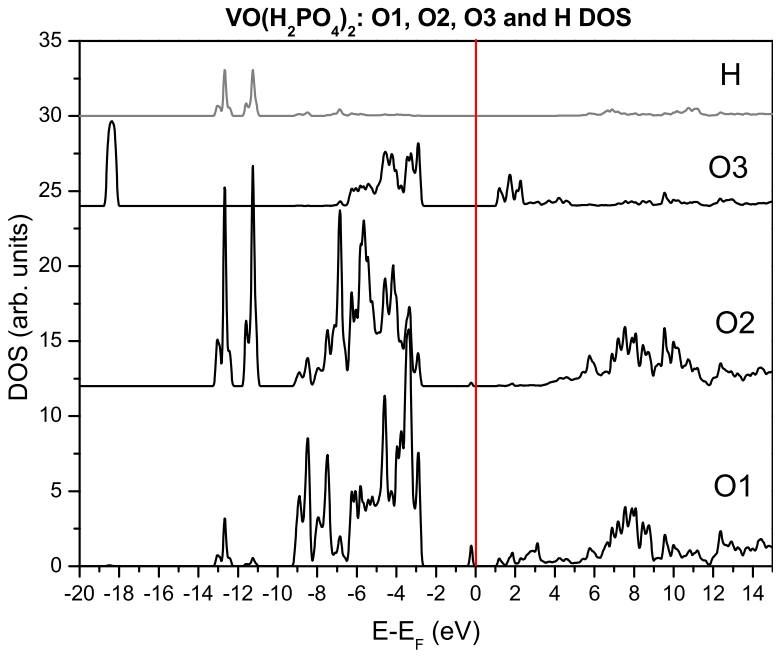

Fig. 6.17: Contribution of the hydrogen and the different oxygen atoms to the DOS of $VO(H_2PO_4)_2$.

with vanadium $3d$ states, respectively.

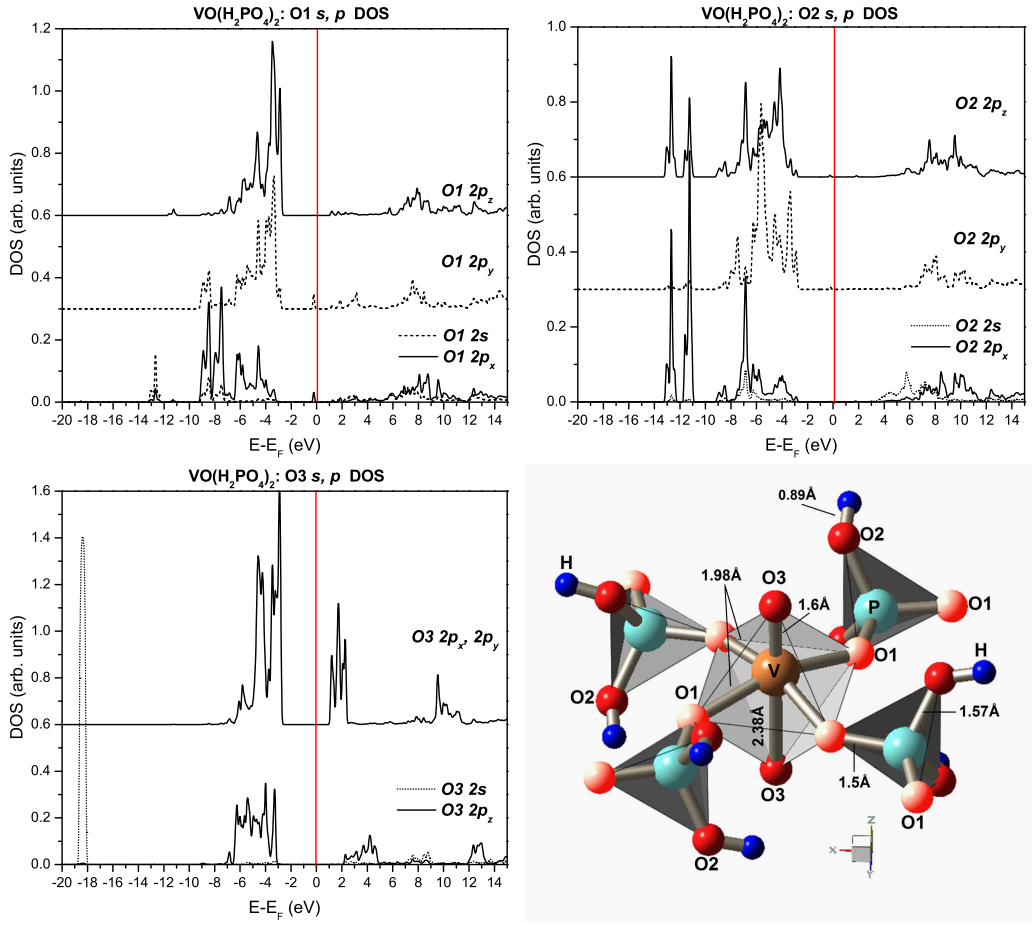

Fig. 6.18: Projected DOS at the bridging (O1 and O2) and vanadyl oxygen (O3) atoms of $VO(H_2PO_4)_2$.

ELNES and the contributions of different oxygens

The ELNES of the oxygen K edge and the contributions from the different oxygen atoms is presented in Fig. 6.19. The different coordination geometry is mirrored in the contributions of the different oxygen atoms to the ELNES. The vanadyl oxygen, O3 provides the main contribution to the first peak in the spectrum. It shows a clear splitting into the main π^* (t_{2g}) peak and a shoulder corresponding to σ^* (e_g) final states, in accordance with the crystal field splitting. At higher energies, above around 6 eV the vanadyl oxygen contributes with transitions into final states formed by overlap with vanadium $4spd$ hybrid states. In the lower energy region, the contribution of the bridging oxygen, O1, peaks at around 3 eV. This is the energy region corresponding to states localized in the basal plane of the VO_5 pyramid, in which the bridging oxygens are involved by a small mixing with the $3d_{xy}$ and the $3d_{x^2-y^2}$ states. At higher energy, transitions into antibonding states formed in the covalent interaction with phosphorus give rise to the peak at around 7.8 eV. The O2 shows no significant intensity in the low energy region, but instead, adds the shoulder to the main peak, due to empty antibonding combinations formed between O2 and the hydrogen atom.

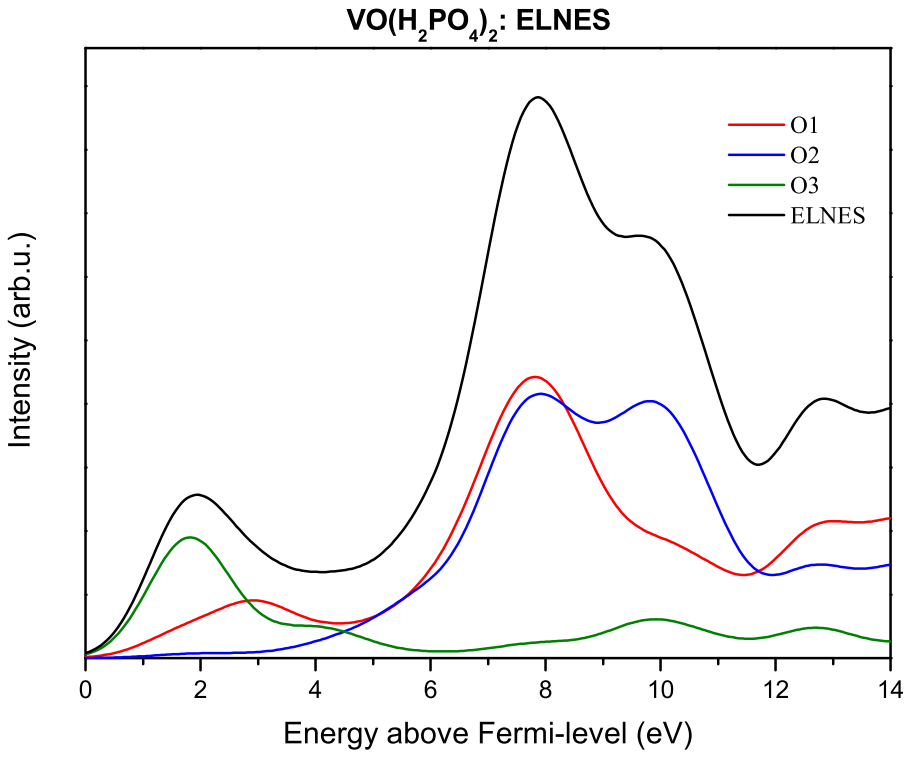

Fig. 6.19: Simulated oxygen K ELNES of $VO(H_2PO_4)_2$.

6.3 Discussion

In both compounds studied in this chapter, the vanadium - vanadium distance is relatively large, leading to very sharp and localized ("atomic like") vanadium $3d$ states. Due to the 4+ oxidation state of vanadium, one electron occupies the lowest lying $3d$ state. The calculations show that the resulting HOMO state is located in the basal plane of the VO_5 pyramid. As a result of the half occupation of the lowest lying $3d$ state, its empty counterpart is shifted upwards in energy by around 2 eV due to the on-site exchange splitting energy. Since the Fermi-level lies within the vanadium $3d$ states, the observed band gap is determined by the splitting of the lowest d state from the remaining $3d$ states and hence by the geometry of the VO_6 polyhedron. With respect to the previous chapters, two new types of oxygen atoms were introduced in this chapter: the P-O-P and the P-O-H bridging oxygen atoms. Their finger prints are clearly observable in the corresponding DOS and ELNES plots. A comparison of the intensity in the regions of the oxygen K ELNES that are characteristic for the O-V and the O-P dominated empty states, respectively, reveals a lower vanadium to phosphorus elemental ratio as compared to the V^{5+} phases (see Fig. 6.20). Additionally to the lower V/P ratio, the intensity in the region of the first few eV's of the O-K ELNES is reduced due to the shift of the Fermi-level with respect to the V^{5+} phases. In going from a 5+ to a 4+ oxidation state, the distortion of the VO_6 polyhedron is lowered, leading to an increase of the vanadium - vanadyl oxygen bond length. This is related with a slight reduction of the covalent character of the bond and hence, with a reduction of the oxygen $2p$ contribution to the unoccupied vanadium $3d$ dominated region of the DOS. The shape of the feature appearing in the EELS spectrum between around 3 and 10 eV (V^{4+} phases) and, respectively, between 6 and 12 eV (V^{5+} phases) is sensitive to the geometry and environment of the PO_4 units. While the $VOPO_4$ phases show a narrow peak, whose width is mainly determined by the distortion of the PO_4 unit, a double peak feature is observed in the V^{4+} phases. This is due to the fact that the oxygens of the PO_4 units have a different chemical environment in the latter case. Each peak of the double peak structure can be related to a different type of oxygen at the PO_4 unit: intensity at lower energy is mainly related to P-O-V bridging oxygen, whereas the second peak can be related to P-O-P and P-O-H oxygens in $VO(PO_3)_2$ and $VO(H_2PO_4)_2$, respectively.

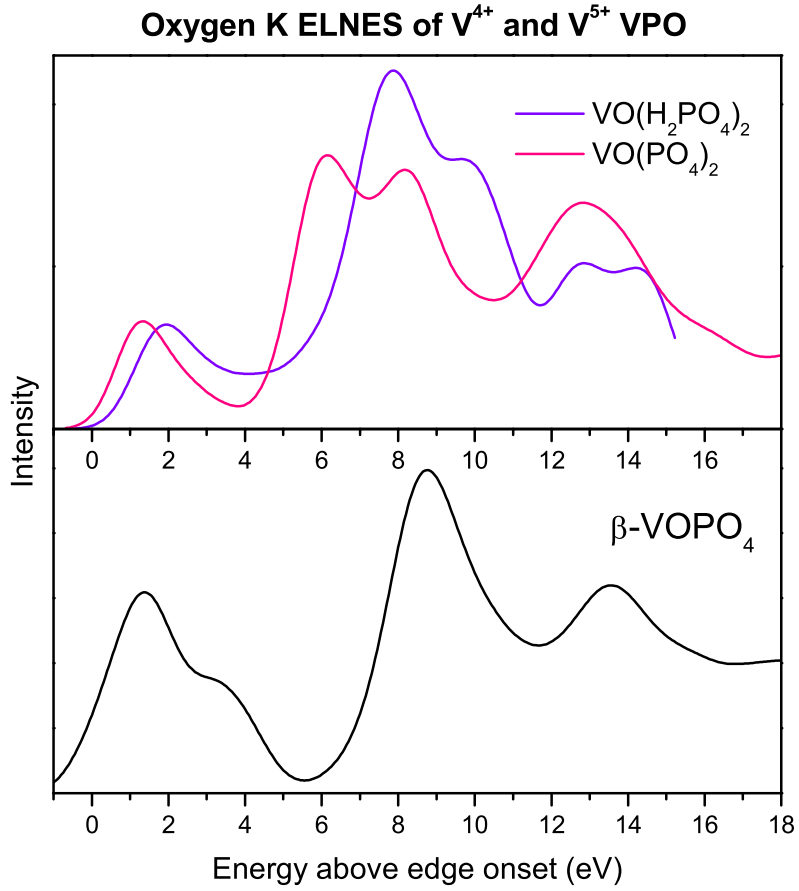

Fig. 6.20: Changes in the oxygen K ELNES from the precursor to the $VO(PO_3)_2$ phase. For comparison, the ELNES is also given for the V^{5+} β-$VOPO_4$ phase.

Chapter 7

Vanadium (III) phosphorous oxide

In this chapter, the electronic structure of a VPO_4 phase (VPP-36521) will be discussed. The aim of this chapter is to add another reference system for the discussion of the relation between electronic and geometric structure.

7.1 The electronic structure of VPO_4

7.1.1 Geometric Structure

The VPO_4 phase with the ICSD number 36521 will be discussed in the following. The structure was first described by Glaum *et al.* [96] and contains vanadium in a formal oxidation state of 3+. VPO_4 crystallizes in the orthorhombic space group D_{2h}^{17} CmCm. The structure is set up of rows of edge sharing VO_6 pyramids which are separated from each other by groups of PO_4 tetrahedra as shown in Fig. 7.1. The VO_6 pyramid is less distorted than in the previously discussed phases which is in agreement with the findings for binary vanadium oxides, where the distortion of the VO_6 octahedra decreases with decreasing oxidation state of vanadium [67]. The vanadium atom in the center of the octahedra forms two short bonds of 1.97 Å along the axial direction with oxygen O2 and four slightly longer bonds at 2.05 Å with the equatorial oxygens, O1. The octahedra are alternately tilted away from the y-axis toward the z-axis by $\pm$ 7.75 ° degrees. This allows for a pairwise interconnection of their apexes via PO_4 tetrahedra (see Fig.7.2). Apical oxygens therefore form bonds with one vanadium and one phosphorus atom at a V-O-P angle of 129.1 °. Equatorial oxygens, O1, are shared between two octahedra and one

tetrahedra by forming bonds with two vanadium atoms at a V-O-V angle of 100.1 ° and one bond with phosphorus at a V-O-P angle of 126.8 °. The PO_4 units present two longer (1.58 Å) and two shorter (1.53 Å) P-O bonds.

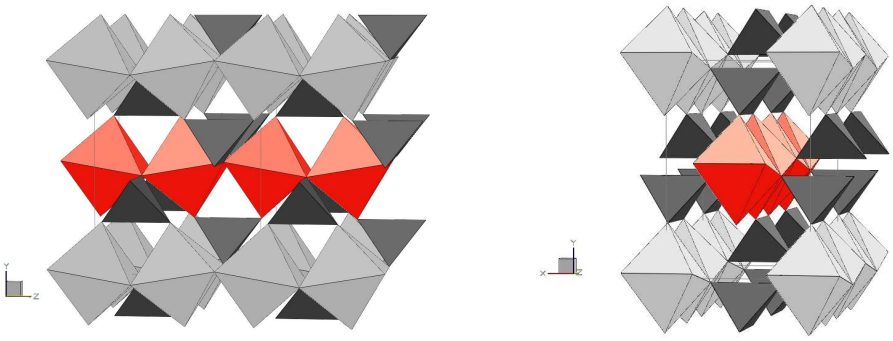

Fig. 7.1: Crystal structure of VPO_4 (VPP-36521) viewed from directions close to [100] and [010], respectively. The orthorhombic unit cell is indicated and groups of atoms are combined to VO_6 octahedra (light gray) and PO_4 tetrahedra (dark gray) for clarity. A chain of edge sharing octahedra is highlighted.

7.1.2 Electronic structure

Density of states

The magnetic structure of VPO_4 was determined by Glaum *et al.* [96]. They observed a strong 1-dimensional antiferromagnetic ordering along the chains of edge-sharing octahedra even at ambient temperatures. To a first approximation, a spin-polarized calculation was performed. The VPO_4 total DOS, including the spin-up and -down components is presented in Fig. 7.3. The effect of spin polarization is clearly visible in the block of bands intersecting the Fermi-level and in the empty states appearing between 2 to 4 eV above the Fermi-level. The calculation reveals a metallic state for VPO_4, as the DOS has a nonzero value at the Fermi level. As can be seen in the atom projected DOS shown in Fig. 7.4 these states correspond to partly filled vanadium states. The overall distribution of features in the DOS is, apart from the upwards shift of the Fermi-level, similar to the cases discussed in the previous chapters. A combination of oxygen and phosphorus bonding states dominates the lower valence band while their antibonding counterpart gives rise to the conduction band region starting above 4 eV. Only a small admixture with vanadium states is visible in the oxygen dominated region.

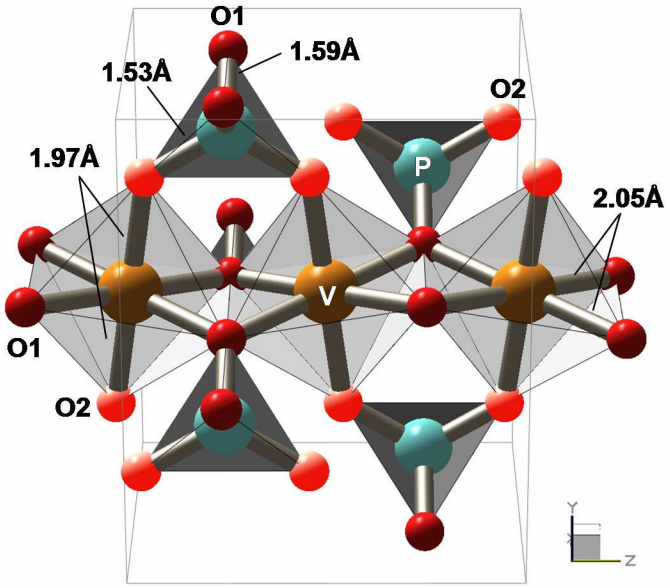

Fig. 7.2: Differently coordinated oxygens in VPO_4 (VPP-36521). The O1 atom is triply coordinated and forms two bonds with vanadium atoms and one bond with a phosphorus atom. The O2 atoms are forming one bond with vanadium, defining the short V-O axis and one bond with a phosphorus atom.

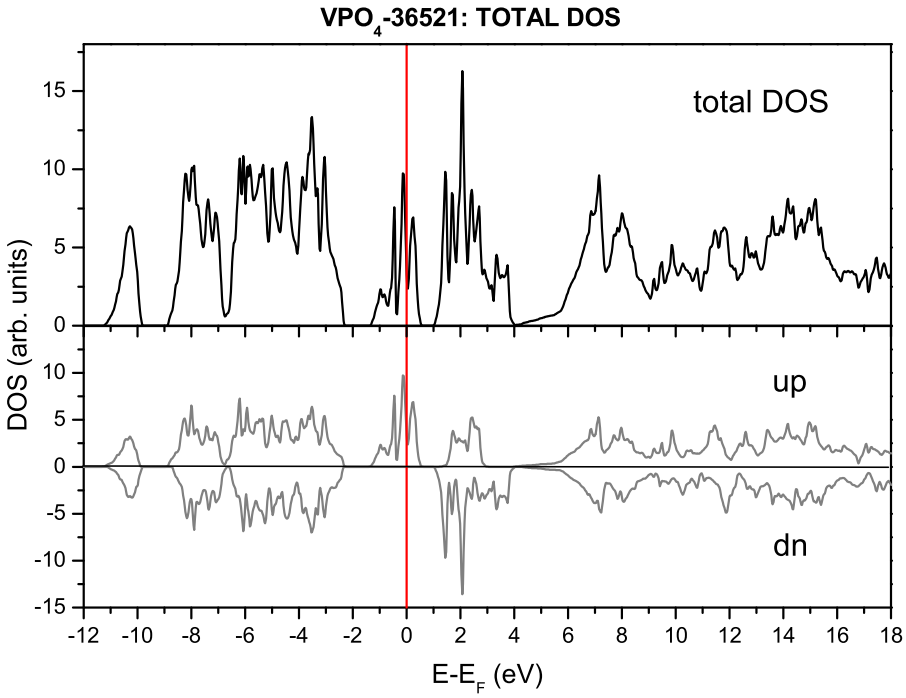

Fig. 7.3: Spin up and down components of the VPO_4 total DOS.

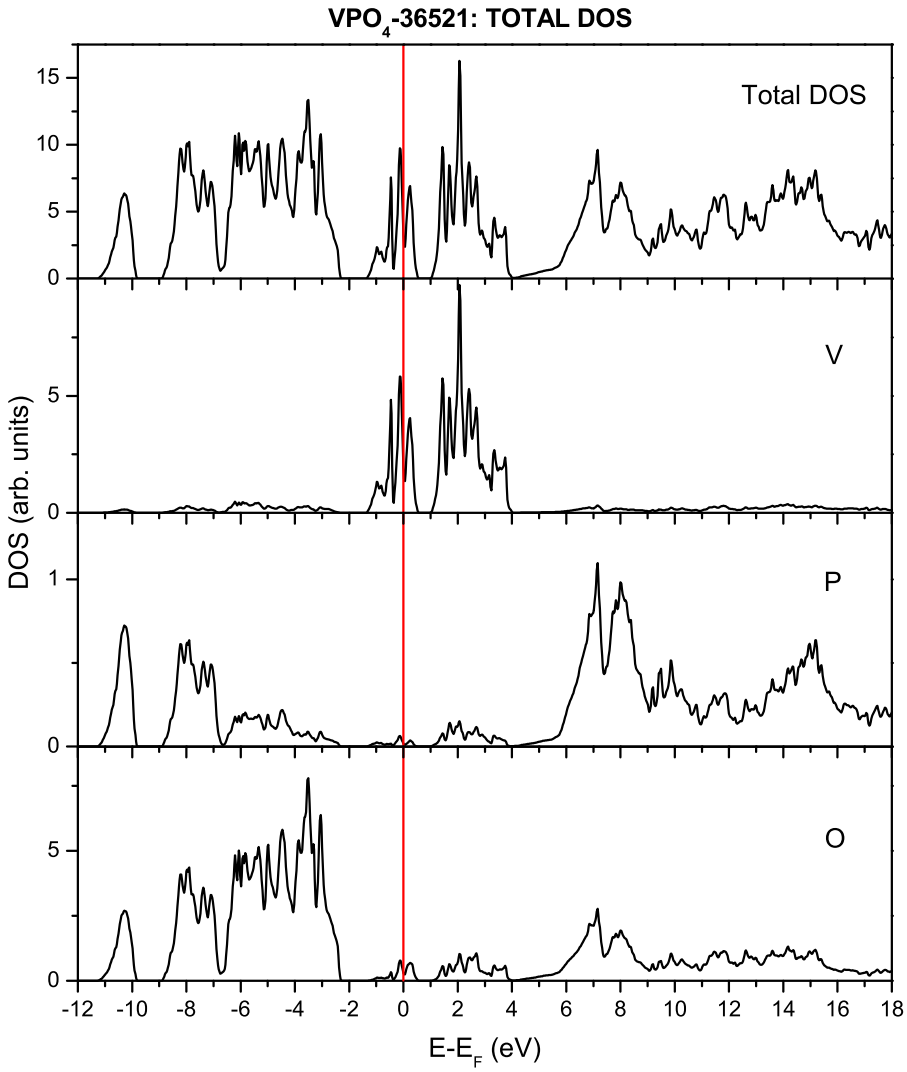

Fig. 7.4: Total DOS and the contributions of V, P and O to the DOS of VPO_4. Note the different scaling for the intensities in the diagrams.

Projected DOS

The vanadium d projected DOS is displayed in Fig. 7.5. In VPO_4, each vanadium atom has formally two electrons available for filling into its $3d$ states. A comparison of the total energy derived in a non spin polarized calculation with the total energy derived in a spin polarized calculation revealed a lower total energy and hence, a more favorable state for the latter. In a non spin polarized calculation, both electrons are filled into the lowest available vanadium $3d$ state, leading to a low spin state (see left graph in Fig. 7.6). In contrast, in a spin polarized calculation, the electrons are not paired but instead, filled into the two lowest available $3d$ states with their spins aligned parallel. This leads to a high spin state. Whilst in the first case, the two electrons have to share the same state, their mutual repulsion is lowered in the spin polarized case. This leads to a lower energy. The effect of spin polarization on the distribution of the vanadium $3d$ projected density of states becomes evident in Fig. 7.5. Due to the ligand field, the vanadium d states are split into two groups according to the close to octahedral symmetry of the vanadium surrounding. The t_{2g} states, forming π^* bonds with the oxygen ligands, and are found at lower energy. The e_g states, forming stronger interacting σ^* combinations with the ligands, appear at higher energies. Due to the larger distance between vanadium and the oxygens of the equatorial plane, antibonding states formed within this plane appear at lower energy as compared to states involving an interaction with the closer lying apical oxygen O2. As compared to $VO(PO_3)_2$, the vanadium-vanadium distance is smaller in VPO_4. As a consequence, the coupling of the unpaired electrons located at the V^{3+} sites is enhanced and the corresponding states become broadened.

The phosphorus s, p and d projected DOS is displayed in Fig. 7.7. The diagram shows similarities with the phosphorus DOS of the cases discussed in the previous chapters. Below the Fermi-level, a clear splitting into s, p and d dominated regions is observed, although a slight mixing between the states is present. Above the Fermi-level, overlapping s, p and d projections contribute to the DOS up to about 11 eV while combinations of p and d states prevail the s contribution above 11 eV.

Differently coordinated Oxygens

The oxygen $2s$ and $2p$ projected DOS at the O1 and O2 sites are presented in Fig. 7.8. Oxygen O1, which is bond to two vanadium and one phosphorus atom, forms a covalent bond with the phosphorus atom. Figure 7.8 reveals the formation of an sp hybrid from a

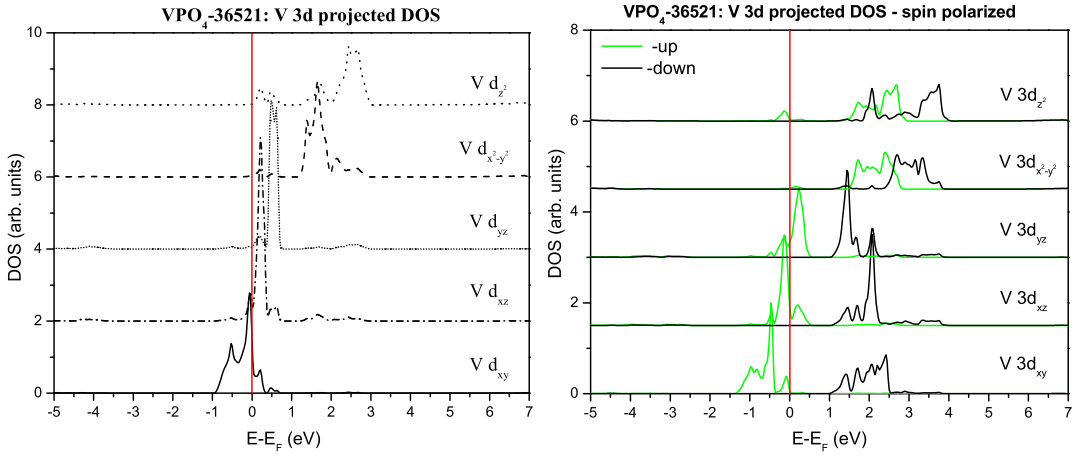

Fig. 7.5: Vanadium $3d$-projected DOS of VPO_4, as derived in a non spin polarized and in a spin polarized calculation. The resulting total energy is -530.869 and -530.885 Rh per atom, respectively. For the calculations, the local coordination system at the vanadium atom was oriented such that the z-axis coincides with the unit cell b axis (see Fig. 7.1).

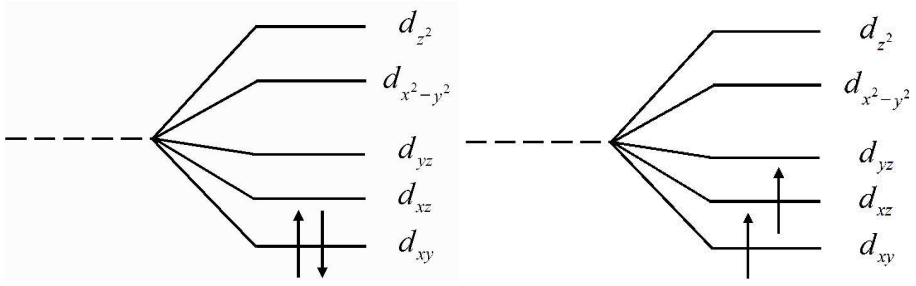

Fig. 7.6: Occupation of $3d$ states in VPO_4 without and with spin polarization.

combination of the $2s$ and a mixture of $2p_x$ and $2p_y$ projections. The portions of $2p_x$ and $2p_y$ contributions are in accordance to the the direction of the resulting covalent bond. The interaction with the two vanadium centers is of more ionic kind, as the electrons are mainly located at the oxygen, while the empty states are located at the vanadium. Only small covalent contributions to the bonding become evident from the mixing of O1 contributions to the otherwise vanadium dominated density of states. A π^* antibond is formed between the O1 $2p_y$ state and a vanadium state corresponding to a mixture of V $3d_{yz}$ and $3d_{xz}$ orbitals as indicated by common features in their projected DOS in the energy region between -0.5 and around 3eV. A σ^* combination between O1 $2p_z$ and V $3d_{xy}/3d_{x^2-y^2}$ states is visible in the range between -1.3 and 4 eV. Note that the local coordinate system at the vanadium atom is rotated with respect to the coordinate system of the unit cell. In the case of O2, the sp hybrid pointing toward the P atom lies in the y-z-plane. As a result, the $2p_y$, $2p_z$ and $2s$ states show common intensities in the DOS mainly between around -11.2 and -9.8 eV and between -8.8 and -6.8 eV. These are the regions in which the phosphorus $3s$ and $3p$ bands are located (see Fig. 7.7). The remaining $2p_x$ projected portion of the O2 DOS shows a dominant feature between around -2.3 and -4.2 eV below the Fermi-level, indicating the presence of a non bonding lone pair. At higher energies, antibonding σ^* combinations are formed between the $2p_y$ and the $3d_{z^2}$. Antibonding π^* combinations formed between O2 $2p_x$ and V $3d_{yz}$ states as well as between O2 $2p_z$ and the V $3d_{xz}$ states are found close to the Fermi-level. From the different bond length between oxygen and vanadium for O1 and O2 and the DOS it follows that the vanadium-oxygen bond with the twofold coordinated oxygen O2 is stronger than in the case of the triply coordinated O1.

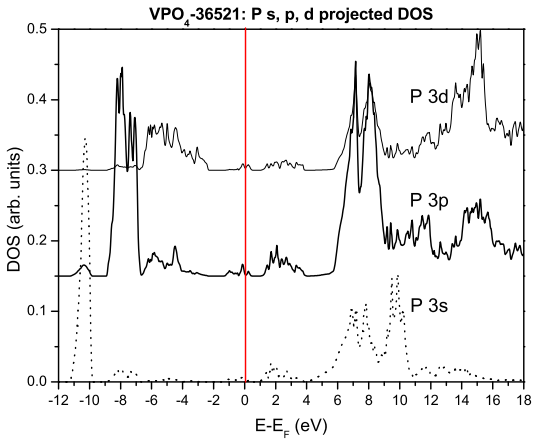

Fig. 7.7: Phosphorus s, p, d projected DOS of VPO_4.

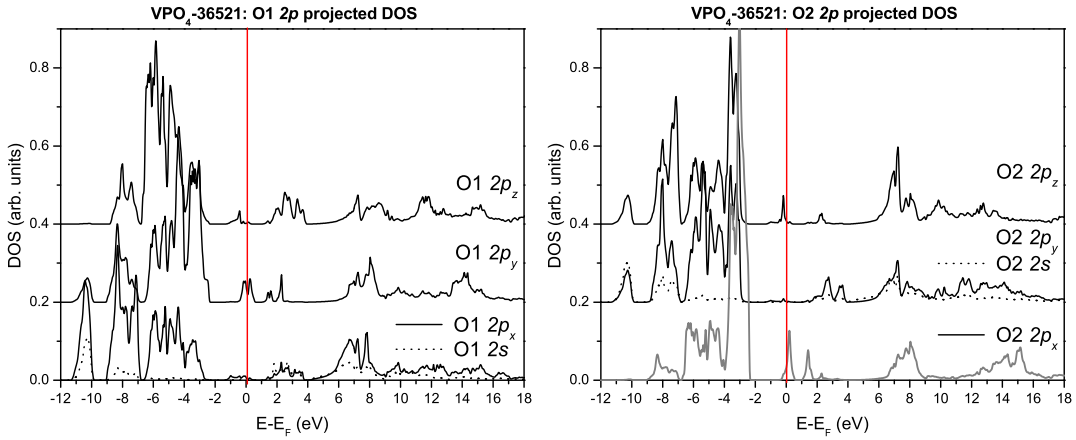

Fig. 7.8: Oxygen $2s$ and $2p$ projected DOS of VPO_4.

ELNES and the contributions of different oxygens

The simulated oxygen K ionization edge is presented in Fig. 7.9. Since both oxygens are coordinated by one phosphorus atom, their contribution to the ELNES region above 5 eV is similar. Intensity in this region derives from transitions into empty states formed mainly by interaction between oxygen and phosphorus. The situation is different in case of the first feature which is related to the empty states formed by antibonding combinations between oxygen $2p$ and vanadium $3d$ states. Contributions from O1 dominate this region because of its twofold coordination with vanadium. Only in the region of the first shoulder just above the edge onset, the spectral weight of O2 overwhelms the portion of O1. This is because the covalent contribution of O2 to the underlying states is bigger due to a shorter bonding distance to the vanadium atom as compared to O1. Nevertheless, this shoulder is much less developed as the corresponding feature observed in the V^{5+} phases. The lowering of its intensity is a direct consequence of the lower oxidation state of VPO_4. It results in a partial occupation of the low lying t_{2g} states, leaving only the empty remnants available as final states in the transition. The reduction of the vanadium oxidation state is also accompanied by a reduction of the distortion of the VO_6 octahedra, leading to an elongation of the vanadyl bond. This lowers the covalent oxygen $2p$ admixture to these states and hence the intensity of the feature.

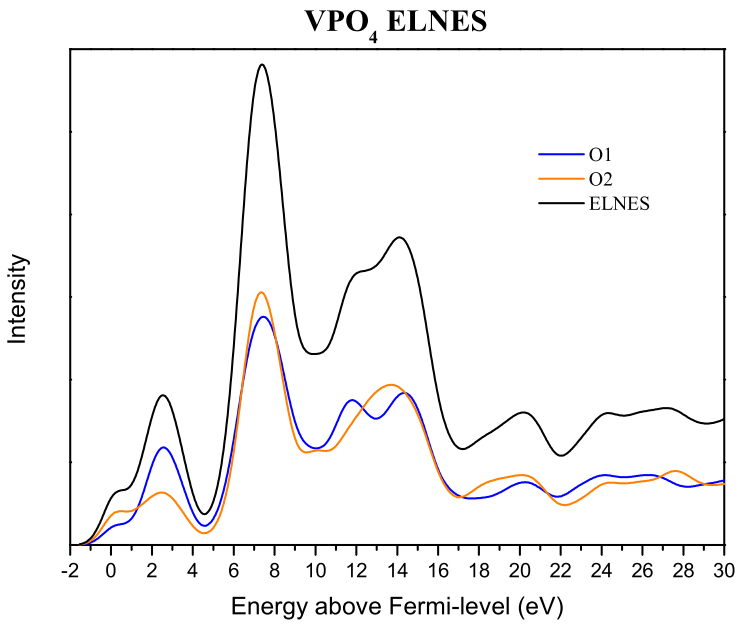

Fig. 7.9: Simulated oxygen K edge of VPO_4 and the contributions of the different oxygens.

Chapter 8

Discussion

8.1 Arrangement of structural units

The presence of VO_6 and PO_4 building blocks is a characteristic feature of the catalytically relevant VPO phases. This implies that during phase transformations, hydration, reduction and oxidation of these VPO phases, the VO_6 and PO_4 are preserved. Changes in the oxidation state effect the degree of distortion of the VO_6 units. The variable distortion of the VO_6 polyhedron, varying from a strongly distorted double pyramid in case of a 5+ oxidation state to a symmetric octahedron in the case of a 2+ oxidation state [79] can therefore be interpreted as the structural degree of freedom. It is a feature that is related to the easy transformation between the phases. Variations in the geometry of the VO_6 units can obviously be accomplished with relatively low effort, specially in the case of phases in which chains of VO_6 units are connected to one another along their apexes and embedded in the three dimensional structure via the oxygens of the equatorial plane. A change in the elemental ratios leads to a variation of the linkage between the elementary building blocks from corner to edge and even to plane sharing. As a result, the vanadium oxidation state is changed. The well located vanadium $3d$ states are switching between electron acceptor site in case of a 5+ oxidation state and electron donor site in the case of a lower oxidation state, as can be seen in Fig. 8.1. The vanadium hence switches between Lewis acidic and basic properties as a function of oxidation state and linking of the structural units.

In general, due to the weak interlayer interaction in the case of layered phases, structural rearrangements can be achieved more easily as in the case of more isotropic structures.

Since the partial oxidation of hydrocarbons involves a Mars van Krevelen mechanism, and due to the fact that releas of lattice oxygen is accomplished by a rearrangement of structural units, the substrate phase is involved in determining the energetics of oxygen exchange on the surface layers. One reason for the fact that VPP is the main phase observed in working catalysts could therefore be that its (100) face in effect "catalyzes" the Mars van Krevelen mechanism that is going on at the surface region of the active catalyst.

8.2 Some statements about the limitations and possibilities in the interpretation of ionization edges

Oxygen K edge

Measurements of the oxygen K ionization edge are connected with the following advantages:

- They appear in an easily accessible energy range with a good signal to noise ratio.
- Simulations of the oxygen K ionization edge are in good agreement with the experiment and can therefore be used for interpretation.
- The fine structure of the oxygen K ionization edge is very sensitive to structural effects such as the crystal field and the oxidation state.

The disadvantage of the oxygen K edge lies in the fact that it can not be used for monitoring structural changes of a catalyst under in-situ conditions since gas phase oxygen alters the spectrum and limits the possibilities of interpretation.

Vanadium K edge

The fine structure of the vanadium K edge monitors variations in the local geometric surrounding of the vanadium atoms. The two main drawbacks for the use of the vanadium K ionization edge are:

- Due to the high ionization energy, the vanadium K edge is not accessible in EELS measurements performed in a TEM. Instead, a synchrotron source is needed (NEXAFS).

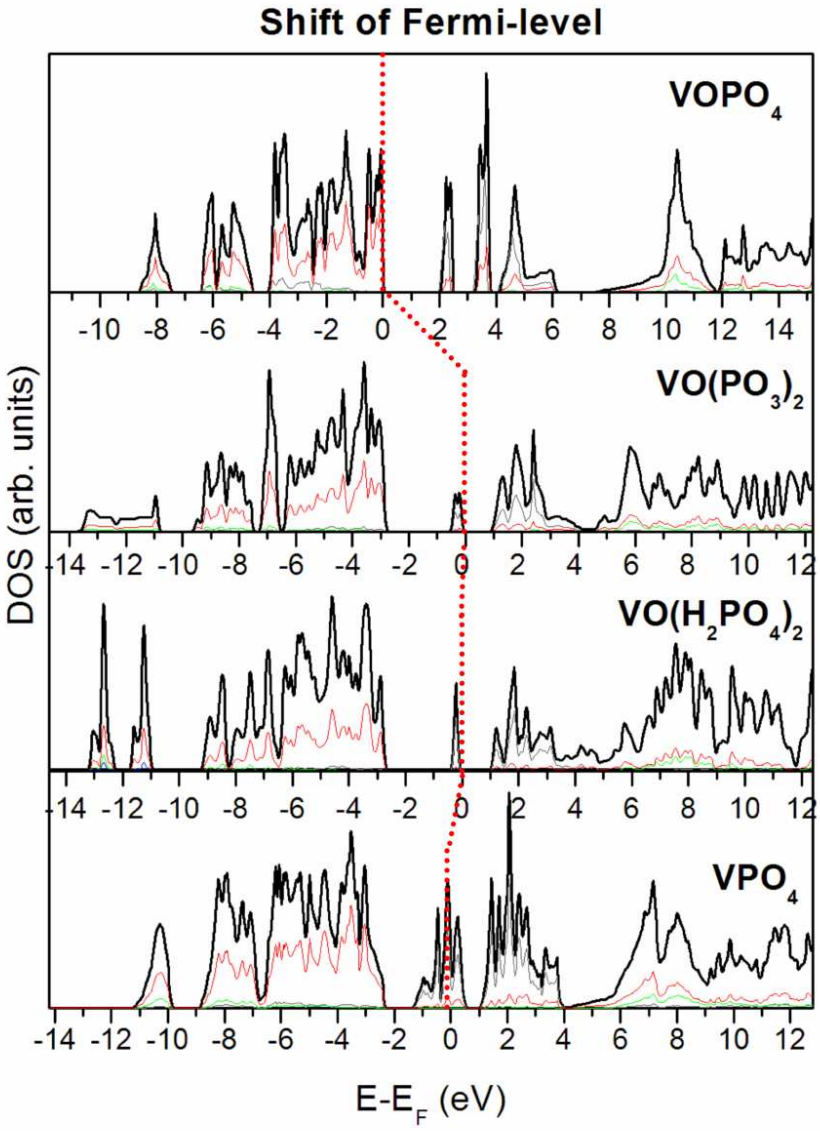

Fig. 8.1: Changes in the DOS with decreasing vanadium oxidation state. The projected DOS of oxygen, vanadium and phosphorus are plotted in red, gray and green, respectively.

- Simulations of the vanadium K ionization edge are in good agreement with the experiment, although the energy scale seems compressed in the simulation due to self energy effects.

Vanadium L edge

The vanadium L edges have the advantage of a high spectral intensity. Additionally, they appear in an energy range that is easily accessible for EELS. The shape of the L edges acts very sensitively on changes in the geometric and chemical environment of the vanadium atom. From their energy position the oxidation state of vanadium can be estimated and their width is a measure of the crystal field splitting. As a drawback, electron correlation effects (multiplet) effects make the simulation and interpretation of spectral features difficult. Only in case of V^{5+} phases, which have a $3d^0$ ground state, the multiplet effects have a relatively small influence on the spectral shape [70].

An overview of the crystal field splitting for different surroundings of the vanadium cation is given in Fig. 8.2. A comparison of the vanadium white-line of α_I-$VOPO_4$ and β-$VOPO_4$ with the calculated unoccupied vanadium $3d$ density of states indicates a correspondence between features in the spectrum and the position of empty states, although their intensities are not reproduced (see Fig. 8.4, 8.5,).

The fact that the empty vanadium $3d$ projected states can be related to the shape of the white lines is demonstrated in Fig. 8.6. The NEXAFS spectra were recorded at different orientation of the polarization vector of the synchrotron light with respect to the sample. The diagrams reveal a polarization dependence of the individual features. In the case of the first feature appearing slightly above 515 eV, the intensity is higher if the spectrum is recorded with the polarization vector oriented parallel to the x-y-plane (i.e. 90° from the z axis). This is in agreement with the localization of the corresponding final state ($3d_{xy}$). This experiments therefore prove that the agreement between theory and experiment does not only hold for the positions of the peaks, but also for their angular dependence.

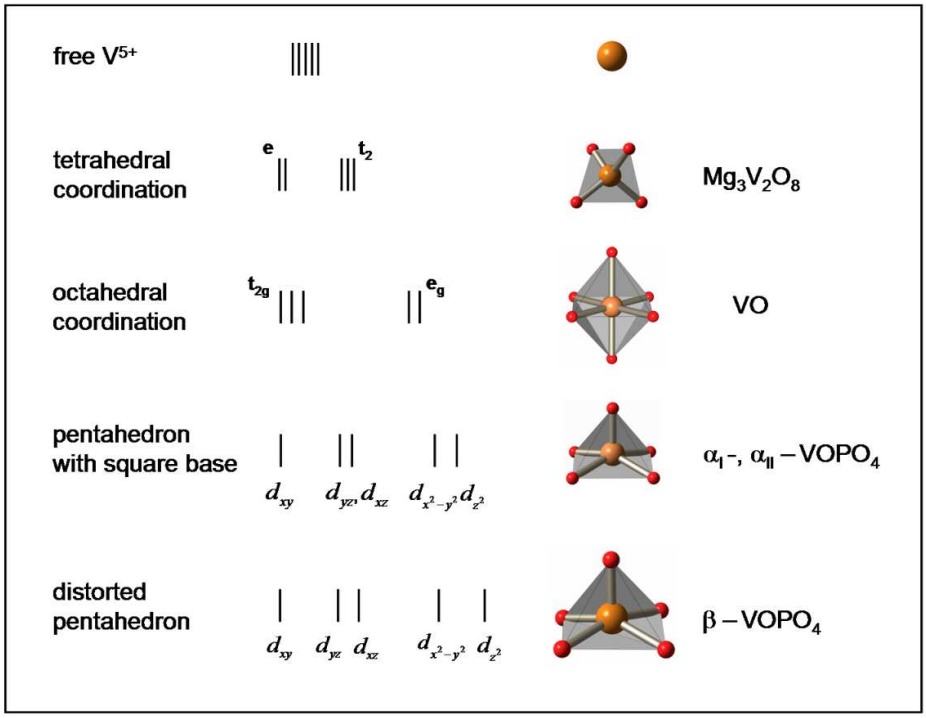

Fig. 8.2: The splitting of $3d$ states for different crystal fields.

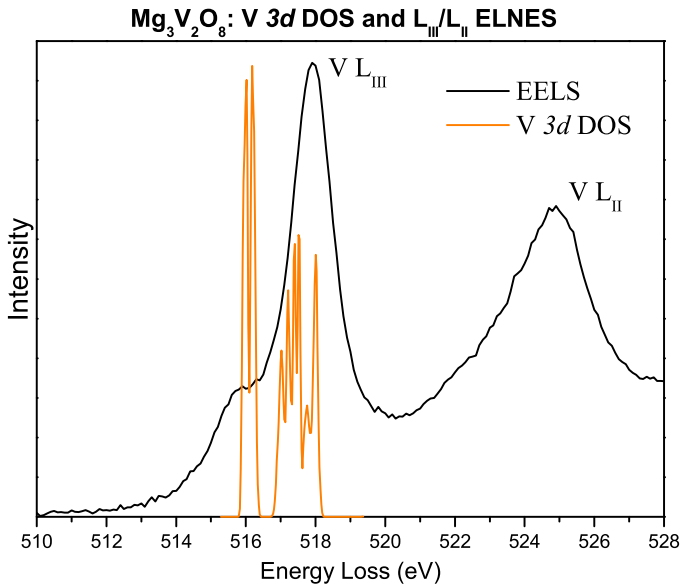

Fig. 8.3: Vanadium L_3 white line and the corresponding unoccupied $3d$ states of $Mg_3V_2O_8$. In this compound, the vanadium atom is in a 5+ oxidation state and tetrahedrally coordinated by oxygen atoms

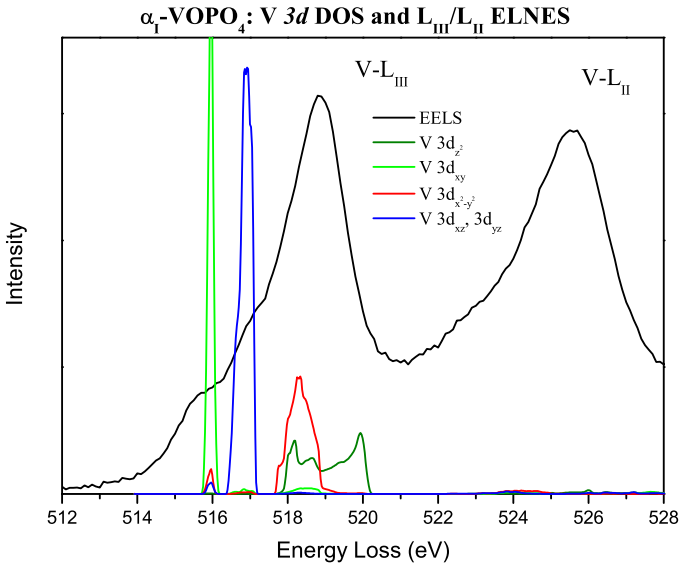

Fig. 8.4: Vanadium L_3 white line and the corresponding unoccupied $3d$ states of α_I-$VOPO_4$.

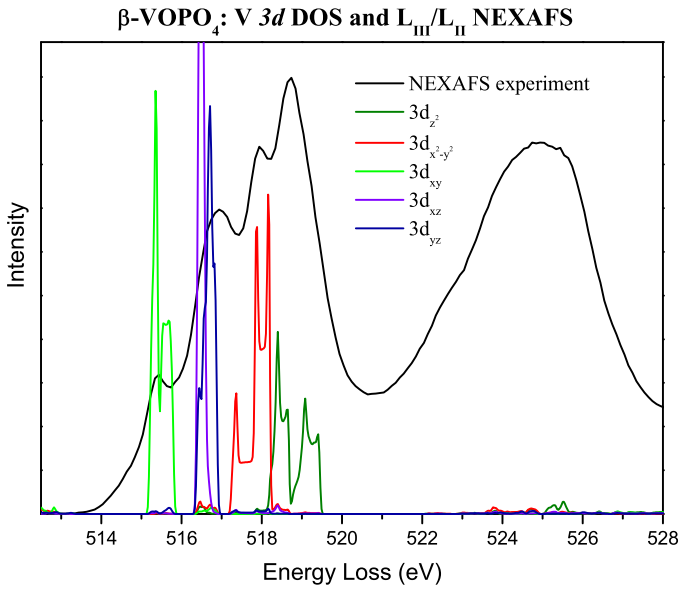

Fig. 8.5: Vanadium L_3 white line and the corresponding unoccupied $3d$ states of β-$VOPO_4$.

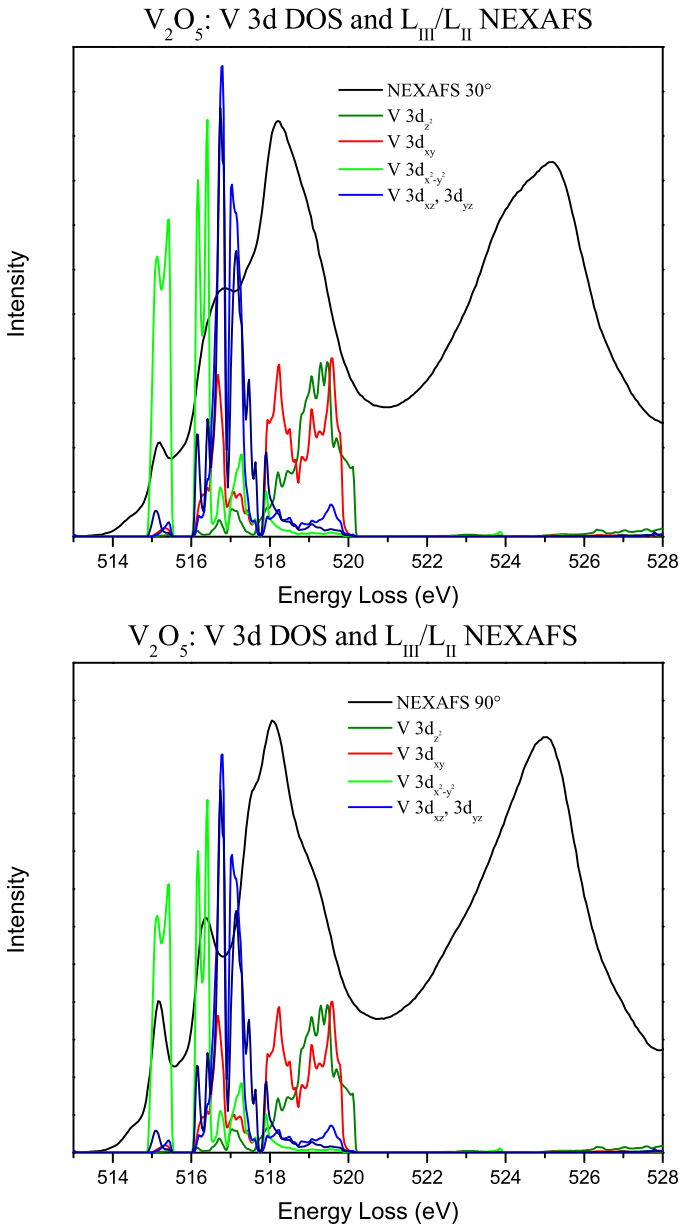

Fig. 8.6: Vanadium L white line recorded at different polarization angle and the calculated unoccupied $3d$ states of V_2O_5.

Chapter 9

Conclusion and Outlook

Vanadium phosphorus oxides (VPO) are a very complex and fascinating system characterized by an easy formation and interconversion of several crystalline phases. VPO´s are commercially used as catalysts for the synthesis of maleic anhydride in the partial oxidation of n-butane. Many spectra are recorded from a variety of samples in the quest for a good catalyst. But often the phase composition of the catalyst is not known and the recorded spectra are not easy to interpret. One way to get a more profound understanding of the working catalyst and the role of the different phases is to reduce the complexity of the system by investigating the specific occurring phases in depth on their own. In this work, the electronic structure of several VPO phases has been investigated by a combined theoretical and experimental approach. The investigated phases have been chosen according to their applicability as model substances for the investigation of the relation between geometric and electronic structure. Understanding this relation is a key issue in view of the unsolved questions concerning the catalytic properties of VPO based catalysts. The observed phases represent ideal model substances, as they contain structural features that are common to most of the catalytically relevant VPO phases.

Samples that were available, were characterized by X-ray diffraction and a combination of electron microscopic techniques. Electron energy loss spectroscopy (EELS) was applied as a sensitive tool to probe the local electronic structure at the oxygen and vanadium sites. It could be shown that the simulated spectra are in good agreement with experimental data. The combination of EELS with ab-initio simulations thereby offers the possibility of tracing back structural features present in recorded spectra to the underlying transitions at the corresponding sites.

A detailed insight into bonding properties such as hybridization and covalent versus ionic bonding and the localization of lone pairs was gained from an inspection of the site and angular momentum projected density of states. The effect of structural variations on the electronic structure was investigated for the case of two V_2O_5 polymorph and three $VOPO_4$ phases. The results of simulations and the presented EELS spectra point out the close agreement in the electronic structure of different $VOPO_4$ phases. It could be shown that differences in their total energy are very small and that variations in the density of states are mainly related to variations in the geometry and distortion of the VO_6 and PO_4 structural units, while their relative arrangement has only a minor effect on the electronic structure. Observed differences in the stability and hydration behavior as well as the reduction and re-oxidation properties are, on the other hand, determined by the way in which these units form the three dimensional structure. The electron density distribution reveals how corner sharing of VO_5 pyramids and strongly bonded PO_4 units forms a three dimensional network that is responsible for the higher stability of β-$VOPO_4$ with respect to the layer structure of α_I-, α_{II}-, γ- and δ-$VOPO_4$.

From the energetically well separated contributions of P-O and V-O bonds to the density of states and the fact that the total energy of the system and details of the electronic structure remain relatively unaffected by a variation of the arrangement of structural units, a reasonable chemical independence of the PO_4 and VO_5 building blocks was concluded.

Simulations performed for the case of V^{4+} phases revealed a very localized electron in a HOMO state located at the equatorial plane of the VO_6 polyhedron. As the Fermi level is shifted upwards with respect to the V^{5+} phases and the lowest vanadium $3d$ state is occupied with one electron, the band gap is determined by the splitting of this state from the remaining $3d$ states and hence, related to the distortion of the VO_6 polyhedron. In case of a V^{3+} oxidation state, the simulations have demonstrated the importance of a correct treatment of the electron spins when filling the vanadium $3d$ states. Such electron correlation effects set a limit to the application of a DFT ground state approach for the simulation of spectra. In the last chapter, these limitations have been pointed out by a comparison of vanadium L_3 edges obtained in high resolution NEXAFS experiments with the underlying density of states. It could be shown that at least for the case of V^{5+} phases, a correct assignment of spectral features to the underlying transitions is possible.

In the case of the oxygen K ionization edges, characteristic fingerprints in the spectra could be related to the different types of oxygens throughout the investigated phases. Spectral features in EELS spectra are hence well understood and serve as a basis set of

characteristic fingerprints that are related to different atom coordinations, structural distortions and oxidation states.

The gained insight therefore helps to assist the interpretation of spectra recorded from VPO samples of unknown phase composition and, even more interesting, to understand changes observed in spectra recorded during in-situ XAS experiments.

Appendix A

Structure data

A.1 γ-V_2O_5

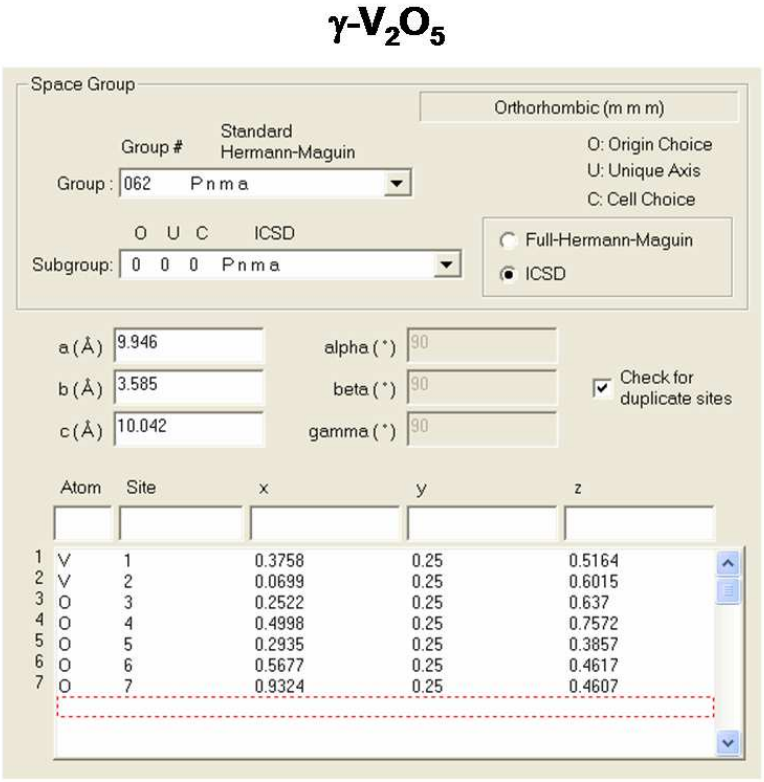

Fig. A.1: γ-V_2O_5

A.2 β-VOPO$_4$

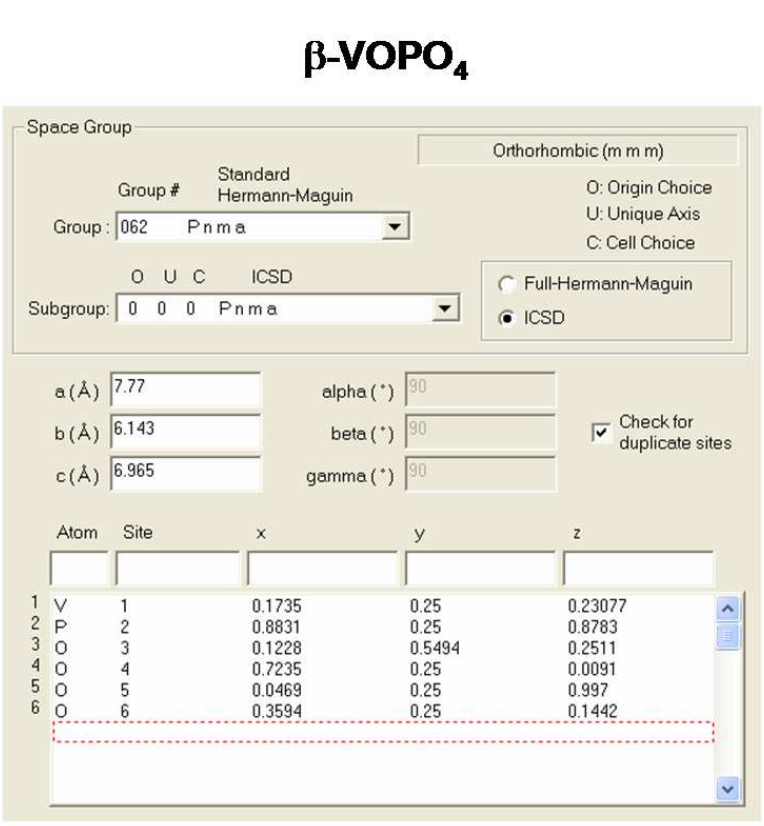

Fig. A.2: β-VOPO$_4$

A.3 α_I-$VOPO_4$

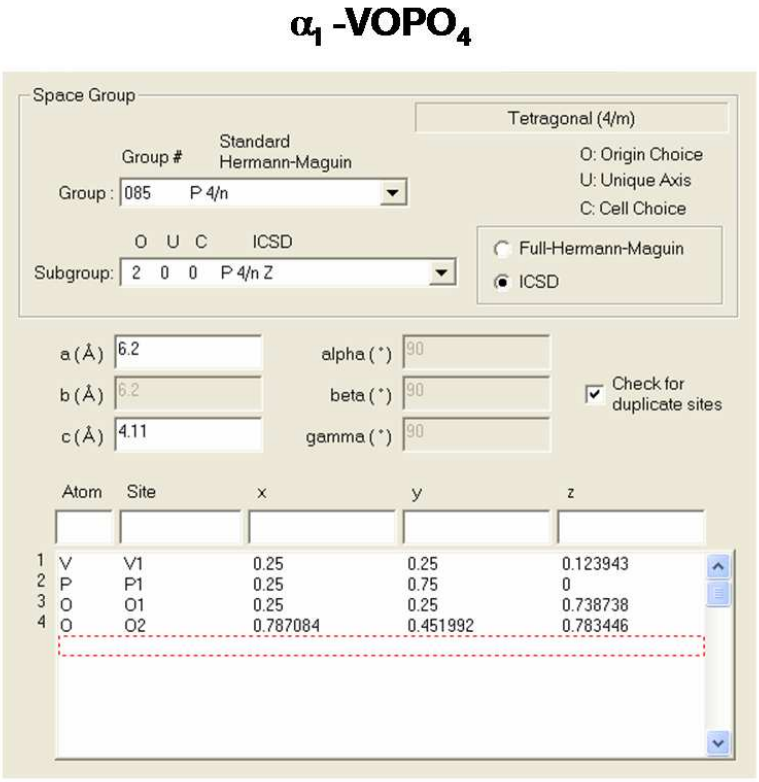

Fig. A.3: α_I-$VOPO_4$

A.4 α_{II}-VOPO$_4$

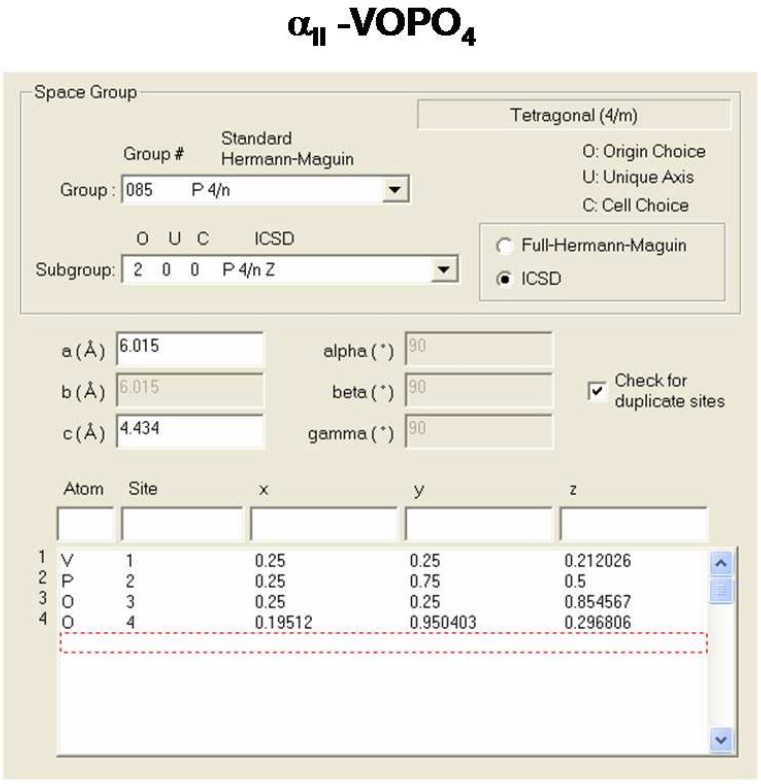

Fig. A.4: α_{II}-VOPO$_4$

A.5 $VO(PO_3)_2$

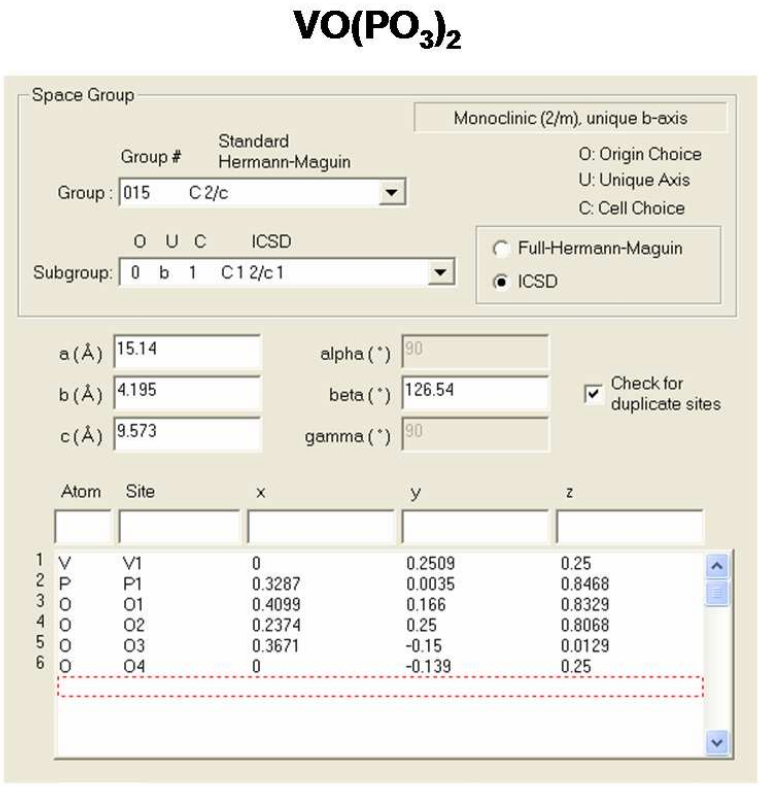

Fig. A.5: $VO(PO_3)_2$

A.6 $VO(H_2PO_4)_2$

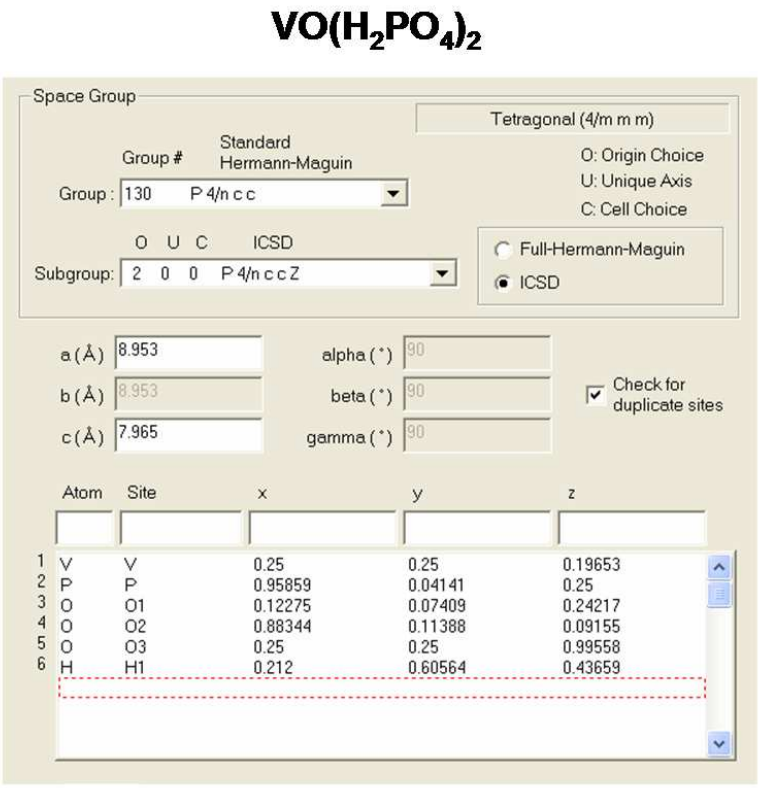

Fig. A.6: $VO(PO_3)_2$

A.7 VPO_4

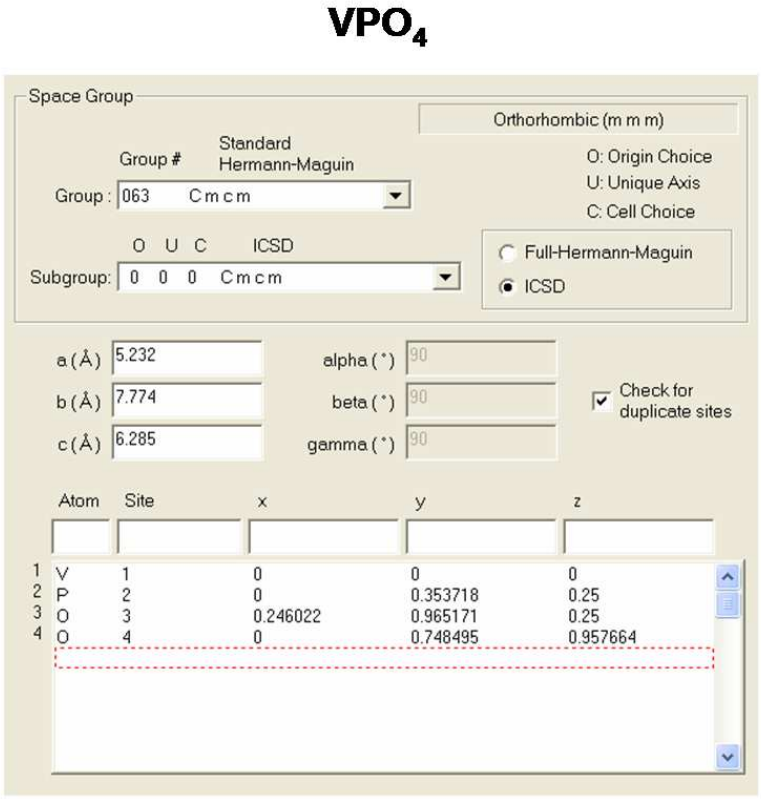

Fig. A.7: VPO_4

Bibliography

[1] E. BORDES, *Catal. Today* **1**, 499 (1987).

[2] G. CENTI, F. TRIFIRÒ, J. EBNER, and V. FRANCHETTI, *Chem. Rev.* **88**, 55 (1988).

[3] N. H. BATIS, H. BATIS, A. GHORBEL, J. C. VENDRINE, and J.-C. VOLTA, *J. Catal.* **128**, 248 (1991).

[4] C. J. KILEY, A. BURROWS, S. SAJIP, G. J. HUTCHINGS, M. T. SANANES, A. TUEL, and J.-C. VOLTA, *J. Catal.* **162**, 31 (1996).

[5] G. J. HUTCHINGS, C. J. KIELY, M. T. SANANES-SCHULZ, A. BURROWS, and J.-C. VOLTA, *Catal. Today* **40**, 273 (1998).

[6] R. J. H. CLARK, *The chemistry of titanium and vanadium*, Elsevier, Amsterdam, 1968.

[7] B. M. WECKHUYSEN and D. E. KELLER, *Catal. Today* **78**, 25 (2003).

[8] G. J. B., *J. of Sol. State Chem.* **3**, 490 (1971).

[9] W. BRÜCKNER, H. OPPERMANN, W. REICHELT, J. I. TERUKOW, F. A. TSCHUDNOWSKI, and E. WOLF, *Vanadiumoxide*, Akademie-Verlag, Berlin, 1983.

[10] F. J. MORIN, *Phys. Rev. Lett.* **3**, 34 (1959).

[11] P. AMORÓS, M. D. MARCOS, M. ROCA, J. ALAMO, A. BELTRÁN-PORTER, and D. BELTRÁN-PORTER, *J. Phys. Chem. Sol.* **62**, 1393 (2001).

[12] M. MALOW, *Hydrocarbon Process.* **11**, 149 (1980).

[13] R. WINCKLER, *Ann.* **4**, 230 (1832).

[14] J. PELOUZE, *Ann.* **11**, 263 (1834).

[15] J. SKEEN, *Chem. Eng. News* **26**, 3684 (1948).

[16] HTTP://WWW.SRICONSULTING.COM/CEH/PUBLIC/REPORTS/672.5000/?ABSTRACT.HTML.

[17] G. CENTI, *Catal. Today* **16**, 5 (1993).

[18] M. ABON and J.-C. VOLTA, *Appl. Catal. A-Gen.* **157**, 173 (1997).

[19] R. K. GRASSELLI, *Top. Catal.* **21**, 79 (2002).

[20] G. CENTI, F. CAVANI, and F. TRIFIRO, *Selective Oxidation by Heterogeneous Catalysis*, Kluwer Academic/Plenum, New York, 2001.

[21] U. RODEMERCK, B. KUBIAS, H. ZANTHOFF, and M. BAERNS, *Appl. Catal. A-Gen.* **153**, 203 (1997).

[22] B. CHEN and E. MUNSON, *J. Am. Chem. Soc.* **121**, 11024 (1999).

[23] R. K. GRASSELLI, *Top. Catal.* **15**, 93 (2001).

[24] P. MARS and D. W. VAN KREVELEN, *Chem. Eng. Sci.* **3**, 41 (1954).

[25] M.ABON, K. BÉRÉ, and P. DELICHÉRE, *Catal. Today* **33**, 15 (1997).

[26] P. COURTINE and E. BORDES, *Appl. Catal. A-Gen.* **157**, 45 (1997).

[27] G. W. COULSTON, S. R. BARE, H. KUNG, K. BIRKELAND, G. K. BETHKE, R. HARLOW, N. HERRON, and P. L. LEE, *Science* **275**, 191 (1997).

[28] B. HODNETT, *Catal. Rev. Sci. Eng.* **27**, 373 (1985).

[29] F. J. C. SANCHEZ, J. A. LOPEZ-SANCHEZ, R. P. WELLS, C. RHODES, A.-Z. ISFAHANI, and G. HUTCHINGS, *Cat. Lett.* **77**, 189 (2001).

[30] V. GULIANTS, J. BENZIGER, S. SUNDARASAN, I. WACHS, J. JEHNG, and J. ROBERTS, *Catal. Today* **28**, 275 (1996).

[31] D. J. THOMPSON, M. O. FANNING, and B. K. HODNETT, *J. Molec. Catal. A* **198**, 125 (2003).

[32] G. CENTI, G. GOLINELLI, and F. TRIFIRÒ, *Appl. Catal.* **48**, 13 (1989).

[33] F. B. ABDELOUAHAB, N. G. R. OLIER, F. LEFEBVRE, and J.-C. VOLTA, *J. Catal.* **134**, 151 (1992).

[34] G. J. HUTCHINGS, A. DESMARTIN-CHOMEL, R. OLIER, and J.-C. VOLTA, *Nature* **368**, 41 (1994).

[35] Y. ZHANG-LIN, M. FORISSIER, R. P. SNEEDEN, J. C. VÉDRINE, and J. C. VOLTA, *J. Catal* **145**, 256 (1994).

[36] Y. ZHANG-LIN, M. FORISSIER, J. C. VÉDRINE, and J. C. VOLTA, *J. Catal* **145**, 267 (1994).

[37] K. AIT-LACHGAR, M. ABON, and J. VOLTA, *J. Catal.* **171**, 383 (1997).

[38] F. CAVANI, S. LIGI, T. MONTI, F. PIERELLI, F. TRIFIRÒ, ALBONETTI, and G. MAZZONI, *Catal. Today* **61**, 203 (2000).

[39] P. L. GAI and K. KOURTAKIS, *Science* **267**, 647 (1995).

[40] G. CENTI, I. MANENTI, A. RIVA, and F. TRIFIRÒ, *Appl. Catal.* **9**, 177 (1984).

[41] Z.-Y. XUE and G. L. SCHRADER, *J. Phys. Chem. B* **103**, 9459 (1999).

[42] H. BLUHM, M. HAÄVECKER, E. KLEIMENOV, A. KNOP-GERICKE, A. LISKOWSKI, R. SCHLÖGL, and D. SU, *Surf. Sci.* **23**, 99 (2003).

[43] *EL/P 3.0 User's Guide*, Gatan, Inc., 1995.

[44] R. F. EGERTON, *Electron Energy-Loss Spectroscopy in the Electron Microscope*, Plenum Press, New York, 1996.

[45] SHRIVER and ATKINS, *Inorganic Chemistry*, Oxford University Press, ISBN 0-521-65214-6, Oxford, 1999.

[46] R. HOFFMANN, *Solids and Surfaces: A Chemist´s View on Bonding in Extended Structures*, VHC Publishers, Inc., 1988.

[47] P. HOHENBERG and W. KOHN, *Phys. Rev.* **136**, B864 (1964).

[48] L. HEDIN and B. I. LUNDQVIST, *J. Phys. C: Sol. St. Phys.* **4**, 2064 (1971).

[49] V. L. MORUZZI, J. F. JANAK, and A. R. WILLIAMS, *Calculated Properties of Metals*, Pergamon, New York, 1978.

[50] C. HÉBERT-SOUCHE, P.-H. LOUF, P. BLAHA, M. NELHIEBEL, J. LUITZ, P. SCHATTSCHNEIDER, K. SCHWARZ, and B. JOUFFREY, *Ultramicroscopy* **83**, 9 (2000).

[51] *WIEN2k, An Augmented Plane Wave + Local Orbitals Program for Calculating Crystal Properties*, Techn. Universität Wien, Austria, 2001. ISBN 3-9501031-1-2, 2001.

[52] J. P. PERDEW, K. BURKE, and M. ERNZERHOF, *Phys. Rev. Lett.* **77**, 3865 (1996).

[53] *XCrysden*, Techn. Universität Wien, Austria, 2001. ISBN 3-9501031-1-2, 2001.

[54] N. S. P. BHUVANESH and J. GOPALAKRISHNAN, *J. Mater. Chem.* **7(12)**, 2297 (1997).

[55] M. WITKO, R. TOKARZ, and J. HABER, *Appl. Catal. A-Gen.* **157**, 23 (1997).

[56] A. CHAKRABARTI, K. HERMANN, R. DRUZINIC, M. WITKO, F. WAGNER, and M. PETERSEN, *Phys. Rev. B* **59**, 10583 (1999).

[57] V. EYERT and K.-H. HÖCK, *Phys. Rev. B* **57** (1998).

[58] S. ATZKERN, S. V. BORISENKO, M. KNUPFER, M. S. GOLDEN, and J. FINK, *Phys. Rev. B* **61**, 12792 (2000).

[59] J. M. COCCIANTELLI, P. GRAVEREAU, J. P. DOUMERC, M. POUCHARD, and P. HAGENMULLER, *J. of Sol. State Chem.* **93**, 497 (1991).

[60] R. VALENTI, T. SAHA-DASGUPTA, J. V. ALVAREZ, K. P. ZGAJČIĆ, and C. GROS, *Phys. Rev. Lett.* **86**, 5381 (2001).

[61] N. PINNA, U. WILD, J. URBAN, and R. SCHLÖGL, *Adv. Mat.* **15**, 329 (2003).

[62] N. PINNA, M. WILLINGER, K. WEISS, J. URBAN, and R. SCHLÖGL, *Nano Letters* **3**, 1131 (2003).

[63] G. GU, M. SCHMID, P. CHIU, A. MINETT, J. FRAYSSE, G. KIM, S. ROTH, M. KOZLOV, E. MUÑOZ, and R. H. BAUGHMAN, *Nature Materials* **2**, 316 (2003).

[64] G. R. PATZKE, F. KRUMEICH, and R. NESPER, *Angew. Chem. Int. Ed.* **41**, 2446 (2002).

[65] V. V. IVANOVSKAYA, A. N. ENYASHIN, A. A. SOFRONOV, Y. N. MAKURIN, N. I. MEDVEDEVA, and A. L. IVANOVSKII, *Solid State Comm.* **126**, 489 (2003).

[66] S. J. KANG and T. C. OZAWA, Balls&Sticks ver. 1.4.2.

[67] D. S. SU, M. WIESKE, E. BECKMANN, A. BLUME, G. MESTL, and R. SCHLÖGL, *Catalysis Letters* **75**, 81 (2001).

[68] R. D. LEAPMAN and L. A. GRUNES, *Phys. Rev. Lett.* **45**, 397 (1980).

[69] J. FINK, T. MÜLLER-HEINZERLING, B. SCHEERER, W. SPEIER, F. U. HILLEBRECHT, J. C. FUGGLE, J. ZAANEN, and G. A. SAWATZKY, *Phys. Rev. B* **32**, 4899 (1985).

[70] F. M. F. DE GROOT, *J. of Electr. Spec. and Rel. Phenom.* **15**, 529 (1994).

[71] H. EICK and L. KIHLBORG, *Acta Chem. Scand.* **28**, 722 (1996).

[72] E. BORDES, *Catal. Today* **16**, 27 (1993).

[73] F. BENABDELOUAHAB, J.-C. VOLTA, and R. OLIER, *J. Catal.* **148**, 334 (1994).

[74] S. LIM, J. T. VAUGHEY, W. T. A. HARRISON, L. L. DUSSACK, A. J. JACOBSON, and J. W. JOHNSON, *Solid State Ionics* **84**, 219 (1996).

[75] T. P. MOSER and G. L. SCHRADER, *J. Catal.* **104**, 99 (1987).

[76] M. E. LASHIER, T. P. MOSER, and G. L. SCHRADER, editors, *New Developments in Selective Oxidation*, Elsevier Science Publishers, Amsterdam, 1990.

[77] M. E. LASHIER and G. L. SCHRADER, *J. Catal.* **128**, 113 (1991).

[78] R. GOPAL and C. CALVO, *J. Solid State Chem.* **5**, 432 (1972).

[79] C. HÉBERT, M. WILLINGER, D. S. SU, P. PONGRATZ, P. SCHATTSCHNEIDER, and R. SCHLÖGL, *Eur. Phys. J. B* **28**, 407 (2002).

[80] W. KRAUS and G. NOLZE, PowderCell for Windows Version 2.3, 1999.

[81] M. WILLINGER, Investigation of the Fine Structure in the Oxygen K Edge of Vanadium Oxides, Master's thesis, Vienna University of Technology, 2001.

[82] J. P. PERDEW and A. ZUNGER, *Phys. Rev. B* **23**, 5048 (1981).

[83] J. J. REHR and R. C. ALBERS, *Rev mod Phys* **72**, 621 (2000).

[84] J. K. BARTLEY, C. RHODES, C. J. KIELY, A. F. CARLEY, and G. J. HUTCHINGS, *Phys. Chem. Chem. Phys.* **2**, 4999 (2000).

[85] M. TACHEZ, F. THEOBALD, and E. BORDES, *J. Solid State Chem.* **40**, 280 (1981).

[86] E. BORDES, P. COURTINE, and G. PANNETIER, *Ann. Chim.* **8**, 105 (1973).

[87] B. JORDAN and C. CALVO, *Can. J. Chem.* **51**, 2621 (1973).

[88] C. SRILAXMI, N. LINGAIAH, A. HUSSAIN, P. S. S. PRASAD, K. V. NARAYANA, A. MARTIN, and B. LÜCKE, *Catal. Comm.* **5**, 199 (2004).

[89] E. BORDES, J. W. JOHNSTON, A. RAMINOSONA, and P. COURTINE, *Mater. Sci. Monograph* **28B**, 887 (1985).

[90] M. V. GANDUGLIA-PIROVANO and J. SAUER, *Phys. Rev. B* **70**, 45422 (2004).

[91] F. HANNOUR, A. MARTINA, B. KUBIAS, B. LÜCKE, E. BORDES, and P. COURTINE, *Catal. Today* **40**, 263 (1998).

[92] M. T. SANANES, G. J. HUTCHINGS, and J. C. VOLTA, *J. Catal.* **154**, 253 (1995).

[93] H. SAWADA, N. HAMADA, K. TERAKURA, and T. ASADA, *Phys. Rev. B* **53**, 12742 (1996).

[94] S. PETIT, S. A. BORSHCH, and V. ROBERT, *J. AM. CHEM. SOC.* **125**, 3959 (2003).

[95] D. C. JOHNSTON, J. W. JOHNSON, D. P. GOSHORN, and A. J. JACOBSON, *Phys. Rev. B* **35**, 219 (1987).

[96] R. GLAUM and R. GRUEHN, *Z. Kristallogr.* **198**, 41 (1992).

Danksagung

Diese Arbeit wurde im Zeitraum von März 2002 bis Juni 2005 in der Abteilung Anorganische Chemie am Fritz-Haber-Institut der Max-Planck-Gesellschaft angefertigt.
Mein Dank gilt Herrn Prof. Dr. Robert Schlögl für die interessante wissenschaftliche Fragestellung und die Ermöglichung dieser Doktorarbeit sowie seiner Unterstützung in Bezug auf die wissenschaftliche Arbeit und meinen weiteren wissenschaftlichen Werdegang.
Ich danke Herrn Prof. Dr. Martin Lerch für die ansprechende Zusammenarbeit, sowie für sein Interesse und die Übernahme des Zweitgutachtens für diese Arbeit. Einen besonderen Dank möchte ich priv. Doz. Dr. Thorsten Ressler aussprechen für seine Bereitschaft, als Vertreter bei der Verteidigung einzuspringen.
Ganz besonders möchte ich mich bei Dr. Dangsheng Su für sein Vertrauen, seine Betreuung und den Zuspruch insbesondere bei meiner Entscheidungsfindung für diese Doktorarbeit bedanken. Er hat ganz wesentlich zu einer meiner bisher wichtigsten und besten Entscheidungen beigetragen.

Ich möchte mich auch ganz herzlich bei den folgenden Personen bedanken:
Bei Jakob, weil ich von ihm wirklich sehr viel gelernt habe und er trotz all meiner Fragerei nie die Geduld verloren hat. Bei Jens und Jakob für die vielen ansprechenden Diskussionen über alle möglichen und unmöglichen Themen, für die super nette Zeit und die ausgesprochen gute und selbstlose Kooperation.
Bei Nicola, der mir eine große Hilfe war bei allen Hard– und Software–Problemen und mir auch noch zusätzliche Rechenkapazität für meine Simulationen zur Verfügung gestellt hat.
Bei Hermann Sauer, dem Spezialisten für alle Fragen, die sonst keiner beantworten kann.
Bei Gisela, Xiaowei, Achim, Di, Norbert und Klaus für die angenehme Zusammenarbeit und das immer freundliche Klima.
Bei Michael für die NEXAFS Spektren, bei Axel, bei Christian und bei Frank.
Nichts wäre, wie es ist, ohne meine Eltern, meine Geschwister und meine vielen Freunde.
Aber ganz besonders möchte ich mich bei Stephanie bedanken.